
CONTEMPORARY AND
INNOVATIVE RESEARCH IN
ENGINEERING
All Sciences Academy

CONTEMPORARY AND INNOVATIVE RESEARCH IN ENGINEERING

Editor
Asst. Prof. Dr. Umut ÖZKAYA

Contemporary and Innovative Research in Engineering
Editor: Asst. Prof. Dr. Umut ÖZKAYA

Design: All Sciences Academy Design
Published Date: March 2026
Publisher's Certification Number: 72273
ISBN: 978-625-8676-89-1

www.allsciencesacademy.com
allsciencesacademy@gmail.com

CONTENT

Hydrodynamic Behavior and Energy Losses in Transversely Corrugated Stainless Steel Flexible Pipes

Fevzi Balkan*
Ayşe Bilgen Aksoy
Yiğit Aksoy

1. Introduction

Corrugated stainless steel flexible pipes are increasingly employed across a broad range of engineering applications, including heating, ventilation, and air-conditioning (HVAC) systems, industrial fluid transport lines, renewable energy installations, and building services [1,2]. Their widespread use is largely attributed to several mechanical advantages over conventional rigid pipes, such as ease of installation, tolerance to misalignment, effective vibration damping, and the ability to accommodate thermal expansion without the need for additional compensators [1]. Owing to these characteristics, flexible corrugated pipes are particularly well suited for compact systems, retrofit applications, and installations subject to geometric constraints or dynamic loading conditions.

Despite these mechanical benefits, the hydraulic behavior of corrugated flexible pipes differs fundamentally from that of smooth or conventionally rough pipes. Periodic corrugations along the pipe wall introduce pronounced flow disturbances, promote earlier transition to turbulence, and induce flow separation accompanied by recirculation zones within the grooves [3–6]. As a result, pressure losses in corrugated pipes are substantially higher than those observed in smooth pipes of comparable diameter and length [7]. In practical systems, this increased pressure drop leads directly to higher pumping power requirements, reduced overall system efficiency, and elevated operational costs [8].

*This book chapter is derived from the Master's thesis entitled "Determination of Friction Factor for Different Flow Conditions in Stainless Steel Transversely Corrugated Flexible Pipes",

Within this framework, the present chapter provides a comprehensive discussion of the hydrodynamic behavior and energy losses in transversely corrugated stainless steel flexible pipes. Particular emphasis is placed on linking corrugation-induced flow features to their influence on friction factor behavior and pressure drop characteristics.

2. Physical Background of Corrugated Pipe Flows

The hydrodynamic behavior of flows in corrugated pipes is governed not only by classical parameters such as the Reynolds number and fluid properties, but also by the detailed geometry of the corrugations themselves. In contrast to smooth or uniformly rough pipes, corrugated pipes introduce periodic expansions and contractions along the flow direction, fundamentally modifying the local pressure and velocity fields.

2.1 Geometric Effects of Corrugation Parameters

Key geometric parameters—including corrugation height, pitch, and profile shape—control the intensity and spatial extent of flow separation, recirculation, and reattachment processes that develop within each groove [3–6]. From a physical standpoint, each corrugation acts as a localized disturbance that repeatedly interrupts boundary-layer development.

As the fluid accelerates over the crest of a corrugation and subsequently decelerates within the groove, an adverse pressure gradient is generated, which may lead to partial or complete boundary-layer separation. The resulting separated shear layers reattach downstream, producing localized regions of elevated turbulence production and enhanced momentum exchange between the near-wall region and the core flow [6,12].

2.2 Secondary Flows and Early Transition to Turbulence

One of the most distinctive characteristics of flows in corrugated pipes is the emergence of secondary flow structures that are absent in smooth-pipe configurations. These secondary motions arise from the combined influence of centrifugal forces, pressure gradients, and viscous effects acting within the corrugation grooves. As the flow encounters successive corrugation crests and cavities, localized separation occurs, followed by the formation of recirculation zones inside the grooves. A schematic illustration of this separation–reattachment mechanism is presented in Fig. 1, where the groove-induced vortical structures and reattachment regions are conceptually depicted.

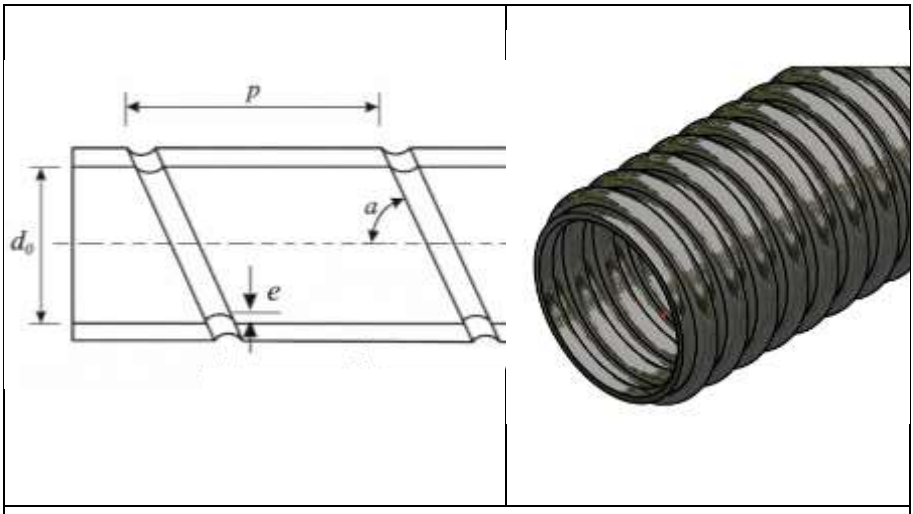

Fig. 1. Idealized geometric representation of a transversely corrugated pipe (left)(X) and representative three-dimensional view of a corrugated stainless steel flexible pipe (right)(Y)

The interaction between the primary axial flow and these groove-confined vortices enhances transverse momentum transport and promotes increased mixing across the pipe cross-section. Consequently, wall shear stress and form drag are amplified compared to smooth-pipe configurations. Unlike conventional rough-wall turbulence, these secondary structures are geometry-driven and may persist over a wide range of Reynolds numbers, continuously influencing the global dissipation characteristics of the flow.

A further important consequence of corrugation-induced disturbances is the early transition from laminar to turbulent flow. In smooth pipes, transition typically occurs at a critical Reynolds number of approximately 2300. In corrugated pipes, however, transition has been reported at significantly lower Reynolds numbers, depending on corrugation geometry and amplitude [3,5]. The repeated disruption of the boundary layer and the presence of separation bubbles, as illustrated in **Fig. 2**, act as inherent instability sources that accelerate the breakdown of laminar flow structures and promote turbulence onset.

3. Review of Friction Factor Approaches for Corrugated Pipes

The prediction of pressure losses in internal flows is traditionally based on the Darcy–Weisbach formulation, in which the friction factor represents the combined effects of wall shear stress and overall flow resistance. For smooth

and uniformly rough pipes, this framework has proven highly effective, leading to well-established correlations that relate the friction factor to the Reynolds number and relative roughness [9,10,21]. However, when applied to corrugated pipes, these classical approaches frequently fail to reproduce experimentally observed trends, indicating that additional geometry-driven flow mechanisms must be considered [3,12].

Early investigations into corrugated pipe flows already recognized that their hydraulic behavior differs fundamentally from that of smooth or conventionally rough pipes. Gibson's pioneering work demonstrated that corrugations introduce a substantial form-drag component in addition to viscous shear, resulting in friction factors significantly higher than those predicted by smooth-pipe theory [3]. Subsequent studies confirmed that pressure losses in corrugated pipes are governed by a complex interaction between flow separation, vortex formation, and reattachment processes occurring within the corrugation grooves, rather than by wall roughness effects alone [6,12].

In response to these observations, several empirical correlations were proposed to incorporate geometric parameters such as corrugation height, pitch, and pipe diameter explicitly. Among the earliest systematic contributions, Hawthorne and von Helms emphasized the dominant role of geometry in determining frictional behavior, demonstrating that corrugated hoses cannot be characterized solely by Reynolds-number similarity [15]. Their findings revealed that geometrically similar corrugated pipes may exhibit markedly different friction factors when scaled in diameter, even under dynamically similar flow conditions [15,17]. This departure from classical similarity principles highlighted the inadequacy of treating corrugations as equivalent roughness elements.

Later experimental investigations reinforced these conclusions. Measurements conducted on transversely corrugated pipes revealed a persistent diameter dependence of the friction factor, contradicting the classical assumption that Reynolds-number similarity ensures dynamic similarity [11,12]. In particular, Ahn and Uslu reported that friction factors increase with pipe diameter at fixed Reynolds numbers, despite decreasing relative roughness ratios [12]. This counterintuitive behavior was attributed to the enlargement and sustained influence of groove-induced separation zones and secondary flow structures in larger pipes, which promote continuous turbulence production and enhanced momentum exchange between the near-wall region and the core flow [6,13].

Further experimental contributions, notably those by Popiel and co-workers, provided evidence of non-classical friction factor behavior over a wide range of Reynolds numbers [13]. Their results showed that corrugated pipes do not

necessarily approach a fully rough regime characterized by Reynolds-number-independent friction factors. Instead, the friction factor may continue to vary with Reynolds number even at high flow rates, reflecting the persistent influence of unsteady vortical structures and secondary motions generated by the corrugation geometry [13,14]. This behavior fundamentally distinguishes corrugated pipes from both smooth and uniformly rough configurations.

Despite their practical usefulness, most available friction-factor correlations remain limited in scope. Many are derived from narrowly defined experimental datasets and are closely tied to specific corrugation geometries or manufacturing processes [15,17]. Consequently, their direct application to different pipe designs or operating conditions may introduce significant uncertainty. Moreover, purely empirical curve-fitting approaches provide limited physical insight into the underlying energy-dissipation mechanisms, restricting their generalizability beyond the tested parameter ranges [6,11].

From an engineering standpoint, these limitations present a tangible design challenge. Practitioners often rely on manufacturer-supplied data, conservative safety margins, or smooth-pipe-based estimates augmented by empirical correction factors [1]. While such strategies may ensure operational reliability, they frequently result in oversized pumping systems and increased energy consumption [8]. These considerations underscore the need for physically informed modeling strategies that explicitly account for the distinctive flow mechanisms induced by corrugation geometry [6,12].

Recent investigations published between 2023 and 2025 have revisited corrugated pipe flows using high-resolution numerical simulations and integrated thermo-hydraulic performance metrics [22–24]. Contemporary CFD-based analyses consistently emphasize that the hydraulic penalty associated with corrugations cannot be interpreted simply as an increase in equivalent roughness. Instead, periodic groove geometries generate strong secondary vortical structures and flow-separation regions that persist over a wide range of Reynolds numbers, sustaining elevated turbulence levels and pressure losses even under conditions where smooth pipes would approach asymptotic behavior [22,23].

High-fidelity simulations further demonstrate that the interaction between groove-induced vortices and the core flow produces complex, geometry-dependent dissipation mechanisms that remain sensitive to both Reynolds number and geometric scaling [22]. These findings extend earlier experimental observations by providing detailed flow-field interpretations of energy dissipation processes [6,12,23]. Moreover, recent studies adopting a coupled thermo-hydraulic and system-level perspective highlight the inherent trade-off between enhanced transport processes and increased pressure losses in corrugated pipes [23,24]. Within this broader framework, the friction factor

is no longer treated as an isolated hydraulic parameter, but rather as part of an integrated performance assessment that incorporates pumping power requirements and overall energy efficiency [24].

Taken together, the studies reviewed in this section demonstrate that the friction factor in corrugated pipes cannot be interpreted within the classical smooth- or rough-pipe framework. Geometry-induced separation, persistent secondary flow structures, and scale-dependent dissipation mechanisms fundamentally alter the relationship between Reynolds number and hydraulic resistance. These observations suggest that a purely friction-factor-based evaluation is insufficient to fully characterize the performance of corrugated pipes. Instead, a broader energy-oriented perspective is required, in which pressure losses are directly linked to pumping power and overall system efficiency. Such an approach is discussed in the following section.

4. Energy Perspective on Hydraulic Losses in Corrugated Pipes

From an energy-systems standpoint, hydraulic losses in internal flows represent a direct penalty on overall system efficiency. In smooth-pipe applications, pressure losses can generally be estimated with reasonable accuracy using classical friction-factor correlations, allowing pumping power requirements to be predicted with limited uncertainty. In corrugated pipes, however, the non-classical friction behavior discussed in the preceding sections introduces additional complexity, making an explicit energy-based evaluation essential for realistic system design.

The mechanical power required to sustain flow through a pipe is directly related to the pressure drop and the volumetric flow rate. Consequently, the elevated pressure losses induced by corrugation geometry translate into substantially higher pumping power demands compared to smooth pipes of similar nominal dimensions. This increase cannot be regarded as a minor correction to smooth-pipe estimates. Rather, it reflects fundamental changes in the flow structure, including persistent separation zones, secondary vortical motions, and sustained turbulence production within the corrugation grooves [6,12,13].

An important implication of this behavior is that the friction factor alone provides an incomplete description of energetic performance. Although it

remains a useful dimensionless indicator of hydraulic resistance, it does not directly quantify the actual energy cost associated with maintaining a prescribed flow rate. In engineering systems—particularly HVAC installations, industrial process piping, and energy-conversion devices—pumping power constitutes a recurring operational expense that accumulates over the lifetime of the system. As a result, even moderate increases in friction factor may produce significant long-term energy penalties.

Recent studies adopting an energy-oriented perspective emphasize that the hydraulic penalty associated with corrugated pipes must be evaluated relative to the intended system function. In applications where enhanced mixing or transport processes are desirable, such as compact heat exchangers or intensified thermal systems, the increased pressure loss may be partially offset by improvements in heat-transfer performance [8,22,23]. From this viewpoint, corrugated pipes should not be assessed solely in terms of minimizing friction factor, but rather through a combined evaluation of transport enhancement and energy consumption. This inherent trade-off highlights the necessity of performance metrics that integrate hydraulic resistance with energetic efficiency.

Another critical aspect of the energy perspective is the strong dependence of pumping power on both flow rate and pipe diameter. Since pumping power scales with the product of pressure drop and volumetric flow rate, the diameter-dependent friction behavior observed in corrugated pipes has amplified energetic consequences. Experimental and numerical evidence indicates that, at identical Reynolds numbers, larger-diameter corrugated pipes may incur disproportionately higher energy penalties than smaller ones, despite exhibiting lower relative roughness ratios [12,13]. This observation challenges conventional scaling arguments and further illustrates the limitations of applying smooth-pipe-based energy estimates to corrugated geometries.

At the system level, the implications extend beyond the pipe segment itself. Increased pumping power requirements influence pump selection, motor sizing, and control strategies, with potential consequences for system reliability and capital investment. Furthermore, elevated energy consumption contributes to higher operating costs and increased environmental impact, particularly in installations characterized by continuous or long-duration operation. These considerations reinforce the importance of evaluating corrugated pipe performance within a broader energy and sustainability framework rather than treating hydraulic losses as an isolated design variable.

Recent CFD-based investigations published between 2023 and 2025 further support this perspective by explicitly linking flow structures to energy-dissipation mechanisms. High-resolution simulations demonstrate that

groove-induced vortical structures persist downstream and continue interacting with the core flow, resulting in sustained energy dissipation that cannot be mitigated simply by increasing the Reynolds number [22–24]. Such findings confirm that corrugated pipes do not exhibit a classical asymptotic regime in which energy losses become independent of flow rate, as often assumed for fully rough smooth pipes.

In summary, an energy-based assessment provides a more comprehensive and physically meaningful framework for evaluating hydraulic losses in corrugated pipes. By explicitly accounting for pumping power requirements, geometric scaling effects, and system-level implications, this perspective complements traditional friction-factor analysis and offers a more robust basis for engineering decision-making. The integration of hydraulic and energetic considerations is therefore essential for the rational design and optimization of systems employing corrugated pipe geometries.

5. Governing Equations and Modeling Assumptions

The hydrodynamic behavior of flow in corrugated pipes is governed by the fundamental conservation principles of mass and momentum. For incompressible, single-phase flows with constant thermophysical properties, the governing equations are formulated in the framework of the Reynolds-averaged Navier–Stokes (RANS) equations. This approach enables the description of the mean flow field while accounting for turbulence effects through suitable closure relations.

5.1 Continuity and Momentum Equations

For steady, incompressible flow, the continuity equation is expressed as

$$\nabla \cdot \mathbf{u} = 0 \tag{1}$$

where $\mathbf{u}$denotes the mean velocity vector.

The Reynolds-averaged momentum equation can be written in tensor form as

$$\rho(\mathbf{u} \cdot \nabla)\mathbf{u} = -\nabla p + \mu \nabla^2 \mathbf{u} - \nabla \cdot (\rho \mathbf{u}'\mathbf{u}') \tag{2}$$

where ρ is the fluid density, $p$the mean pressure, μ the dynamic viscosity, and $\rho \mathbf{u}'\mathbf{u}'$ the Reynolds stress tensor arising from turbulent velocity fluctuations.

In corrugated pipe flows, the Reynolds stress contribution is particularly significant due to strong velocity gradients, periodic flow separation, and recirculation within the grooves. These mechanisms enhance turbulence

production and increase overall momentum dissipation compared to smooth-pipe configurations.

5.2 Turbulence Modeling

Closure of the RANS equations requires a turbulence model. In the present framework, a two-equation eddy-viscosity model is adopted, as it offers a balanced compromise between predictive accuracy and computational efficiency.

Within the k–ε formulation, the turbulent (eddy) viscosity is defined as

$$\mu_t = \rho C_\mu \frac{k^2}{\varepsilon} \tag{3}$$

where $k$is the turbulent kinetic energy, ε its dissipation rate, and C_μ a model constant.

The transport equations for k and ε are given by

$$\rho(\mathbf{u} \cdot \nabla)k = \nabla \cdot \left[\left(\mu + \frac{\mu_t}{\sigma_k}\right)\nabla k\right] + G_k - \rho\varepsilon \tag{4}$$

$$\rho(\mathbf{u} \cdot \nabla)\varepsilon = \nabla \cdot \left[\left(\mu + \frac{\mu_t}{\sigma_\varepsilon}\right)\nabla \varepsilon\right] + C_{1\varepsilon}\frac{\varepsilon}{k}G_k - C_{2\varepsilon}\rho\frac{\varepsilon^2}{k} \tag{5}$$

where G_k represents the production of turbulent kinetic energy due to mean velocity gradients. Standard model constants are adopted according to established literature.

Although the classical k–ε equations are presented for completeness, the numerical simulations in this study employ the realizable k–ε variant. In this formulation, the eddy-viscosity coefficient is not treated as a universal constant, and additional mathematical constraints are imposed to ensure realizability of the turbulence stresses. This modification improves predictive performance in flows involving separation, curvature, and rotation—features inherent to corrugated pipe geometries.

5.3 Near-Wall Treatment and Modeling Scope

Accurate representation of the near-wall region is critical in corrugated pipe simulations. Strong curvature and periodic cavity structures prevent the development of a classical logarithmic boundary layer along the wall. Consequently, conventional smooth-wall assumptions may not be locally valid.

In practical computations, wall functions or enhanced near-wall treatments are employed to bridge the viscous sublayer and fully turbulent region, provided that the mesh resolution satisfies recommended y^+criteria. This strategy allows reliable estimation of wall shear stress and form drag without excessive grid refinement.

Depending on the objectives of the analysis, both two-dimensional and three-dimensional computational domains may be used. Two-dimensional models are appropriate for investigating fundamental separation–reattachment mechanisms and groove-induced vortical structures at reduced computational cost. Three-dimensional simulations are required when azimuthal variations or complex corrugation profiles significantly influence the flow field.

5.4 Modeling Assumptions

The following simplifying assumptions are adopted:

Steady-state conditions

Incompressible Newtonian fluid

Isothermal flow

Hydraulically rigid pipe wall

Negligible gravitational effects for horizontal configurations

These assumptions are consistent with the majority of experimental and numerical studies on corrugated pipe flows and enable direct comparison with available benchmark data.

6. Pressure Losses and Numerical Methodology for Corrugated Pipes

6.1 Physical Origin of Pressure Losses

Pressure losses in internal pipe flows originate primarily from viscous friction within the fluid and from resistance imposed by the confining wall. Even in hydraulically smooth pipes, finite pressure drops arise as a direct consequence of internal viscous dissipation.

In corrugated pipes, however, an additional and often dominant loss mechanism emerges. The periodically indented wall geometry produces successive contractions and expansions along the flow direction, inducing

boundary-layer separation, recirculation within the grooves, and the formation of coherent vortical structures.

These groove-induced flow structures intensify turbulence production and increase form drag, leading to pressure losses substantially greater than those observed in smooth or uniformly rough pipes operating under comparable conditions. Unlike classical roughness effects—where energy dissipation is primarily governed by near-wall shear stress—losses in corrugated geometries are strongly influenced by geometry-driven separation and sustained secondary flow motions.

A rigorous interpretation of pressure losses in corrugated pipes therefore requires revisiting the classical smooth-pipe framework and extending it to incorporate the additional mechanisms introduced by corrugation geometry. Establishing this baseline is essential for understanding the limitations of conventional friction-factor correlations and for developing a coherent foundation for the numerical and energy-based analyses presented in the subsequent sections.

6.2 Pressure Losses in Smooth Pipes

6.2.1 Classical Framework for Smooth Pipes

For smooth, straight pipes, the total head loss consists of friction losses along the pipe length and local (minor) losses associated with fittings such as elbows, valves, and flow meters. The Darcy–Weisbach equation provides the friction head loss as follows [23]:

$$h_f = f\frac{L}{d}\frac{V^2}{2g} \tag{6}$$

where Ldenotes the pipe length, $D$the pipe diameter, V the mean flow velocity, g the gravitational acceleration, and f the Darcy friction factor.

The head loss associated with N local elements is expressed as [23]:

$$h_e = \sum_{i=1}^{N} K_i \frac{V^2}{2g} \tag{7}$$

The total pressure drop become [23]:

$$\Delta P = \rho g\left(h_f + h_e\right) \tag{8}$$

For laminar flow in smooth pipes, the friction factor depends solely on the Reynolds number and is given by

$$f = \frac{64}{Re} \tag{9}$$

In turbulent flow regimes, the friction factor depends on both the Reynolds number and the relative roughness, defined as

$$\varepsilon = \frac{e}{D} \tag{10}$$

where e represents the average roughness height.

One of the most widely used implicit correlations for turbulent flow is the Colebrook equation [23]:

$$\frac{1}{\sqrt{f}} = -2.0 \log\left(\frac{\varepsilon}{3.7} + \frac{2.51}{Re\sqrt{f}}\right) \tag{11}$$

A commonly employed explicit alternative is the Haaland equation [23]:

$$\frac{1}{\sqrt{f}} = -1.8 \log\left[\left(\frac{\varepsilon}{3.7}\right)^{1.11} + \frac{6.9}{Re}\right] \tag{12}$$

In addition to these analytical correlations, the Moody diagram provides a graphical summary of extensive experimental data and remains a standard engineering reference for estimating friction factors in smooth and rough pipes [23]. For smooth-pipe flows, the friction factor generally decreases with increasing Reynolds number and may approach an asymptotic regime at sufficiently high Reynolds numbers. These classical trends establish a well-defined baseline for internal flow behavior.

However, as will be shown in the following sections, corrugated pipes do not necessarily follow this classical smooth- or rough-pipe logic. The additional separation, form drag, and geometry-induced secondary flow mechanisms significantly complicate the determination of the friction factor in corrugated configurations.

6.3 Corrugated (Flexible) Pipes: Empirical Models and Non-Classical Behavior

In corrugated pipes, friction losses become significantly more pronounced as a direct consequence of groove-induced flow structures. Although several experimental investigations have been reported in the literature, broadly applicable correlations capable of reliably predicting friction factors remain relatively limited.

One of the early modeling approaches was proposed by Hawthorne and von Helms [14], who idealized corrugated hoses as a sequence of orifice-like elements and derived the following expression for the pressure drop:

$$\Delta P = \frac{N}{2}\rho V^2 \left[1 - \left(\frac{d}{d+\gamma s}\right)^2\right]^2 \tag{13}$$

where d denotes the inner diameter, $s$the distance between two adjacent corrugation crests (pitch), N the number of corrugations along the pipe, and γan empirical constant. Because this formulation does not explicitly incorporate Reynolds-number effects or a friction-factor framework, uncertainties on the order of ±30% have been reported for typical applications [13].

To explicitly account for Reynolds-number dependence, Kauder [13] proposed the following empirical relation for the Darcy friction factor:

$$\ln f = 6.75 + 4.13 \ln\left(\frac{t}{d}\right) + \left[230\left(\frac{t}{d}\right)^{2.1} - 0.7\right] \ln\left(\frac{t}{s}\right) + 0.193 e^{-3300\left(\frac{t}{d}\right)^{2.6}\left(\frac{t}{s}\right)} \ln Re \tag{14}$$

where t represents the corrugation height (or groove depth).

Once the friction factor $f$is obtained, the corresponding pressure drop may be calculated as [13]:

$$\Delta P = 4f \frac{L}{d}\left(\frac{\rho V^2}{2}\right) \tag{15}$$

The applicability of this correlation is restricted to the following parameter ranges:

$$0.0455 < \frac{t}{d} < 0.0635 \text{and} 0.2 < \frac{t}{s} < 0.6 \tag{16}$$

For a specific U-profile corrugated pipe geometry, Bernhard and Hsieh [9] proposed an alternative empirical formulation expressed as

$$f = \ln\left(C_0 + C_1 Re_d + C_2 Re_d^2\right) \tag{17}$$

Taken together, these studies demonstrate that corrugated pipes may deviate substantially from the smooth- or rough-pipe logic embedded in conventional friction-factor correlations. In particular, unlike smooth pipes, corrugated configurations do not necessarily exhibit a monotonic decrease in friction factor with increasing Reynolds number.

In practical engineering applications, manufacturer-provided friction-factor charts—when available—may therefore serve as useful references, although their completeness and reliability vary between suppliers. Comprehensive documentation, such as that provided by Witzenmann, is often regarded as a benchmark in this context [1].

From a physical standpoint, groove-induced secondary flows provide a plausible explanation for the observed non-classical behavior. Flow within corrugation cavities is subjected to strong transverse pressure gradients and centrifugal effects, which sustain vortex-like secondary motions and fundamentally alter global dissipation characteristics. Consequently, friction losses in corrugated pipes cannot be attributed solely to wall roughness, but must instead be interpreted as the outcome of complex, geometry-driven flow mechanisms.

6.4 Governing Hydrodynamic Equations (RANS Formulation)

The numerical simulations are performed by solving the governing equations introduced in Section 5 within a finite-volume framework. The flow is assumed to be Newtonian, incompressible, turbulent, steady, and isothermal.

For completeness, the continuity equation governing mass conservation is expressed as

$$\nabla \cdot \mathrm{u} = 0 \tag{18}$$

and the Reynolds-averaged momentum equation may be written in compact tensor form as

$$\rho(\mathrm{u} \cdot \nabla)\mathrm{u} = -\nabla p + \mu \nabla^2 \mathrm{u} - \nabla \cdot (\rho \mathrm{u}'\mathrm{u}') \tag{19}$$

Turbulence closure is achieved using the realizable k–εmodel. The turbulent (eddy) viscosity is defined as

The continuity equation for incompressible flow is expressed as

$$\mu_t = \rho C_\mu \frac{k^2}{\varepsilon} \tag{20}$$

In the realizable formulation, the coefficient $C_\mu$is no longer treated as a universal constant, and additional realizability constraints are imposed on the dissipation equation. This modification improves predictive accuracy for flows involving separation, curvature, and secondary vortical structures—features inherent to corrugated pipe geometries [25].

6.5 Mesh Design, Near-Wall Resolution, and Boundary Conditions

The computational domain corresponding to the two-dimensional transversely corrugated pipe and the associated mesh structure are illustrated in Figure 2.

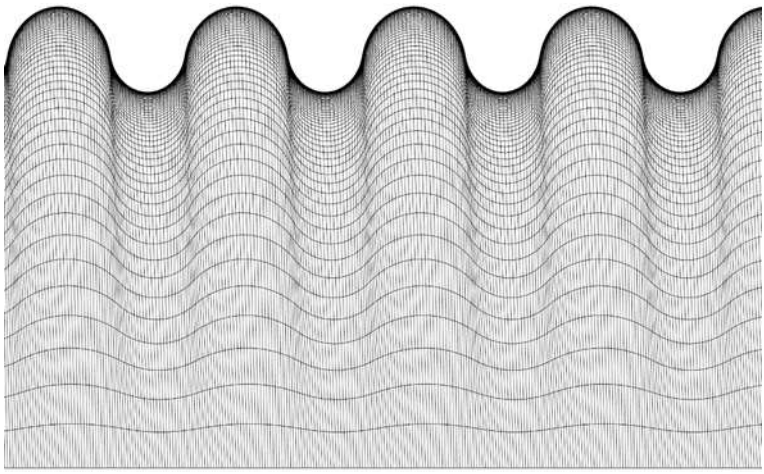

Figure 2. Two-dimensional corrugated pipe geometry and computational mesh

Because the governing equations constitute a coupled system of partial differential equations, analytical solutions are not feasible for the corrugated pipe geometry considered in this study. A numerical approach is therefore required. In computational fluid dynamics (CFD), the solution domain is discretized into a finite number of control volumes. The spatial resolution of this mesh directly influences both numerical accuracy and computational cost.

An effective strategy consists of applying mesh refinement selectively in regions characterized by strong velocity and pressure gradients—most notably within the near-wall boundary-layer region—while employing a comparatively coarser mesh in the core flow to limit computational expense. This approach is particularly important for corrugated geometries, where groove-induced separation and recirculation generate steep local gradients.

Near-Wall Resolution

Near-wall resolution is governed by the wall-law concept, which relates the first grid spacing adjacent to the wall to local flow conditions. The non-dimensional wall distance is defined as [26]:

$$y^+ = \frac{\rho y^* u^*}{\mu} \tag{21}$$

where u_τ is the friction velocity. The friction velocity is defined as

$$u^* = \sqrt{\frac{\tau_w}{\rho}} \tag{22}$$

and the wall shear stress τ_w is approximated as

$$\tau_w = 0.5\, C_f\, \rho V^2 \tag{23}$$

with the skin-friction coefficient expressed as

$$C_f = 0.078 Re^{-0.25} \tag{24}$$

Solving the first near-wall cell height y^*yields [26]:

$$y^* = \frac{\mu y^+}{\rho V \sqrt{0.039(\rho V d/\mu)^{-0.25}}} \tag{25}$$

To ensure adequate resolution of the viscous sublayer, a target value of $y^+ = 1$is commonly recommended and is adopted in the present simulations [25].

Boundary Conditions

Boundary conditions are prescribed in accordance with standard internal-flow modeling practice. A no-slip condition is imposed at all solid walls:

$$u_{\text{wall}} = v_{\text{wall}} = 0 \tag{26}$$

At the inlet, a uniform axial velocity is specified:

$$u_{\text{inlet}} = V \tag{27}$$

At the outlet, a zero-gauge pressure condition is imposed to allow the flow to adjust naturally within the computational domain:

$$P_{\text{outlet}} = 0 \tag{28}$$

Accordingly, the overall pressure drop across the pipe is obtained directly from the inlet pressure:

$$\Delta P = P_{\text{inlet}} \tag{29}$$

The mesh design, near-wall treatment, and boundary conditions described above establish a consistent numerical framework for resolving the dominant

flow features in corrugated pipes. When combined with the turbulence modeling strategy outlined in Section 6.4, this approach enables reliable prediction of pressure losses and supports subsequent analysis of flow physics and energy dissipation mechanisms.

6.6 Numerical Solution Procedure, Convergence, and Smooth-Pipe Verification

The numerical simulations are carried out using a commercial finite-volume solver, ANSYS Fluent. The governing equations are discretized over the computational domain and reduced to a system of coupled algebraic equations, which are solved iteratively. For incompressible flows, a pressure–velocity coupling algorithm is required; accordingly, SIMPLE-type schemes are employed, as they are widely used and well established for internal flow applications.

Convergence of the numerical solution is assessed by monitoring the variation of flow variables between successive iterations. The velocity error vector is defined as

$$e_u = \begin{bmatrix} | u_i - u_{i-1} | \\ | v_i - v_{i-1} | \end{bmatrix} \tag{30}$$

The continuity residual is evaluated as

$$e_s = | \frac{\partial u_i}{\partial x} + \frac{\partial v_i}{\partial y} | \tag{31}$$

and an analogous error measure is introduced for the turbulence transport variables:

$$e_t = \begin{bmatrix} | \varepsilon_i - \varepsilon_{i-1} | \\ | k_i - k_{i-1} | \end{bmatrix} \tag{32}$$

A numerically consistent and converged solution is obtained when all error measures asymptotically approach zero, i.e.,

$$i \to \infty \;\Rightarrow\; e_u \to 0,\; e_s \to 0,\; e_t \to 0 \tag{33}$$

In addition to residual-based criteria, the inlet pressure is monitored during the iterative process. The inlet pressure is computed as an area-averaged quantity,

$$P_{\text{inlet}} = \frac{1}{A} \int P \, dA \tag{34}$$

and convergence is accepted once this value stabilizes to at least five significant digits.

To verify the numerical framework, a validation study is performed for a smooth straight pipe having the same inner diameter and length as the corrugated configuration. The numerically predicted pressure drop is compared against the analytical estimate based on the Colebrook equation. For hydraulically smooth pipes, the Colebrook relation reduces to the Prandtl form:

$$\frac{1}{\sqrt{f}} = 2.0\log\left(Re\sqrt{f}\right) - 0.8 \tag{35}$$

This implicit relation is solved using a fixed-point iteration scheme,

$$f_{i+1} = \left(\frac{1}{2.0\log\left(Re\sqrt{f_i}\right)-0.8}\right)^2 \tag{36}$$

For the considered flow conditions, the friction factor converges to

$$f = 0.0205 \tag{37}$$

Using this value, the friction head loss and corresponding pressure drop are obtained as

$$h_f = 331.3273 \tag{38}$$

$$\Delta P = 3980 \text{ Pa} \tag{39}$$

The relative deviation between the numerical and analytical pressure drops is quantified by

$$h = 100\frac{\Delta P - \Delta P_S}{\Delta P} \tag{40}$$

and is found to be approximately **0.05%**. This very small discrepancy confirms that the numerical methodology, mesh strategy, and solution procedure accurately reproduce the classical smooth-pipe benchmark, thereby providing a reliable foundation for the subsequent analysis of corrugated pipe flows.

6.7 Corrugated Pipe Simulation and Mesh Independence (Compact Form)

To ensure stable convergence in turbulent simulations, the inlet turbulence level is explicitly specified. Turbulence intensity is defined as:

$$I = \frac{u'}{U} \tag{41}$$

and may be estimated as a function of the Reynolds number according to [27]:

$$I = 0.16Re^{-1/8} \tag{42}$$

For the present operating condition, corresponding to $Re = 5.41 \times 10^4$, the inlet turbulence intensity is obtained as

$$I = 0.0410 \tag{43}$$

which corresponds to approximately 4.1%, a value consistent with turbulent internal flows in geometrically complex ducts.

The corrugated pipe configuration is solved on multiple meshes to assess mesh independence. Rather than reporting the results in several separate tables, a compact summary is provided in **Table 1**, where the pressure drop is reported as a function of total cell count.

Table 1. Mesh-independence summary for the corrugated pipe (2D), showing stabilization of pressure drop.

Total cells	**ΔP(Pa)**	**ΔP(kPa)**	**Deviation from finest (%)**
1,426,000	20,802	20.80	0.91
2,566,800	20,953	20.95	0.19
2,852,000	20,980	20.98	0.06
3,137,200	21,005	21.01	0.06
3,422,400	20,992	20.99	0.00

The results indicate that the predicted pressure drop varies within approximately ±1% over the investigated mesh range and stabilizes around $\Delta P \approx 21$ kPa. This behavior confirms that the numerical solution is effectively mesh-independent for practical engineering purposes.

For comparison, a smooth pipe of identical length and diameter yields a pressure drop of approximately 4 kPa under the same flow conditions. The corrugated pipe therefore exhibits a pressure-loss increase by a factor of about **5.25**, clearly illustrating the severe hydraulic penalty associated with corrugation-induced flow disturbances.

To further contextualize the numerical results, the same geometry and flow conditions are inserted into the Hawthorne and von Helms correlation [14], yielding

$$\Delta P = 29.2 \text{ kPa} \tag{44}$$

This value differs from the CFD prediction (≈21 kPa) by approximately 28%. Considering that uncertainty levels on the order of ±30% are commonly reported for such simplified correlations, the present numerical result remains well within a plausible and physically consistent range.

Expressing the pressure drop in terms of the Darcy friction factor,

$$\frac{\Delta P}{\rho g} = f \frac{L}{d} \frac{V^2}{2g} \tag{45}$$

Yields

$$f = 0.11 \tag{46}$$

This value is substantially higher than typical friction factors for smooth pipes and is fully consistent with the strong energy dissipation caused by corrugation-induced flow separation, recirculation, and secondary flow structures.

7. Results and Flow PhysicsInterpretation

7.1 Global Pressure Loss Characteristics

The numerical results clearly demonstrate that corrugated pipes exhibit substantially higher pressure losses than geometrically equivalent smooth pipes operating under identical flow conditions. For the reference case considered in this study, the pressure drop across the corrugated pipe is approximately 21 kPa, whereas the corresponding smooth pipe yields a pressure loss of about 4 kPa. This corresponds to an increase by a factor of approximately 5.25, highlighting the severe hydraulic penalty associated with corrugated geometries.

This difference cannot be attributed solely to an increase in effective surface roughness. Instead, the dominant contribution arises from the repeated contraction–expansion sequence imposed by the corrugation pattern, which fundamentally alters the momentum balance of the flow. Each groove introduces a localized disturbance that disrupts the near-wall flow, promotes separation, and inhibits the establishment of a fully developed velocity profile comparable to that observed in smooth pipes. As a result, additional irreversible losses accumulate progressively along the pipe length.

From a global energy perspective, the elevated pressure loss directly translates into increased pumping power requirements. Consequently, even relatively short sections of corrugated pipe may dominate the overall hydraulic resistance of a system, particularly in compact installations or applications involving flexible connections. This observation is consistent with practical engineering experience, where corrugated pipes are often regarded as hydraulically inefficient despite their mechanical and installation advantages.

7.2 Velocity Field and Groove-Induced Separation

An examination of the velocity field reveals that the flow structure in corrugated pipes differs fundamentally from that in smooth pipes. As the fluid enters a groove region, the near-wall flow decelerates rapidly due to the sudden local expansion, leading to flow separation at the upstream edge of the corrugation. The separated shear layer spans across the groove cavity, while a low-velocity recirculation zone develops inside the groove.

Downstream of each groove, partial flow reattachment occurs before the fluid encounters the next corrugation. However, the reattachment length is limited, and the boundary layer does not fully recover to a classical fully developed state. Instead, the flow undergoes repeated cycles of separation and reattachment along the axial direction, resulting in a spatially periodic velocity field.

This repeated disruption has two important consequences. First, momentum exchange between the core flow and the near-wall region is significantly enhanced, leading to increased average wall shear stress. Second, the persistence of separated regions suppresses the formation of a stable logarithmic velocity profile typical of smooth-wall turbulent pipe flow. As a result, velocity gradients remain elevated over a larger portion of the cross-section, directly contributing to the observed increase in pressure loss.

These groove-induced separation mechanisms form the physical basis for the complex hydrodynamic behavior observed in corrugated pipes and explain why classical smooth-pipe correlations fail to predict their hydraulic performance accurately.

7.3 Reynolds Number Dependence and Non-Classical Friction Behavior

One of the most distinctive features of corrugated pipe flows is their non-classical dependence on Reynolds number. In smooth pipes, increasing Reynolds number typically leads to a monotonic decrease in the friction factor, which eventually approaches an asymptotic value in the fully turbulent regime. Corrugated pipes, however, exhibit a markedly different trend.

The numerical results indicate that, beyond the onset of fully turbulent flow, the friction factor does not continue to decrease monotonically with increasing Reynolds number. Instead, it may reach an approximately constant level over a certain range and subsequently exhibit a renewed increase at higher Reynolds numbers. This behavior is consistent with experimental observations reported in the literature and cannot be captured by conventional smooth-pipe or rough-pipe correlations.

The underlying reason lies in the scaling behavior of groove-induced flow structures. As the bulk velocity increases, the strength and persistence of separation zones and secondary vortical motions within the grooves also increase. Rather than becoming dynamically insignificant at high Reynolds numbers, these structures extend further into the core flow region, sustaining enhanced turbulence production and additional momentum losses. Consequently, Reynolds number similarity alone is insufficient to ensure dynamic similarity in corrugated pipe flows.

This breakdown of classical Reynolds-number-based similarity highlights a fundamental limitation of applying standard friction-factor correlations, such as those derived from the Moody diagram or the Colebrook equation, to corrugated geometries. It further underscores the necessity of geometry-resolved numerical or experimental approaches when reliable pressure-loss predictions are required.

7.4 Engineering Implications and Practical Interpretation

From an engineering design perspective, the results presented in this chapter emphasize the substantial influence of corrugation geometry on hydraulic performance. The approximately fivefold increase in pressure loss observed for the corrugated pipe, relative to a smooth pipe of identical length and nominal diameter, implies a corresponding increase in required pumping power. In practical systems, this increase may dominate overall energy consumption, particularly when corrugated pipes are used in extended lengths or in configurations involving multiple flexible connections.

A key implication is that corrugated pipes cannot be treated as direct substitutes for smooth pipes through the simple adjustment of an equivalent roughness parameter. Classical design tools based on smooth- or uniformly rough-pipe correlations are unable to capture the combined effects of groove-induced separation, secondary flows, and repeated flow reattachment. As a result, reliance on such correlations may lead to significant uncertainty in pressure-loss estimates.

In engineering practice, designers often depend on manufacturer-provided pressure-drop data or apply conservative safety margins. While this approach may ensure operational reliability, it can also result in oversized pumping systems and reduced energy efficiency. The findings of this study suggest that geometry-resolved numerical analysis offers a valuable complementary tool, providing both quantitative predictions and physical insight into the mechanisms responsible for energy dissipation.

More broadly, the results highlight the necessity of balancing the mechanical advantages of corrugated pipes—such as flexibility, vibration attenuation, and ease of installation—against their inherent hydraulic penalties. A clear understanding of this trade-off is essential for optimizing system performance and for guiding the development of improved corrugation designs with reduced energy losses.

Summary of Key Findings

The results presented in this chapter demonstrate that flows in corrugated pipes are governed by hydrodynamic mechanisms fundamentally different from those observed in smooth pipes. Groove-induced flow separation, persistent secondary vortical structures, and repeated disruption of boundary-layer development collectively lead to substantially higher pressure losses and a non-classical dependence on Reynolds number. These effects cannot be adequately captured by conventional friction-factor correlations, underscoring the need for geometry-resolved numerical or experimental analysis when reliable hydraulic performance predictions are required.

8. Conclusions and Outlook

This chapter presents a comprehensive numerical investigation of turbulent flow and pressure losses in corrugated pipes, with particular emphasis on the physical mechanisms responsible for their elevated hydraulic resistance. By revisiting classical smooth-pipe theory and systematically extending it to corrugated geometries, it has been demonstrated that pressure losses in corrugated pipes are governed not only by surface roughness effects, but also

by groove-induced flow separation, secondary motions, and the repeated disruption of boundary-layer development.

The numerical results confirm that corrugated pipes exhibit substantially higher-pressure losses than smooth pipes of identical nominal dimensions. For the configuration investigated, the pressure drop is increased by a factor of approximately five, a result that is closely linked to the persistence of vortical structures within the corrugation grooves and to a non-classical dependence of the friction factor on Reynolds number. These findings clearly indicate that conventional design correlations developed for smooth or uniformly rough pipes are insufficient for reliable hydraulic performance prediction in corrugated geometries.

From an engineering standpoint, the results underscore the importance of explicitly accounting for corrugation-induced energy penalties in pump selection and system design. Although corrugated pipes offer significant mechanical and installation advantages, their hydraulic behavior requires careful evaluation, particularly in applications where energy efficiency and long-term operating costs are of primary concern.

Looking ahead, the present results provide a solid foundation for further research aimed at improving the hydraulic performance of corrugated pipes. Future studies may extend the analysis to fully three-dimensional configurations, investigate alternative corrugation geometries with reduced pressure-loss penalties, or integrate high-fidelity numerical simulations with targeted experimental validation. Such efforts would support the development of more energy-efficient flexible pipe solutions and contribute to the establishment of more reliable and physically consistent design guidelines for corrugated pipe systems.

References

[1]. Witzenmann GmbH, *Metal Hose Handbook*, Witzenmann Group, Germany, 2015.
[2]. Srinivasan, B., Idem, S. A., "Pressure drop testing of corrugated stainless steel pliable gas tubing (PLT)," *Proceedings of ASME IMECE*, USA, 2014.
[3]. Gibson, A. H., "The flow of water in a corrugated pipe," *Philosophical Magazine*, vol. 49, pp. 161–173, 1925.
[4]. Webster, M. J., Metcalf, L. R., "Friction factors in corrugated metal pipe," *Journal of the Hydraulics Division*, ASCE, vol. 85, pp. 1–24, 1959.
[5]. Allen, J., "Flow of incompressible fluids through corrugated pipes," *Proceedings of the Institution of Civil Engineers*, vol. 29, pp. 205–220, 1964.
[6]. Weisend II, J. G., Van Sciver, S. W., "Pressure drop from flow of cryogens in corrugated bellows," *Cryogenics*, vol. 30, pp. 685–690, 1990.
[7]. Bernhard, D. M., Hsieh, C. K., "Pressure drop in corrugated pipes," *Journal of Fluids Engineering*, ASME, vol. 118, pp. 812–818, 1996.

[8]. Dizaji, H. S., et al., "Experimental studies on heat transfer and pressure drop characteristics for corrugated tubes," *International Journal of Thermal Sciences*, vol. 95, pp. 15–24, 2015.
[9]. Colebrook, C. F., "Turbulent flow in pipes," *Journal of the Institution of Civil Engineers*, vol. 11, pp. 133–156, 1939.
[10]. Haaland, S. E., "Simple and explicit formulas for the friction factor in turbulent pipe flow," *Journal of Fluids Engineering*, vol. 105, pp. 89–90, 1983.
[11]. Ahmed, S., Islam, M. Q., Jonayat, A. S. M., "Determination of loss coefficient for flow through flexible pipes," *Experimental Thermal and Fluid Science*, vol. 42, pp. 48–55, 2012.
[12]. Ahn, H., Uslu, I., "Experimental investigation on pressure drop in corrugated pipes," *Proceedings of ASME IMECE*, USA, 2013.
[13]. Popiel, C. O., et al., "Friction factor for transient flow in transversely corrugated pipes," *Journal of Fluids Engineering*, vol. 135, 041202, 2013.
[14]. Calomino, F., et al., "Experimental and numerical study on the flow field and friction factor in a pressurized corrugated pipe," *Journal of Hydraulic Engineering*, vol. 141, 04015027, 2015.
[15]. Hawthorne, R. C., von Helms, H. C., "Flow in corrugated hose," *Product Engineering*, vol. 34, pp. 56–61, 1963.
[16]. Kauder, K., *Dissipation inkompressibler Medien in Rohrleitungen*, PhD Thesis, Germany, 1974.
[17]. Riley, K. L., *Flow Losses in Flexible Hose*, Technical Report, USA, 1967.
[18]. Srinivasan, B., Idem, S. A., "Pressure drop testing of corrugated stainless steel pliable gas tubing," *ASME*, 2015.
[19]. Li, Y., et al., "Pressure drop and friction factor of slush nitrogen turbulent flow in helically corrugated pipes," *Cryogenics*, vol. 94, pp. 50–59, 2018.
[20]. Nikuradse, J., "Laws of flow in rough pipes," *NACA Technical Memorandum 1292*, 1950.
[21]. White, F. M., *Fluid Mechanics*, McGraw-Hill, New York, 1990.
[22]. Al-Obaidi, A. R., "Dynamic simulation of thermo-hydraulic flow in corrugated pipes under various geometrical configurations," *Journal of Thermal Analysis and Calorimetry*, vol. 149, pp. 9663–9688, 2024. https://doi.org/10.1007/s10973-024-13467-z
[23]. Chaurasiya, P. K., et al., "Numerical exploration of heat transfer and friction factor in corrugated dual-pipe heat exchangers using nanofluids," *Thermal Science and Engineering Progress*, vol. 56, 103076, 2024. https://doi.org/10.1016/j.tsep.2024.103076
[24]. Al-Obaidi, A. R., "Comparative investigation of novel thermo-hydraulic flow characteristics and heat efficiency enhancement in 3D corrugated pipes," *Heat Transfer*, vol. 54, no. 3, pp. 2165–2183, 2025. https://doi.org/10.1002/htj.23286
[25]. Balkan, F., *Determination of Friction Factor for Different Flow Conditions in Stainless Steel Transversely Corrugated Flexible Pipes*, Master's Thesis, Graduate School of Natural and Applied Sciences, Manisa Celal Bayar University, Manisa, Türkiye, 2023.
[26]. X Dong, Y., Huixiong, L., & Tingkuan, C. (2001). Pressure drop, heat transfer and performance of single-phase turbulent flow in spirally corrugated tubes. *Experimental Thermal and Fluid Science*, *24*(3-4), 131-138.

[27]. Y A. B. Aksoy, F. B. Balkan, E. Polat, Z. Coşkun, “Paslanmaz Çelik Enine Oluklu Esnek Borularda Farklı Akış Koşulları İçin Isı İletim Performansı (Heat Transfer Performance in Stainless Steel Transversely Corrugated Flexible Pipes for Different Flow Conditions),” in *15. Ulusal Tesisat Mühendisliği Kongresi*, İzmir, Türkiye, 16-19 Nisan 2025. pp. 645–657.

The Effect of Micro-Glass Fibre Reinforcement on the Bending Properties of Unsaturated Polyester Composites

Nisan YEŞİL[1]

Hüseyin ÜNAL[2]

1- Metalurji ve Malzeme Müh.; Subor Boru San ve Tic. AŞ. nisan.kuyumcu@subor.com.tr ORCID No: 0000-0001-9279-4976

2- Prof. Dr.; Sakarya Uygulamalı Bilimler Üniversitesi Teknoloji Fakültesi Metalurji ve Malzeme Mühendisliği Bölümü. unal@subu.edu.tr ORCID No: 0000-0003-0521-6647

ABSTRACT

This study investigates the influence of micro-glass fiber reinforcement on the mechanical behaviour of unsaturated polyester (UPE) composites at various fiber loadings. Neat UPE exhibits relatively low stiffness and moderate flexibility; however, the addition of micro-glass fibers significantly alters its mechanical response. Increasing the fiber content to 20-50 wt.% results in a noticeable enhancement in flexural strength, indicating improved load-transfer capability between the matrix and the reinforcing fibers. The most pronounced improvement is observed in flexural modulus, where stiffness increases dramatically with higher fiber fractions, reflecting a transition from matrix-controlled to fiber-dominated structural performance. In parallel, the surface hardness of the composites rises substantially due to the rigid and incompressible nature of the glass fibers, which restrict indentation and improve resistance to localized deformation. Conversely, flexural strain decreases sharply as fiber content increases, revealing a reduction in ductility resulting from constrained polymer mobility and intensified fiber-fiber interactions. The results demonstrate that micro-glass fiber reinforcement effectively enhances the rigidity, strength, and hardness of UPE, making the composites suitable for applications requiring high stiffness and dimensional stability, while acknowledging the associated decline in flexibility.

Keywords – Unsaturated polyester, Micro-glass fiber, thermoset, composite, mechanical properties.

INTRODUCTION

Unsaturated polyester (UPE) resins remain one of the most widely used thermosetting matrices in polymer composite technology due to their relatively low cost, ease of processing, adjustable curing behaviour, and good chemical resistance. These characteristics make UPE-based materials particularly attractive for applications in the automotive, marine, construction, and infrastructure sectors. Chemically, UPE resins are typically synthesized through the polycondensation reaction of unsaturated dicarboxylic acids such as maleic anhydride or fumaric acid with diols such as propylene glycol and are commonly dissolved in styrene, which acts as a reactive diluent. During curing, a free-radical polymerization reaction forms a three-dimensional crosslinked network, giving the material a rigid thermoset structure that cannot be remelted upon heating (Strong, 2008; Osswald & Menges, 2012). The density of unsaturated polyester resins generally ranges between 1.1 and 1.3 g/cm³, which is significantly lower than that of many metallic materials. Their glass transition temperature (Tg) typically falls within the range of 60–120 °C, and due to the crosslinked

structure they do not exhibit a true melting temperature but rather degrade at elevated temperatures (Callister & Rethwisch, 2020). Although UPE resins offer good corrosion resistance and electrical insulation properties, their intrinsic mechanical limitations particularly moderate stiffness and relatively limited flexural load-bearing capacity often necessitate the use of reinforcement materials to broaden their structural applications (Mallick, 2007).

Among the available reinforcement materials, glass fibers are widely preferred for polyester matrices due to their high elastic modulus, good tensile strength, favorable strength-to-cost ratio, and compatibility with polymer matrices. Glass fibers are produced by melting silica-based raw materials and drawing the molten glass into very fine filaments. Their chemical composition typically includes silicon dioxide (SiO_2), aluminum oxide (Al_2O_3), calcium oxide (CaO), and boron oxide (B_2O_3), and their density generally ranges between 2.4 and 2.6 g/cm³. Glass fibers exhibit tensile strengths typically between 2000 and 3500 MPa and elastic moduli of approximately 70-90 GPa, providing excellent reinforcement capability for polymer composites (Mallick, 2007; Strong, 2008). Depending on their composition and intended application, several types of glass fibers exist, including E-glass, S-glass, C-glass, and alkali-resistant (AR) glass fibers (Osswald & Menges, 2012). When incorporated into UPE matrices in chopped or continuous forms, glass fibers significantly enhance the mechanical performance of the composite by carrying an increasing portion of the applied load as the fiber content increases, which typically results in improvements in flexural modulus and flexural strength provided that adequate fiber dispersion and fiber–matrix adhesion are achieved (Romanzini D., 2013; Jariwala H., 2020).

In addition to conventional glass fibers, glass fiber powder (also referred to as milled glass fiber) has also been widely used as a micro-scale reinforcement or filler in polymer composites. Glass fiber powder is produced by mechanically grinding or milling continuous or chopped glass fibers into short lengths ranging from a few micrometers to several hundred micrometers. Similar to continuous glass fibers, glass fiber powders possess good hardness, chemical stability, and electrical insulation properties. When incorporated into polymer matrices such as unsaturated polyester or epoxy systems, they can enhance surface hardness, wear resistance, dimensional stability, and overall mechanical performance (Callister & Rethwisch, 2020; Mallick, 2007). Moreover, the presence of micro-sized glass fibers within the matrix may improve load transfer and reduce void formation when appropriate dispersion and processing conditions are achieved (Osswald & Menges, 2012). However, the extent of property enhancement strongly depends on several microstructural parameters, including fiber weight fraction, fiber length distribution, fiber orientation, fiber–matrix interfacial bonding, and processing method. Surface treatments such as silane coupling

agents are frequently used to improve interfacial adhesion and enhance stress transfer efficiency between the fiber and the polymer matrix (Assunção G.S.C., 2024; Nallaiya, G., 2022).

While the addition of glass fibers or micro-glass fibers generally leads to significant increases in stiffness, hardness, and load-bearing capacity, it may also introduce certain mechanical trade-offs. In particular, increasing fiber content often reduces the ductility of the composite, as the rigid fibers restrict the mobility of polymer chains and facilitate earlier initiation of microcracks under mechanical loading. This phenomenon typically results in a reduction in strain-to-failure or flexural strain, illustrating the classical stiffness–ductility trade-off commonly observed in short-fiber-reinforced thermoset composites (Boukhoulda A., 2024; Tarikul H., 2024). Therefore, optimizing the fiber content and distribution within the polymer matrix is essential to achieve a balanced combination of stiffness, strength, and toughness in UPE-based composite materials.

Considering the increasing industrial demand for lightweight yet mechanically robust materials and the growing body of research on unsaturated polyester composites, a systematic evaluation of the influence of micro-glass fiber reinforcement on key mechanical properties is of considerable importance. In particular, understanding how varying micro-glass fiber weight fractions affect flexural strength, flexural modulus, hardness, and flexural strain can provide valuable insights into the structure–property relationships governing these materials. Therefore, this study aims to investigate the mechanical performance of unsaturated polyester composites reinforced with different weight fractions of micro-glass fibers, with the objective of elucidating the mechanisms responsible for the observed trends and providing guidance for the design of high-performance polyester-based composite systems.

EXPERIMENTAL

Materials and Preparation of Composites

The production flow chart for polyester/glass fibre composite is shown in Figure 1 below. In the study, composite specimens were produced by incorporating different weight fractions (20, 30, 35, and 50 wt.%) of reinforcing additives into an unsaturated polyester matrix and casting the mixtures into silicone moulds. Flexural and hardness test specimens were fabricated using specially designed silicone rubber moulds prepared in accordance with relevant ISO standards. During the composite fabrication process, a predetermined amount of liquid polyester resin was first poured into a glass beaker. Subsequently, glass fiber powder was gradually added to the resin at the specified weight ratios (20-50 wt.%), and the mixture was homogenized using a mechanical stirrer for approximately 60 minutes to

ensure a uniform dispersion of the reinforcement within the matrix. After obtaining a homogeneous mixture, 1.0 wt.% of the curing agent Methyl Ethyl Ketone Peroxide was introduced and mixed for about 30 seconds. The resulting mixture was then poured into the silicone moulds. The curing agent was used to initiate crosslinking and hardening of the thermoset polyester resin. The moulded samples were initially kept in the moulds at room temperature for approximately 8-10 hours to allow primary curing. Subsequently, the specimens were post-cured in an oven at 80 °C for 7-8 hours to complete the crosslinking process. Finally, the samples were conditioned for 24 hours at 23 °C and 50% relative humidity before testing. Both the polyester resin and the curing agent used in this work were supplied by Boytek, located in Istanbul.

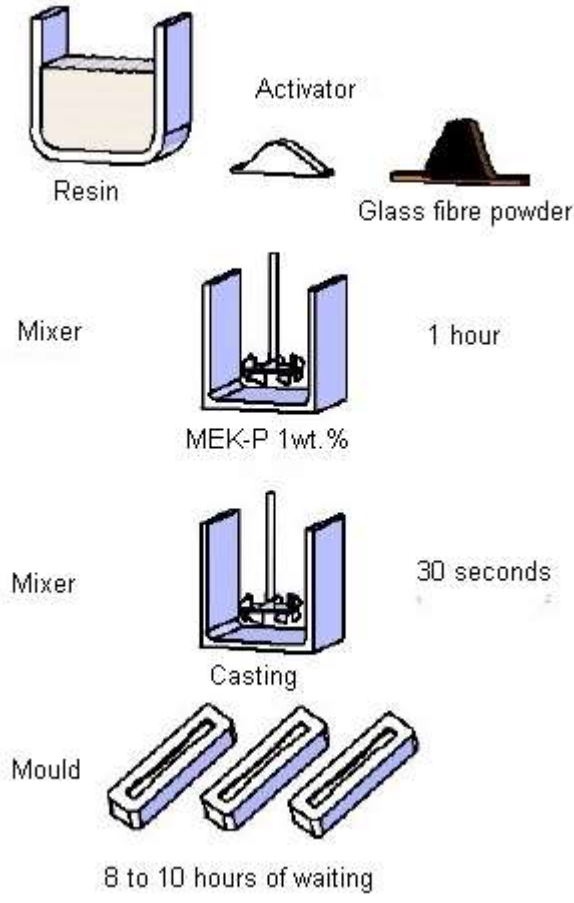

Figure 1. Schematic composite production flow diagram

Mechanical Tests

Bending Test

The flexural properties of glass fiber reinforced unsaturated polyester composites were evaluated using a three-point bending test. The experiments were performed in accordance with the procedures described in the ASTM D790 standard. Rectangular specimens were prepared with typical dimensions of approximately 127 mm in length, 12.7 mm in width, and about 4 mm in thickness. During the test, each specimen was placed on two supports with a defined span length, and the load was applied at the midpoint using a universal testing machine. The crosshead speed was set to 5 mm/min to ensure a controlled and uniform deformation rate throughout the experiment. As the load increased, the specimen experienced bending until failure or until the maximum flexural load was reached. The applied force and corresponding deflection values were continuously recorded to determine the flexural strength and flexural modulus of the composite material. This method provides a reliable assessment of the bending behaviour and structural performance of fiber-reinforced polymer composites.

RESULTS AND DISCUSSION

Figure 2 presents the variation in flexural strength of neat unsaturated polyester and micro-glass-fiber-reinforced UPE composites at reinforcement levels of 20, 30, 35 and 50 wt.%. The flexural strength of the neat resin was measured as 63.9 MPa, whereas incorporating 20, 30, 35, and 50 wt.% micro-glass fibers resulted in strengths of 70.9, 70.3, 67.9, and 70.6 MPa, respectively. These values correspond to increases of approximately 10.9% (20 wt.%), 10.0% (30 wt.%), 6.3% (35 wt.%), and 10.5% (50 wt.%) relative to the unreinforced polymer. The improvement in flexural performance at all reinforcement levels primarily arises from the effective stress transfer between the polyester matrix and the micro-glass fibers. The rigid, high-modulus glass fibers restrict matrix deformation under bending, thereby enhancing the composite's resistance to tensile and compressive stresses. The highest relative improvement is observed at 20 wt.% and 50 wt.% fiber loading, which indicates that at these concentrations the fiber distribution and fiber- matrix interfacial adhesion are sufficiently optimized to promote efficient load bearing. In contrast, the slightly lower improvement observed at 35 wt.% may be associated with increased fiber fiber interactions, reduced wetting of fibers due to matrix insufficiency, or the formation of localized stress concentrations. Such microstructural effects can limit the effective load transfer capacity, leading to marginally lower flexural strength despite

the higher fiber content. Nonetheless, the overall results demonstrate that micro-glass fiber reinforcement consistently enhances the stiffness and load-carrying capability of UPE, confirming the beneficial role of short-fiber dispersion in improving flexural performance

Figure 3 illustrates the variation in flexural modulus of neat unsaturated polyester and micro-glass-fiber-reinforced UPE composites at reinforcement contents of 20, 30, 35, and 50 wt.%. The flexural modulus of the neat resin was 2020 MPa**,** whereas the incorporation of 20, 30, 35, and 50 wt.% micro-glass fibers resulted in modulus values of 2940, 5000, 5260, and 7680 MPa**,** respectively. These correspond to substantial increases of approximately 45.5% (20 wt.%), 147.5% (30 wt.%), 160.6% (35 wt.%), and 280% (50 wt.%) relative to unreinforced UPE. The pronounced enhancement in flexural modulus with increasing fiber loading reflects the dominant stiffness contribution of the micro-glass fibers, whose elastic modulus is significantly higher than that of the polyester matrix. As the fiber content increases, the composite's deformation under bending becomes increasingly governed by the rigid fibers rather than the relatively compliant polymer phase.

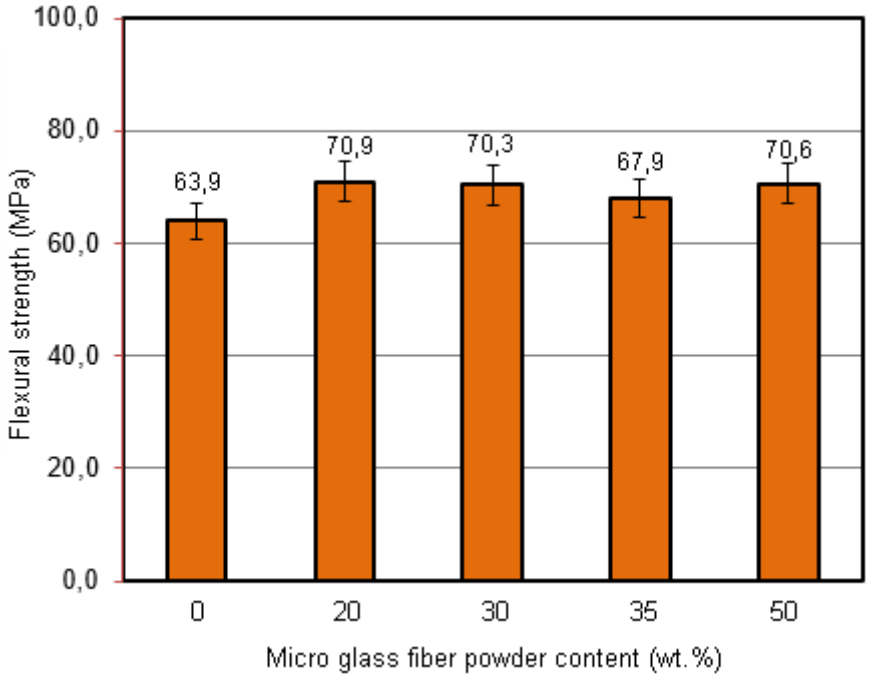

Figure 2. Change in flexural strength of pure unsaturated polyester and UPE composites containing micro glass fibres at different ratios (from 20wt.% to 50wt.%).

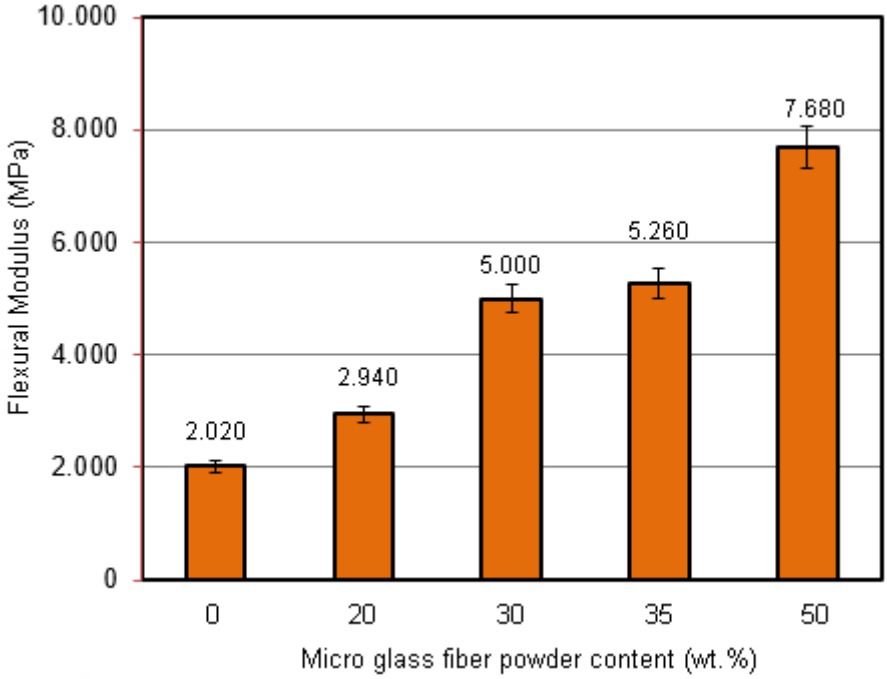

Figure 3. Change in the Flexural Modulus of pure unsaturated polyester and UPE composites containing micro glass fibres at different ratios (from 20% to 50%).

This transition results in a near-linear to super-linear improvement in modulus, particularly beyond 30 wt.% reinforcement, where fiber-fiber proximity reduces matrix continuity and further restricts strain accommodation. The sharp increase at 50 wt.% fiber loading can be attributed to the formation of a more continuous fiber network, which enables more efficient stress transfer and minimizes matrix-dominated deformation. Additionally, higher fiber volume fractions tend to reduce shear lag effects, thereby allowing the fibers to bear a larger portion of the applied load. Generally, the results confirm that micro-glass fiber addition is highly effective in increasing the stiffness of UPE, and the degree of improvement becomes more pronounced as the reinforcement content approaches fiber-dominated structural behaviour.

Figure 4 shows the variation in Barcol hardness of neat unsaturated polyester and micro-glass-fiber-reinforced UPE composites at reinforcement levels of 20, 30, 35, and 50 wt.%. The hardness of the neat resin was 22**,** whereas the incorporation of 20, 30, 35, and 50 wt.% micro-glass fibers resulted in values of 44, 48, 49, and 52, respectively. These correspond to notable increases of approximately 100% (20 wt.%), 118% (30 wt.%), 123% (35 wt.%), and 136% (50 wt.%) compared to the unreinforced polymer. The substantial increase in Barcol hardness with increasing fiber content is primarily attributed to the inherently high rigidity and surface resistance of

the micro-glass fibers. As the fiber loading rises, the composite surface becomes progressively dominated by the stiff, incompressible glass particles, reducing the extent of localized indentation under the hardness probe. In addition, the presence of hard, non-deformable fibers restricts the mobility of the polyester chains near the surface, resulting in a more constrained polymer network that resists penetration more effectively. The modest but consistent increase from 30 wt.% to 50 wt.% suggests that higher fiber fractions not only reinforce the bulk matrix but also contribute to the formation of a harder microstructural skeleton near the composite surface. This microstructural densification reduces the effective indentation depth and enhances the composite's resistance to permanent deformation. Overall, the results demonstrate that micro-glass fiber reinforcement markedly improves surface hardness, with improvements becoming more pronounced as the composite transitions toward fiber-dominated mechanical behaviour.

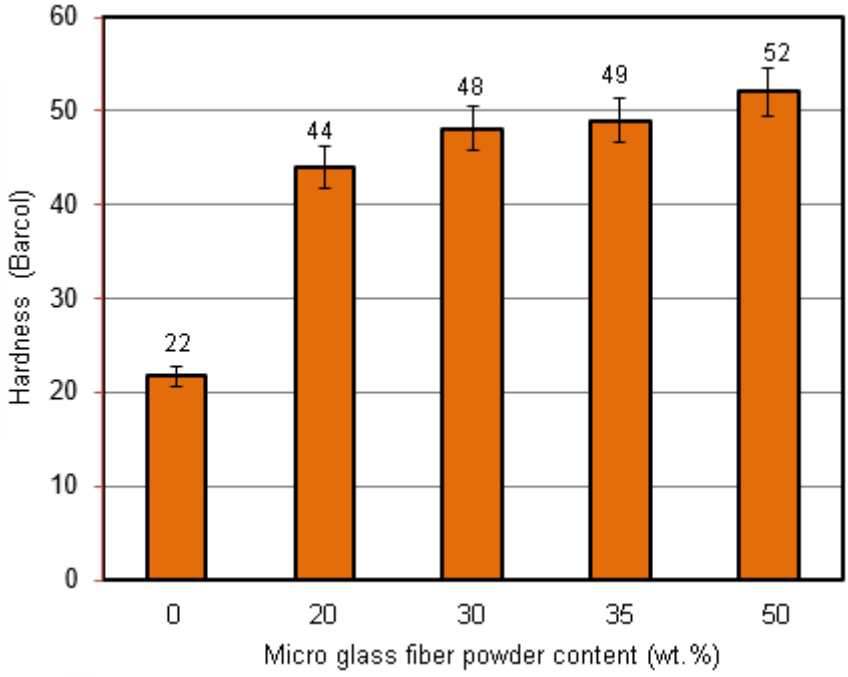

Figure 4. Change in hardness of pure unsaturated polyester and UPE composites containing micro glass fibres at different ratios (from 20% to 50%).

Figure 5 presents the variation in flexural strain of neat unsaturated polyester and micro-glass-fiber-reinforced UPE composites at reinforcement levels of 20, 30, 35, and 50 wt.%. The flexural strain of neat UPE was 6.8%, whereas the incorporation of 20, 30, 35, and 50 wt.% micro-glass fibers resulted in markedly lower strain values of 3.0%, 1.4%, 1.4%, and 0.88%, respectively. These correspond to substantial reductions of approximately

55.9% (20 wt.%), 79.4% (30 wt.%), 79.4% (35 wt.%), and 87.1% (50 wt.%) relative to the unreinforced polymer.

The significant decrease in flexural strain with increasing fiber content is primarily attributed to the inherently brittle and high-stiffness nature of micro-glass fibers. As reinforcement levels increase, the composite structure becomes progressively less capable of accommodating large deformations, since the added fibers restrict matrix mobility and limit the overall ductility of the material. This reduction in strain capacity is consistent with the classical behaviour of short-fiber reinforced thermoset composites, where stiffness enhancement typically comes at the expense of flexibility. At higher reinforcement levels (≥30 wt.%), the strain values converge to very low levels, indicating a transition toward fiber- dominated mechanical behaviour. At these concentrations, fiber-fiber interactions become more pronounced, further constraining the matrix and promoting earlier onset of micro-crack formation under bending. The lowest strain observed at 50 wt.% reflects the formation of a highly rigid composite structure in which the matrix contribution to deformation is minimal, leading to a pronounced decrease in the composite's ability to sustain tensile strain on the outer surface during flexural loading.

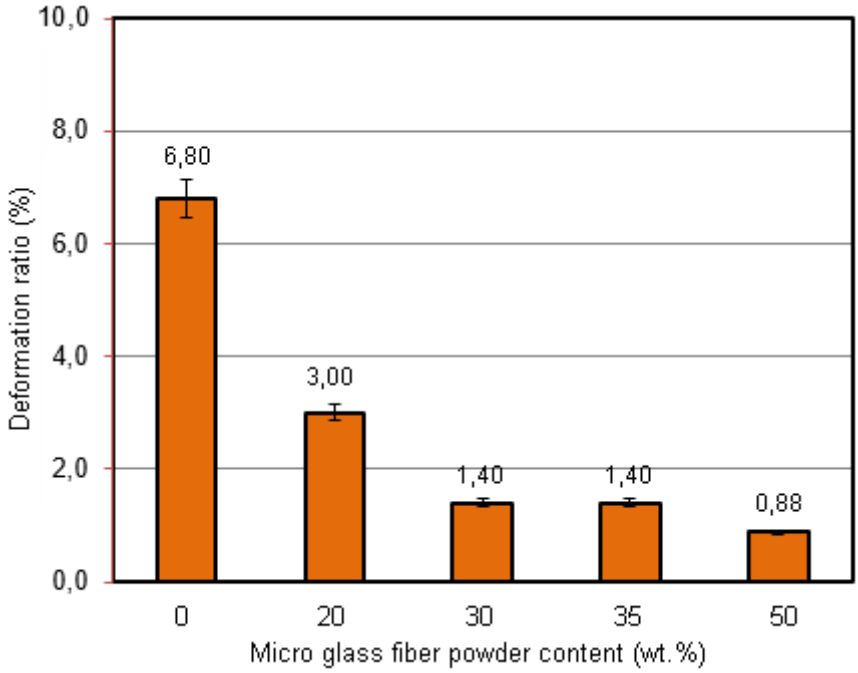

Figure 5. Change in the deformation ratio of pure unsaturated polyester and UPE composites containing micro glass fibres at different ratios (from 20% to 50%).

The results clearly demonstrate the expected trade-off between stiffness and deformability: while micro-glass fibers significantly enhance modulus and hardness, they simultaneously reduce the composite's strain capacity due to diminished matrix continuity and increased brittleness. Based on the information obtained above, a brief summary can be explained as follows.

The change in the deformation ratio of UPE composites containing pure unsaturated polyester and micro glass fibres in varying proportions (from 20wt.% to 50wt.%) is shown in Figure 5. The mechanical characterization of neat UPE and micro-glass-fiber-reinforced UPE composites demonstrates a consistent trend in which increasing fiber content enhances load-bearing capacity while reducing deformability. Flexural strength increased moderately with reinforcement, rising from 63.9 MPa for neat UPE to 70.9-70.6 MPa across the 20-50 wt.% fiber range. This improvement stems from more efficient stress transfer from the matrix to the stiff micro-glass fibers, which suppress matrix cracking under bending. A much more pronounced enhancement was observed in flexural modulus, which increased from 2020 MPa to 2940-7680 MPa as the fiber content increased. This large stiffness gain reflects the high elastic modulus of the glass fibers and the progressive shift from matrix dominated to fiber dominated structural behaviour at higher reinforcement levels. Barcol hardness followed a similar increasing trend, approximately doubling relative to neat UPE, reaching values between 44-52 Barcol hardness with the increase in fiber loading. The presence of rigid, incompressible glass fibers near the composite surface restricts indentation, producing a harder and more resistant material. In contrast, flexural strain decreased sharply with reinforcement, dropping from 6.8% for neat UPE to 0.88-3.0% for the composites. This reduction indicates a loss of ductility due to constrained polymer mobility and earlier onset of micro-cracking as fiber-fiber interactions increase. The pronounced strain reduction reflects the typical trade-off of short-fiber-reinforced thermoset composites: enhanced stiffness and hardness occur at the expense of flexibility.

Overall, the combined results demonstrate that micro-glass fiber addition significantly improves the stiffness, surface resistance, and bending strength of UPE, while simultaneously reducing its ability to deform under flexural loading due to a more rigid and brittle composite microstructure.

CONCLUSIONS

1. Micro-glass fiber reinforcement significantly improved the flexural performance of UPE**,** yielding moderate increases in flexural strength and substantial enhancements in flexural modulus, particularly at reinforcement levels above 30 wt.% where fiber-dominated behaviour becomes prominent.
2. Surface hardness increased markedly with fiber addition**,** approximately doubling relative to neat UPE, due to the rigid and incompressible nature of the micro-glass fibers that restrict surface indentation.

3. Flexural strain decreased sharply as fiber content increased**,** indicating reduced ductility and higher brittleness resulting from restricted matrix mobility and intensified fiber–fiber interactions.
4. A clear stiffness-ductility trade-off was observed**:** improvements in modulus, hardness, and overall rigidity were accompanied by a notable loss in deformability.
5. Micro-glass fibers proved highly effective in reinforcing unsaturated polyester**,** enhancing its structural integrity for load-bearing applications where high stiffness and surface resistance are prioritized over flexibility.

REFERENCES

Alshahrani H., et al. Study on Flexural Behaviour of Glass Fiber Reinforced Composites, *Polymers.* ., (2022).

Assunçao G.S.C., (2024). Mechanical properties of glass-fiber reinforced polyester manufactured by different techniques, Rev. Mat.

Biswas B. Unsaturated Polyester Resins (book chapter). Elsevier / (overview of UPR properties and applications).

Boukhoulda A., Bendine K., Boukhoulda F.B., Bellali MA., Effects of fibre weight fraction on mechanical properties, bio-Composite reinforced with Alfa fibers: Experimental and numerical investigation, *Journal of Composite Materials*, vol. 58, issue 1, pp. 133-142. (2024)

Ganan P., et al., The Evolution and Future Trends of Unsaturated Polyester (UPR) Bio-composites, Polymers, 2023 - bibliometric/review analysis.

Jariwala H., Jain P., Maisuriya V., Experimental and statistical analysis of strength of glass-fiber-reinforced composites, *Polymer Composites*, 42(3):1407-1419, 2020.

Milosan I., Bedo T., Gabor C., Pop M.A., Mechanical Characteristics of Glass-Fiber-Reinforced Polyester Composite Materials, *Materials*, 2025.

Nallaiya, G., "The Effect of Fiber Length on Mechanical Properties of Unsaturated Polyester Composites Reinforced by the Fibers of Sisal", *International Journal of Scientific Research in Science, Engineering and Technology (IJSRSET*), Online ISSN : 2394-4099, Print ISSN : 2395-1990, Volume 9 Issue 3, pp. 14-20, May-June 2022.

Romanzini D., Influence of fiber content on the mechanical and dynamic properties, Composites (classical study on fiber fraction effects), 2013.

Tarikul H., Joao R. Correia M.G., Francisco S., Susana C.F., Marco J., Jose S.C., Freeze-thaw durability of vacuum infused glass fibre composites with unsaturated polyester and vinyl ester matrices. *Composites*, *Construction and Building Materials, Volume 455, 13 December 2024.*

Theoretical Calculation and Stepwise Optimization Analysis of the Equivalent Circuit Parameters of a Microwave Sensor

İbrahim GENÇ[1]

Mesud KAHRİMAN[2]

1- Süleyman Demirel Üniversitesi, Mühendislik ve Doğa Bilimleri Fakültesi, Elektronik ve Haberleşme Mühendisliği Bölümü. d2240112901@ogr.sdu.edu.tr ORCID No: 000-0002-1963-6685

2- Süleyman Demirel Üniversitesi, Mühendislik ve Doğa Bilimleri Fakültesi, Elektrik-Elektronik Mühendisliği Bölümü, mesudkahriman@sdu.edu.tr ORCID No: 0000-0003-0731-0936

ABSTRACT

This study presents the equivalent circuit modeling and progressive optimization of a four-port directional coupler and Complementary Split-Ring Resonator (CSRR) based microwave sensor, designed for the complex dielectric characterization of solid materials. The primary objective is to develop a fast, reliable, and physically meaningful analytical model to replace computationally expensive 3D electromagnetic simulations. Given the complex coupling effects and fringing fields, a controlled optimization strategy was executed within the Advanced Design System (ADS) environment. To avoid entrapment in local minima and preserve the physical validity of the circuit components, parameter tolerance boundaries were incrementally expanded up to a maximum of ±40%. Expanding beyond this limit was intentionally avoided to prevent non-physical parameter values and pure curve-fitting scenarios. The optimized model exhibited strong convergence, reducing the overall Mean Absolute Error (MAE) to 2.90 dB. The primary transmission characteristic (S_{21}) reached an MAE of 0.56 dB, which is well below the targeted 1.0 dB limit. This level of agreement accurately characterizes the resonance depth at 2.88 GHz, Q-factor, and bandwidth. Multi-port dynamics necessitated a natural trade-off and led to parallel amplitude offsets in the coupling (S_{31}) and isolation (S_{41}) ports. However, the model maintained high-fidelity spectral trend tracking. In conclusion, the successful convergence of the parameters within physically meaningful limits confirms the electrical stability and accuracy of the equivalent circuit topology. This approach offers a highly efficient and robust alternative for the design and analysis of complex metamaterial-based microwave sensors.

Keywords – Microwave Sensor, Equivalent Circuit Model, Directional Coupler, Complementary Split-Ring Resonator (CSRR), Optimization, S-parameter.

INTRODUCTION

Presently, the analysis and optimization processes of microwave circuit designs are predominantly conducted using full-wave electromagnetic simulators that employ algorithms such as the Finite Element Method (FEM) or the Finite Difference Time Domain (FDTD) (Swanson and Hoefer, 2003:55). The design of these circuits, operating within the high-frequency electromagnetic spectrum, requires a highly precise characterization of the interaction between complex physical geometries and electromagnetic wave propagation. Although full-wave simulation tools provide high numerical accuracy, they often exhibit a "black-box" nature in explicating the underlying electrical physics of the phenomena within the structure, while also incurring substantial computational costs

To circumvent these limitations and establish a conceptual framework for electromagnetic behavior, the Lumped Element Equivalent Circuit model is widely employed. This model reduces the physical behavior of circuit components to fundamental inductive (L), capacitive (C), and resistive (R) elements, serving as both a critical analytical tool and a robust design philosophy in microwave engineering (Bahl, 2003:9). The analytical advantages and physical insights provided by equivalent circuit modeling play a highly pronounced and indispensable role, particularly in the design of planar resonator-based microwave sensors. In modern scientific and industrial applications, the success of non-contact, high-sensitivity sensors utilized in fields such as dielectric material characterization, food safety, biomedical diagnostics, and environmental monitoring relies directly on the precision of these circuit models (Lei Zhu & Wu, 1999:1590; Wu & Li, 2005:7). Furthermore, the equivalent circuit modeling approach is not exclusively confined to microwave sensor designs; it is also extensively utilized across diverse platforms dedicated to electromagnetic wave manipulation. In this context, within metasurface architectures—which represent an advanced iteration of resonator-based microwave circuits—lumped-element models play a pivotal role in predicting the reflection and transmission characteristics of unit cells (Cildir, 2025:8; Cildir et al., 2025:12).

Equivalent circuit models provide distinct advantages over traditional simulation-based approaches in sensor applications. By mapping specific regions of the resonator topology to corresponding circuit elements, this method offers profound physical insight and enables robust parametric correlation. Specifically, the current density along the conductive traces exhibits an inductive character, whereas the electric field localization within the dielectric gaps corresponds to a capacitive response. This analytical framework allows the designer to deterministically comprehend how geometric modifications influence the spectral frequency response (Marcelli, 2024:2). Furthermore, while the full-wave electromagnetic simulation of complex 3D geometries typically requires hours of computation time, the equivalent circuit model can be solved in milliseconds within the Advanced Design System (ADS) environment. This remarkable computational efficiency facilitates the rapid execution of multi-parameter optimization processes and statistical tolerance analyses (Bandler et al., 2004:337). In addition to sensor research conducted within the RF/microwave frequency spectrum, the ADS platform is extensively utilized across a multitude of diverse multidisciplinary applications (Gozel et al., 2018:7; Kasar et al., 2019:5), primarily due to its superior computational speed and advanced circuit-based analysis capabilities. Ultimately, the equivalent circuit model allows the perturbation of the system's resonance characteristics—induced by the placement of a sample with dielectric or magnetic properties on the sensor—to be formulated directly through variations in the circuit elements (ΔC or ΔL). This capability establishes a solid mathematical foundation,

rendering the analytical computation of sensor sensitivity metrics highly feasible (Agarwal & Garg, 2024:8).

A review of the existing literature on equivalent circuit modeling (Mekki et al., 2024:42; Shi et al., 2025:8) indicates that full-wave simulation results and circuit model responses are predominantly aligned with high congruence through the direct application of optimization tools. These studies typically present the optimized parameters solely as final outcomes, lacking a step-by-step demonstration of how parameter deviations from their initially analytically derived values impact broadband performance. Consequently, there is a scarcity of comprehensive analyses in the literature elucidating the relationship between the systematic, progressive variation of equivalent circuit parameters and the resulting sensitivity and accuracy of S-parameter responses.

The primary objective of this study is to analyze, via a progressive optimization methodology, the broadband characteristics of an equivalent circuit topology. This topology is developed based on a novel four-port directional coupler-based sensor architecture loaded with a Complementary Split-Ring Resonator (CSRR) (Genç et al., 2026:5), whose performance in the 1–5 GHz band has been previously validated through both full-wave simulations and physical measurements. The proposed equivalent circuit model aims to replicate the S-parameters with high fidelity across the 1–5 GHz broadband spectrum. Accordingly, the initial values, analytically derived from the sensor's primary resonance frequency at 2.88 GHz, were designated as the central (nominal) parameters for the optimization algorithm. To ensure the convergence of the equivalent circuit model to the reference electromagnetic response and to circumvent entrapment in local minima, a controlled and progressive optimization strategy was executed within the ADS (Advanced Design System) environment. During this process, the parameter tolerance boundaries were incrementally expanded in a manner that preserves the physical meaning of the equivalent circuit elements, seeking the optimum electrical balance of the system. Within the scope of this approach, the circuit parameters were not merely curve-fitted to a final outcome through a single-step optimization; conversely, the evolution of the *S*-parameter responses and the modeling errors yielded by the controlled variations at each iterative stage were meticulously analyzed. The implemented methodology goes beyond merely identifying the optimal parameter set; it physically and numerically elucidates the impact of parameter deviations on broadband performance, thereby establishing a robust, data-driven bridge between theoretical calculations and broadband physical reality.

REFERENCE SENSOR ARCHITECTURE AND THE DEVELOPMENT OF THE EQUIVALENT CIRCUIT TOPOLOGY

This section presents the geometric configuration, physical dimensions, and full-wave simulation responses of the four-port sensor, which serves as the baseline for the progressive optimization analysis and whose performance has been previously validated in the literature. Subsequently, it details the methodology by which the equivalent circuit topology—formulated to electrically represent the aforementioned physical structure—is mapped onto the sensor architecture. Finally, the analytical derivations of the circuit element values are executed, predicated on the sensor's primary resonance frequency of 2.88 GHz.

Geometric Configuration and Full-Wave Simulation Results

In the design of the microwave sensor presented in the literature, an FR4 substrate with a relative permittivity (ε_r) of 4.3 was utilized. The design procedure of the sensor fundamentally comprises two primary phases. In the initial phase, a directional coupler—depicted in Figure 1(a)—was designed to exhibit a characteristic impedance (Z_0) of 50 Ω and to provide a -10 dB coupling level at a center frequency of 2 GHz. In the subsequent phase, Complementary Split-Ring Resonator (CSRR) elements, the geometric details of which are provided in Figure 1(b), were integrated into the ground plane of the directional coupler. These elements were optimized to generate the targeted resonance at 2.88 GHz, thereby yielding the final microwave sensor architecture (Genç et al., 2026:5).

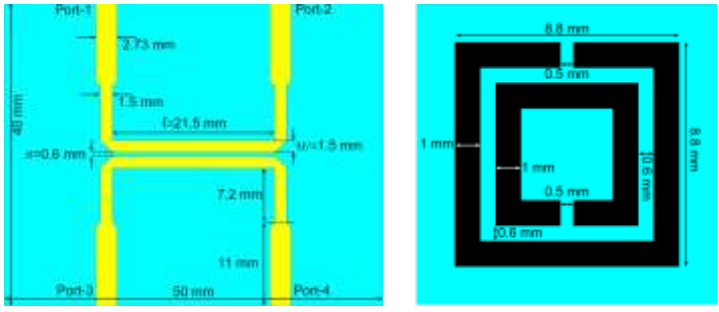

(a) (b)

Figure 1. Geometric configuration and physical dimensions of the components utilized in the design of the directional coupler-based, CSRR-loaded microwave sensor: (a) Directional coupler, and (b) CSRR structures. (Genç et al., 2026:3)

In the final sensor architecture, realized by integrating the CSRR structures into the ground plane of the directional coupler, the layout of these resonance-determining elements is depicted in Figure 2(a). Furthermore, the broadband S-parameter responses across the 1–5 GHz spectrum, obtained

from the full-wave electromagnetic simulations of the sensor, are presented in Figure 2(b). These simulation and measurement results corroborate that the transmission parameters S_{21}, S_{31} and S_{41} designated for material characterization exhibit highly congruent resonance characteristics in the vicinity of the targeted 2.88 GHz frequency (Genç et al., 2026:5).

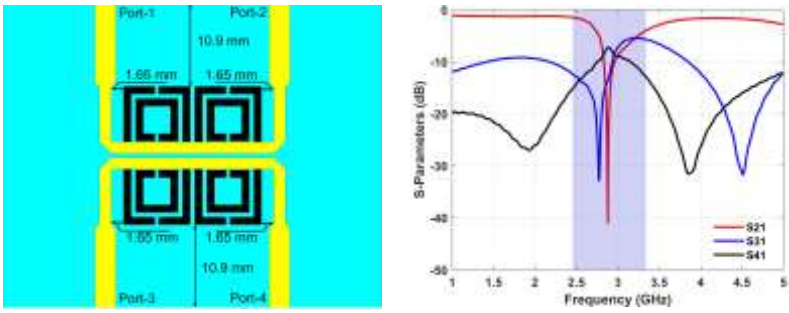

(a) (b)

Figure 2. (a) Layout of the CSRR elements on the ground plane of the four-port sensor, and (b) broadband S-parameter responses obtained via full-wave simulations and physical measurements (Genç et al., 2026:5).

Development of the Equivalent Circuit Topology

According to the classical transmission line theory established by Pozar (2012:147), a lossless microstrip line with a physical length of l can be abstracted from its distributed nature and modeled as a lumped reactive element, provided that its electrical length remains sufficiently small ($\beta l \ll 1$). Under this boundary condition, the electromagnetic behavior of the transmission line can be approximately represented by an equivalent reactance, and the input impedance of a short-circuited line is formulated as follows (Pozar, 2012:147):

$$Z_{in} \approx jZ_0\beta l \tag{1}$$

However, as the operating frequency increases, the phase constant (β) of the transmission line correspondingly rises, which subsequently leads to an increase in its electrical length (βl). The fundamental relationship between the phase constant and the phase velocity (v_p) of the propagation medium is expressed as follows:

$$\beta = \frac{2\pi f}{v_p} \tag{2}$$

In a microstrip configuration, the phase velocity is directly correlated with the speed of light in a vacuum (c) and the effective dielectric constant (ε_{reff}) of the substrate, and it is approximately defined as follows:

$$v_p = \frac{c}{\sqrt{\varepsilon_{reff}}} \tag{3}$$

As the operating frequency escalates and the electrical length βl exceeds the critical threshold, representing the distributed impedance and complex phase behavior of the transmission line with a solitary LC cell loses its accuracy. To circumvent this modeling limitation encountered in broadband analyses and to faithfully reconstruct the high-frequency response of the system, a segmentation methodology was implemented during the formulation of the equivalent circuit topology. Within this framework, to accurately emulate the distributed line behavior, transmission lines with a total physical length of l_{total} are partitioned into N cascaded LC cells, thereby employing a ladder-type network topology. During this segmentation procedure, the electrical length of each sub-segment was minimized to satisfy the following boundary condition:

$$\beta l_{segment} = \beta \frac{l_{total}}{N} \ll 1 \tag{4}$$

This analytical condition demonstrates that by increasing the number of segments, the electrical length of each individual section is curtailed, thereby minimizing phase errors at high frequencies and enhancing the overall model accuracy. Given the requirement to analyze the investigated sensor structure across a broad spectrum of 1–5 GHz, the conventional single-section equivalent circuit approach was discarded in favor of this progressive circuit model, which also accounts for structural discontinuities. In accordance with this theoretical framework, the thin and thick microstrip line regions within the sensor geometry were modeled independently. Furthermore, the primary coupling region at the center of the sensor was partitioned into three identical π-cells to accurately characterize not only the transmission line parameters but also the broadband electromagnetic coupling effects between the lines and the ground plane.

In the modeling of the resonator structure positioned at the center of this coupling region, the fundamental equivalent circuit topology (Figure 3) proposed in the literature by Baena et al. (2005:1452) to describe the characteristic electromagnetic behavior of CSRR structures was adopted as a reference. This model characterizes the inductive and capacitive effects inherently possessed by the resonator and those induced on the transmission line through a lumped-element approximation (Baena et al., 2005:1452).

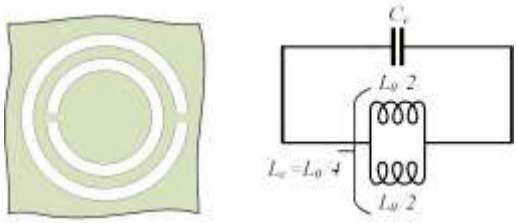

Figure 3. Fundamental equivalent circuit topology proposed by Baena et al. (2005:1452) for modeling the characteristic electromagnetic behavior of CSRR structures.

The aforementioned classical CSRR equivalent circuit (Figure 3) was integrated into the central unit of the three identical π -cells constituting the primary coupling region of the sensor, in alignment with broadband analysis requirements and physical layout constraints. Within this central π -cell, the physical interactions between the resonator rings and the transmission lines were incorporated into the network as capacitive and inductive coupling elements. The final equivalent circuit topology of the sensor yielded by the segmentation of the transmission lines and the coupling-based integration of Baena's resonator model into the central π cell is illustrated in Figure 4.

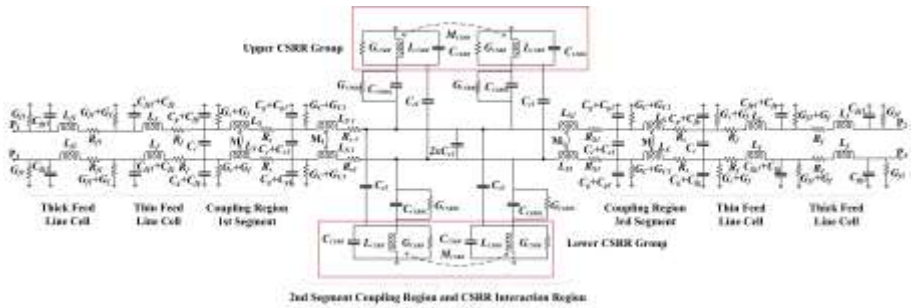

Figure 4. Proposed lumped-element equivalent circuit topology for the microwave sensor architecture.

Analytical Derivation of the Equivalent Circuit Parameters

Each lumped element within the proposed segmentation-based equivalent circuit model (Figure 4) was analytically derived by referencing the physical design parameters of the sensor and the dielectric properties of the substrate. In the initial stage of the modeling process, the effective dielectric constant (ε_{reff}), which characterizes the wave propagation on the microstrip lines, and the electrical length (θ), which determines the phase shift, were calculated using the formulations established by Pozar (2012:148):

$$\varepsilon'_{reff} = \frac{\varepsilon'_r + 1}{2} + \frac{\varepsilon'_r - 1}{2} \frac{1}{\sqrt{1 + 12h/w}} \quad (5)$$

$$\lambda_g = \frac{c}{f_0 \sqrt{\varepsilon_{eff}}} \quad (6)$$

$$\theta = \frac{l}{\lambda_g} x\, 360^o \quad (7)$$

Furthermore, to enhance the physical fidelity of the circuit, parallel conductance representing the dielectric losses of the FR-4 substrate and series resistance parameters modeling the ohmic losses stemming from the skin effect at high frequencies were incorporated into the analysis, utilizing the formulations provided by Pozar (2012:119) (Pozar, 2012:119)

$$G = \omega_0 C tan\delta \quad (8)$$

$$R_{surf} = \sqrt{\frac{\omega_0 \mu_0}{2\sigma}} \quad (9)$$

$$R = R_{surf} \left(\frac{1}{w}\right) \quad (10)$$

The electrical parameters of the three identical segments, which represent the coupling region of the directional coupler located at the center of the sensor, were determined based on even- and odd-mode analysis (Eroglu and Lee, 2008:2757). The even-mode (Z_{0e}) and odd-mode (Z_{0o}) impedances are defined in terms of the coupling coefficient (C) as follows:

$$Z_{0e} = Z_0 \sqrt{\frac{1 + 10^{C/20}}{1 - 10^{C/20}}} \quad (11)$$

$$Z_{0o} = Z_0 \sqrt{\frac{1 - 10^{C/20}}{1 + 10^{C/20}}} \quad (12)$$

Using these mode impedances, the series self-inductance (Ls), ground capacitance (Cg), mutual magnetic coupling (M), and electric coupling (Cc) between the lines of the respective segments were calculated analytically as a function of θ (Zhou and Chen, 2008:2):

$$C_g = \frac{1}{2\pi f_0 Z_{0e}} \tan\left(\frac{\theta}{2}\right) \tag{13}$$

$$C_c = \frac{1}{4\pi f_0} \left(\frac{1}{Z_{0o}} - \frac{1}{Z_{0e}}\right) \tan\left(\frac{\theta}{2}\right) \tag{14}$$

$$L_s = \frac{Z_{0e} + Z_{0o}}{4\pi f_0} sin\ (\theta) \tag{15}$$

$$M = \frac{Z_{0e} - Z_{0o}}{4\pi f_0} sin\ (\theta) \tag{16}$$

The CSRR structure etched on the ground plane is modeled as a parallel *LC* tank circuit excited by an axial electric field. The equivalent capacitance (C_c) of the structure was calculated using a structure-specific integral equation that incorporates the dielectric substrate thickness (h), the permittivity of free space (ε_0), and the relative permittivity of the substrate (ε_r). In this formulation, geometric variables such as the inner metal disk radius of the resonator (a), the outer ground plane aperture radius (b), and the slit width between the rings (c) are integrated over the wavenumber (k) in the spectral domain, thereby maximizing the physical fidelity of the model (Baena et al., 2005:1454).

$$C_c = \frac{\pi^3 \varepsilon_0}{c^2} \int_0^{+\infty} \frac{[b\mathcal{B}(kh) - a\mathcal{B}(ka)]^2}{k^2} \left[\frac{1}{2}\left(1 + \frac{1 + \frac{\varepsilon_r}{\varepsilon_0}\tanh(kh)}{1 + \frac{\varepsilon_0}{\varepsilon_r}\tanh(kh)}\right)\right] dk \tag{17}$$

In Equation (17), the $\mathcal{B}$ function represents a combination of the Struve and Bessel functions. The equivalent inductance (L_c) is defined as one-fourth of the total ring inductance (L_o), based on the assumption that the structure behaves as a circular coplanar waveguide (CPW) (Baena et al., 2005:1454):

$$L_0 = 2\pi\, r_0\, L_{pull} \tag{18}$$

$$L_c = \frac{L_0}{4} = \frac{2\pi\, r_0\, L_{pull}}{4} \tag{19}$$

Here, the value of L_{pul} is obtained through elliptic integrals depending on the magnetic permeability of free space (μ_0) and geometric ratios:

$$L_{pull} = \frac{\mu_0}{4} \frac{K(k')}{K(k)} \tag{20}$$

Here, the modulus k represents the geometric ratio defined by the metal ring width (d) and the slit width (c) constituting the CSRR, whereas k' is the complementary modulus and can be calculated using the following equations:

$$k = \frac{d}{d + 2c} \tag{21}$$

$$k' = \sqrt{1 - k^2} \tag{22}$$

The mutual inductance between two CSRRs (M_{CSRR}), which characterizes the magnetic interaction between two adjacent CSRR unit cells, can be expressed in terms of the resonators' self-inductances (L_{CSRR}) and the mutual coupling coefficient (k_{mut}) as follows:

$$M_{CSRR} = k_{mut} L_{CSRR} \tag{23}$$

The weak electric fields coupling from the CSRR structure on the ground plane to the far transmission line on the top surface are modeled as microstrip fringing capacitance. This value can be expressed by the following approximation as a function of the gap between the two lines (s) and the dielectric thickness (h):

$$C_{cl} = \frac{\varepsilon_0 \varepsilon_{reff} W_{eff}}{h} \exp(-\frac{\pi s}{h}) \tag{24}$$

The interaction of the CSRR resonator with the overlying coupling line is modeled as the lumped equivalent (C_{CSRRL}) of the distributed capacitance in the corresponding section of the transmission line. Accordingly, the shunt capacitance value was derived using the per-unit-length capacitance expressions from Pozar (2012:142), and scaled by the speed of light (c) and the physical length occupied by the resonator under the line ($l_{segment}$) as follows:

$$C_{CSRRL} = \frac{\sqrt{\varepsilon_{reff}}}{Z_0 c} l_{segment} \tag{25}$$

Once the mathematical foundation of the proposed equivalent circuit model was established, all parameters required to model the circuit's behavior at the fundamental resonance frequency of 2.88 GHz were derived using Equations (5)–(25). This derivation took into account the physical design parameters of the sensor, including an FR-4 substrate with a thickness of h = 1.5 mm and a relative permittivity of ε_r = 4.3, a line length of l= 21.5 mm, a

gap between the lines of s = 0.6 mm, and a square CSRR geometry with dimensions of 8.8 x 8.8 mm. These derived theoretical values establish a robust baseline for the precise optimization process to be conducted in the Advanced Design System (ADS) environment. The analytical starting values for all transmission lines, the resonator tank, and the parasitic coupling components that constitute the equivalent circuit are presented in Table 1.

Table 1. Calculated Initial Values of Equivalent Circuit Elements for the 2.88 GHz Resonance Frequency

Circuit Section	***Symbol***	***Represented Physical/Electrical Component***	***Initial Value***
Thick Feed Lines θ= 48.25 ° Z_0 = 52.26 Ω ε_{reff} = 3.35	L_{f1}	Total Series Inductance of Thick Line	3.07 nH
	C_{fg1}	Total Shunt Capacitance of Thick Line	0.67 pF
	R_{f1}	Total Series Ohmic Resistance of Thick Line	0.047 Ω
	G_{f1}	Total Dielectric Loss Conductance of Thick Line	0.111 mS
Thin Feed Lines W = 1.5 mm θ= 30.5 ° Z_0 = 71.82 Ω ε_{reff} = 3.108	L_f	Total Series Inductance of Thin Line	2.89 nH
	C_{fg}	Total Shunt Capacitance of Thin Line	0.30 pF
	R_f	Total Series Ohmic Resistance of Thin Line	0.056 Ω
	G_f	Total Dielectric Loss Conductance of Thin Line	0.066 mS
Directional Coupler Segments s = 0.6 mm, $l_{segment}$ = 7.17mm θ= 43.67 ° Z_{0e} = 82 Ω Z_{0o} = 32 Ω	L_s	Series Self-Inductance of Coupling Segment	2.17 nH
	L_{s1}	Series Self-Inductance of Center Segment	1.34 nH
	C_g	Ground Capacitance of Coupling Segment	0.46 pF
	C_{g1}	Ground Capacitance of Center Segment	0.25pF
	M	Mutual Magnetic Coupling Between Lines	0.95 nH
	M_1	Mutual Magnetic Coupling of Center Lines	0.33 nH
	C_c	Electric Coupling Between Lines	0.73 pF
	C_{c1}	Electric Coupling of Center Lines	0.054 pF
	R_s	Series Ohmic Resistance of Segment	0.067 mΩ
	R_{s1}	Series Ohmic Resistance of Center Segment	0.037 mΩ
	G_c	Dielectric Loss Conductance of Segment	0.160 mS
	G_{c1}	Dielectric Loss Conductance of Center Segment	0.091 mS
Square CSRR Resonator Tank and Secondary Couplings 8.8 x 8.8 mm, @ 2.88 GHz	L_{CSRR}	Equivalent Inductance of Square CSRR	1.50 nH
	C_{CSRR}	Equivalent Capacitance of Square CSRR	2.04 pF
	G_{CSRR}	Dielectric Leakage Conductance of Square CSRR	0.74 mS
	C_{CSRRL}	Shunt Capacitance of CSRR-to-Line Connection	0.84 pF
	G_{CSRRL}	Dielectric Loss Conductance of CSRR-to-Line Connection	0.30 mS
	M_{CSRR}	Mutual Inductance Between CSRRs	0.20 nH
	C_{c1}	Fringing Capacitance to the Far Line	0.35 pF

STEPWISE OPTIMIZATION ANALYSIS AND RESULTS

This section details the stepwise process of applying the derived analytical initial values to the equivalent circuit model within the ADS environment, and the subsequent tuning process aimed at aligning these values with the full-wave simulation results obtained from CST Microwave Studio.

Error Analysis Between Analytical Initial Values and CST Simulation Data

Using the equivalent circuit element values analytically derived in Section 2 and presented in Table 1, a simulation was performed in the ADS environment without the application of any optimization technique. A comparative plot of the resulting spectral *S*-parameter responses and the CST Microwave Studio full-wave simulation results is illustrated in Figure 5.

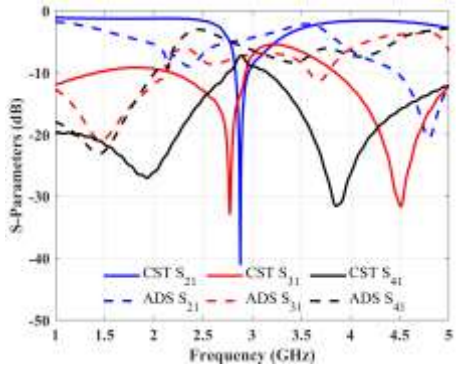

Figure 5. Comparison of the ADS simulation results, obtained using the analytically calculated values (Table 1), with the reference CST full-wave simulation data.

An analysis of Figure 5 reveals significant amplitude and frequency discrepancies between the ADS equivalent circuit results, derived from analytical calculations, and the reference CST data. Although the initial responses lack direct agreement, the analytical model demonstrates a clear tendency to capture the overall spectral behavior and resonance trends. These pronounced initial deviations underscore the necessity of a stepwise optimization process to drive the convergence of the equivalent circuit model toward the reference full-wave data (CST).

To project the deviations observed in the graphical results onto a numerical domain and to quantitatively assess the accuracy performance of the analytically derived equivalent circuit parameters across the 1–5 GHz broadband spectrum, a Mean Absolute Error (MAE) analysis was performed on the scattering parameters S_{21}, S_{31}, and S_{41}. The MAE metric, which is based on the arithmetic mean of the absolute differences between the ADS responses and the reference 3D full-wave electromagnetic data, enables a direct evaluation of the error magnitude caused by parameter variations in the decibel (dB) scale. This distinctive characteristic renders the MAE a highly practical and reliable quantitative assessment tool in microwave model validation processes, where full-wave electromagnetic simulations are compared with parametric equivalent circuit models.

A review of the fundamental literature on microwave filter and directional coupler designs reveals that typically accepted design tolerances

regarding passband ripples are generally specified on the order of 0.5 dB (Matthaei et al., 1980; Pozar, 2012). Guided by this theoretical foundation, a highly rigorous error classification methodology with strict boundaries was adopted in the present study to validate the accuracy of both the analytically calculated initial parameters and the subsequent stepwise optimization stages. According to this established framework, an MAE ≤ 0.5 dB is defined as "high agreement" (corresponding to a maximum variation of 12% in power level), the 0.5 dB < MAE ≤ 1.0 dB range as "partial agreement" (power variation between 12% and 26%), and an MAE > 1.0 dB as "insufficient agreement." The insufficient agreement category not only implies that the selected parameter values induce a power deviation exceeding 26%, but also indicates a dramatic degradation in the characteristic behavior of the S-parameter frequency response.

In addition to the MAE values, which reflect the overall average performance of the system across the frequency spectrum of interest, a "maximum deviation" metric has also been integrated into the analysis. As a reflection of the variations in the target parameters, this metric represents the maximum absolute difference (in dB) recorded across the operating band between the ADS predictions and the CST full-wave simulation results. The primary motivation for incorporating this metric into the analysis is to transparently reveal the peak deviation levels exhibited by the parameter optimization particularly in challenging regions such as sharp resonance points or band edges and to verify the stability of the equivalent circuit under these boundary conditions.

Taking the defined evaluation criteria into account, the broadband error analyses and the identified maximum deviation values for the circuit simulations established through analytical calculations are presented in Table 2.

Table 2. Error analyses and maximum deviation values of the circuit simulations established through analytical calculations.

Parameter	**MAE (dB)**	**Max. Deviation (dB)**	**Frequency (GHz)**	**Compliance Status**
S_{21}	4.96	36.21	2.880	Non-compliant
S_{31}	7.25	27.81	4.512	Non-compliant
S_{41}	9.48	25.18	3.852	Non-compliant
General MAE	7.23	-	-	Non-compliant

An examination of Table 2 reveals that the analytically calculated initial parameters exceed the specified tolerance limits for all scattering parameters and are categorized as 'non-compliant' according to the MAE > 1.0 dB criterion. The MAE value of 4.96 dB obtained for the S_{21} parameter, which represents the fundamental transmission behavior, indicates that the model

fails to capture the resonant characteristics across the broadband spectrum. This non-compliance escalates to levels of 7.25 dB and 9.48 dB for the S_{31} and S_{41} ports, respectively, where complex electromagnetic interactions are dominant.

The primary reason for the high deviations exhibited by the analytical model is the inability of quasi-static assumptions to fully represent the fringing capacitances occurring at the corner points and line ends of the square CSRR and directional coupler segments. In particular, the extreme maximum deviation of 36.21 dB observed at the 2.88 GHz resonance frequency of the S21 parameter proves the inadequacy of the analytical model in characterizing the high-Q notch depth and the dispersive nature of the structure. Furthermore, the analytical approach neglects parasitic cross-coupling effects between distant segments within the layout and fails to account for the frequency-dependent variations of conductor and dielectric losses (e.g., skin effect). The inherent inability of fixed-value lumped elements (L, C, R, G) to reflect the frequency-varying electrical length effects of microwave structures leads to a rapid degradation of model accuracy as the frequency increases.

In conclusion, these initial parameters obtained through the analytical approach prove insufficient to fully represent the broadband performance of the sensor and the complex electromagnetic interactions between the ports. This situation underscores the necessity of transitioning beyond the narrow-band assumptions of analytical models to reach 'optimum' values that achieve high agreement with full-wave simulation results. Consequently, subjecting these analytically derived data to a 'fine-tuning' process via optimization techniques is considered a critical step toward enhancing the physical accuracy of the model.

Progressive Optimization Strategy

In accordance with the established physical constraints and the unavoidable need for optimization, a progressive parametric scanning strategy was adopted for the equivalent circuit model to ensure the convergence of the initial parameters to the full-wave reference data obtained in the CST environment. Within this framework, a systematic scanning process was initiated with ±10% variation steps, using the analytically calculated reference values as the center points. To enable the model to capture complex electromagnetic interactions and reach the optimum electrical balance without being trapped in local minima, the scanning range was incrementally expanded in a manner that preserves the physical meaning of the equivalent circuit elements; the spectral impact of each component variation on the S-parameters was analyzed in detail.

Considering the complex electromagnetic behaviors, strong coupling effects, and fringing fields of the four-port directional coupler and CSRR-based structure which cannot be directly calculated in the analytical model stretching the optimization tolerances to the extent permitted by physical

boundaries was evaluated as a necessary and appropriate methodological approach to represent the model as closely as possible to physical reality.

Following this methodological planning, the built-in optimization tool of the ADS software was activated as the first step of the progressive process. A constrained optimization procedure was performed, using the analytical initial values presented in Table 1 as a reference and allowing the parameters to vary only within a ±10% tolerance range. The comparative plots of the equivalent circuit S-parameters obtained from this initial optimization step versus the CST full-wave simulation results are presented in Figure 6.

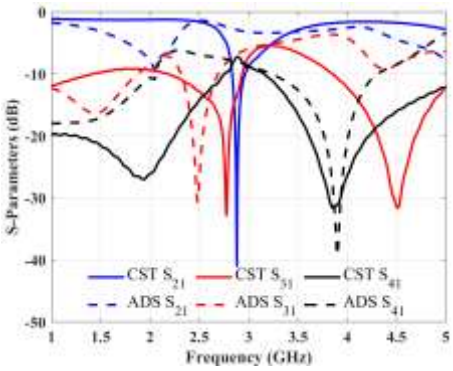

Figure 6. Comparison of the ADS optimization results within a ±10% variation range of the initial values (Table 1) versus the reference CST data.

The ±10% constrained optimization results presented in Figure 6 demonstrate significant progress, both statistically and visually, in the convergence of the equivalent circuit model to the CST reference data when compared to the analytical initial state in Figure 5. This recovery in the overall spectral behavior, achieved despite the narrow ±10% variation range allowed to the algorithm, is mathematically validated by the reduction of the calculated Overall MAE value from 7.23 dB to 5.01 dB. Although the model has begun to capture the fundamental spectral characteristics of the reference data, full spectral agreement has not yet been achieved due to the constraints imposed by the 10% tolerance limit.

A detailed port-based analysis reveals that the deep resonance of CST at 2.88 GHz in the primary transmission parameter, S_{21}, cannot be captured; instead, the model generates a relatively shallow notch at approximately -10 dB levels around 2 GHz. Furthermore, the S_{31} parameter fails to reach the deep resonance characteristic of the reference data near 2.8 GHz, shifting towards the 2.5 GHz region due to optimization constraints. In contrast, the most notable local agreement is achieved in the S_{41} parameter; the deep notch near 3.9 GHz in the high-frequency region of the spectrum shows an almost perfect overlap with the CST data despite the narrow tolerance applied. However, the peak expected around 2.8 GHz shifts toward 2.3 GHz. This situation

physically demonstrates that while the narrow optimization boundaries achieve high local agreement for S_{41}, they remain insufficient to simultaneously compensate for the high-Q resonance of the CSRR structure in S_{21} and the strong coupling responses in S_{31}.

The previously applied error analysis methodology was repeated for the *S*-parameters obtained from the ±10% constrained optimization step. Based on the established evaluation criteria, the results of the broadband error analysis and the identified maximum deviation values are presented in Table 3.

Table 3. Error (MAE) and Deviation Analysis After ±10% Constrained Optimization

Parameter	MAE (dB)	Max. Deviation (dB)	Frequency (GHz)	Compliance Status
S_{21}	2.67	38.07	2.880	Non-compliant
S_{31}	5.97	24.63	2.772	Non-compliant
S_{41}	6.40	15.97	2.104	Non-compliant
Genel MAE	5.01	-	-	Non-compliant

As a result of the ±10% constrained optimization step, the reduction of the overall MAE from 7.23 dB to 5.01 dB indicates that the model has begun to capture the fundamental electromagnetic trend over the broadband. However, the maximum deviation reaching 38.07 dB at the resonance frequency (2.88 GHz) for the S_{21} parameter physically proves that the narrow ±10% tolerance range is insufficient to simultaneously compensate for the complex cross-coupling effects and the high-Q resonance depth. To understand the mathematical basis of why the model is constrained on the frequency axis despite capturing the visual characteristics correctly, it is necessary to examine Table 4, which presents the parametric boundary constraints.

The parametric variation analysis presented in Table 4 shows that 20 out of 27 physical parameters constituting the equivalent circuit model were pushed by the algorithm exactly to the narrow ±10% tolerance limits or to values very close to these boundaries. This intensive 'boundary saturation' has physically constrained the convergence of the optimization process. Specifically, the fact that critical resonator elements determining the fundamental resonance characteristics (L_{CSRR}, C_{CSRR}) and cross-couplings between lines (C_g, C_{cl}, M, M_{CSRR}) remained trapped at the lower or upper constraints mathematically prevents further minimization of the error function (MAE). This situation proves that the actual optimal solution space (global optimum), capable of fully modeling the complex electromagnetic behavior of the circuit, lies well beyond this defined narrow tolerance range.

To release the optimization algorithm from these artificial constraints and provide a wider search space, thereby enabling the parameters stuck at boundary values to reach the correct local minima, the parametric scanning limits were expanded to the ±20% level in accordance with the progressive

optimization strategy established at the beginning of the study. The comparative spectral plots of the equivalent circuit S-parameters obtained as a result of this second optimization phase versus the CST full-wave reference results are presented in Figure 7.

The ±20% expanded optimization results presented in Figure 7 demonstrate a critical improvement in the convergence of the equivalent circuit model to the reference data. The fundamental S_{21} resonance notch, which remained shallow and stagnant in the low-frequency region (around 2.4 GHz) during the previous narrow-tolerance (±10%) phase, has performed a significant and successful shift toward the target center frequency of 2.88 GHz with the expansion of the search space. Although the improved representation of the S_{21} resonance depth (-45 dB) and center frequency in the spectrum validates the methodological accuracy of the progressive optimization strategy, the broadband spectral behaviors of the S_{31} and S_{41} parameters have not yet been accurately modeled.

Table 4. ±10% Constrained Optimization Results and Boundary Value Analysis.

Parameter	***Initial Value***	***±10% Optimization Result***	***Variation (Δ%)***	***Boundary Status***
L_{f1}	3.07 nH	2.763 nH	-10.00%	At Limit
C_{fg1}	0.67 pF	0.737 pF	+10.00%	At Limit
R_{f1}	0.047 Ω	0.0423 Ω	-10.00%	At Limit
G_{f1}	0.111 mS	0.0999 mS	-10.00%	At Limit
L_f	2.89 nH	3.179 nH	+10.00%	At Limit
C_{fg}	0.30 pF	0.330 pF	+10.00%	At Limit
R_f	0.056 Ω	0.0504 Ω	-10.00%	At Limit
G_f	0.066 mS	0.0594 mS	-10.00%	At Limit
L_s	2.17 nH	2.387 nH	+10.00%	At Limit
L_{s1}	1.34 nH	1.474 nH	+10.00%	At Limit
C_g	0.46 pF	0.414 pF	-10.00%	At Limit
C_{g1}	0.25 pF	0.225 pF	-10.00%	At Limit
M	0.95 nH	0.855 nH	-10.00%	At Limit
M_1	0.33 nH	0.3541 nH	+7.30%	Inside
Cc	0.73 pF	0.718 pF	-1.64%	Inside
C_{c1}	0.054 pF	0.0528 pF	-2.22%	Inside
Rs	0.067 mΩ	0.0737 mΩ	+10.00%	At Limit
R_{s1}	0.037 mΩ	0.0385 mΩ	+4.05%	Inside
Gc	0.160 mS	0.144 mS	-10.00%	At Limit
G_{c1}	0.091 mS	0.0819 mS	-10.00%	At Limit
L_{csrr}	1.50 nH	1.350 nH	-10.00%	At Limit
C_{csrr}	2.04 pF	2.0592 pF	+0.94%	Inside
G_{CSRR}	0.740 mS	0.7301 mS	-1.34%	Inside
C_{CSRRL}	0.84 pF	0.756 pF	-10.00%	At Limit
G_{CSRRL}	0.300 mS	0.270 mS	-10.00%	At Limit
M_{CSRR}	0.20 nH	0.1802 nH	-9.90%	At Limit
C_{cl}	0.35 pF	0.315 pF	-10.00%	At Limit

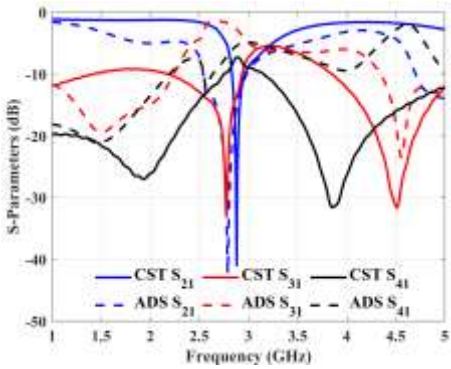

Figure 7. Comparison of the ADS optimization results within a ±20% variation range of the initial values (Table 1) versus the reference CST data.

To determine the numerical projection of the expanded scanning range on model sensitivity, the spectral data obtained from the ±20% optimization phase were re-analyzed according to statistical performance criteria, and the findings are detailed in Table 5

Table 5. Error (MAE) and Deviation Analysis After ±20% Constrained Optimization

Parameter	MAE (dB)	Max. Deviation (dB)	Frequency (GHz)	Compliance Status
S_{21}	4.01	36.65	2.788	Non-compliant
S_{31}	4.31	26.12	2.480	Non-compliant
S_{41}	8.26	22.66	3.848	Non-compliant
Global MAE	5.53	-	-	Non-compliant

As seen in the statistical data presented in Table 5, the search space expanded by ±20% increased the Overall Mean Absolute Error (MAE) from 5.01 dB to 5.53 dB, contrary to expectations. Although the notch depth of the S_{31} parameter in the visual spectrum (Figure 7) improved, the increase in the average error of this parameter to 4.01 dB and the maximum deviation of the S_{41} parameter reaching 22.66 dB physically demonstrate the severe 'trade-off' mechanism in the system.

While attempting to capture the resonance form in a local region, the algorithm was forced to degrade the overall agreement in other coupling parameters due to narrow boundaries. The high deviations (36.65 dB) observed at the resonance frequency are an analytical illusion arising from the nature of high-Q resonators. This resulting increase in error and parametric congestion demonstrate that the actual global optimum of the model lies well beyond the ±20% limits

The current equivalent circuit parameter values reached as a result of the optimization process conducted within the ±20% limits are detailed in

Table 6. An analysis of the ±20% data presented in Table 6 reveals that the majority of the circuit elements particularly the parameters determining the fundamental resonance and coupling characteristics of the sensor have hit the lower boundary limits, resulting in a serious contraction of the model's solution set. To increase the rate of improvement and enable the parameters to escape these restrictive local minima more effectively, the optimization process was continued by moving to the next step of the progressive strategy: the ±40% expanded scanning phase.

The equivalent circuit S-parameters obtained from the third optimization phase, conducted by expanding the parameter constraints to the ±40% level, are presented in Figure 8 in comparison with the CST full-wave reference data.

Table 6. ±20% Constrained Optimization Results and Boundary Value Analysis.

Parameter	*Initial Value*	*±10% Optimization Result*	*Variation (Δ%)*	*Boundary Status*
L_{f1}	3.07 nH	2.7358 nH	-10.89%	Inside
C_{fg1}	0.67 pF	0.8037 pF	+19.96%	At Limit
R_{f1}	0.047 Ω	0.0564 Ω	+20.00%	At Limit
G_{f1}	0.111 mS	0.1332 mS	+20.00%	At Limit
L_f	2.89 nH	3.4637 nH	+19.85%	At Limit
C_{fg}	0.30 pF	0.2611 pF	-12.97%	Inside
R_f	0.056 Ω	0.0671 Ω	+19.85%	At Limit
G_f	0.066 mS	0.0788 mS	+19.40%	At Limit
L_s	2.17 nH	1.8771 nH	-13.50%	Inside
L_{s1}	1.34 nH	1.4117 nH	+5.35%	Inside
C_g	0.46 pF	0.3880 pF	-15.65%	Inside
C_{g1}	0.25 pF	0.2182 pF	-12.71%	Inside
M	0.95 nH	1.0318 nH	+8.61%	Inside
M_1	0.33 nH	0.3953 nH	+19.80%	At Limit
Cc	0.73 pF	0.6847 pF	-6.20%	Inside
C_{c1}	0.054 pF	0.0593 pF	+9.80%	Inside
Rs	0.067 mΩ	0.0794 mΩ	+18.49%	Near Limit
R_{s1}	0.037 mΩ	0.0444 mΩ	+19.99%	At Limit
Gc	0.160 mS	0.19 mS	+18.70%	Near Limit
G_{cl}	0.091 mS	0.1088 mS	+19.60%	At Limit
L_{csrr}	1.50 nH	1.2002 nH	-19.99%	At Limit
C_{csrr}	2.04 pF	1.6324 pF	-19.98%	At Limit
G_{CSRR}	0.740 mS	0.7429 mS	+0.40%	Inside
C_{CSRRL}	0.84 pF	0.6727 pF	-19.91%	At Limit
G_{CSRRL}	0.300 mS	0.3555 mS	+18.50%	Near Limit
M_{CSRR}	0.20 nH	0.1600 nH	-19.99%	At Limit
C_{cl}	0.35 pF	0.28 pF	-20%	At Limit

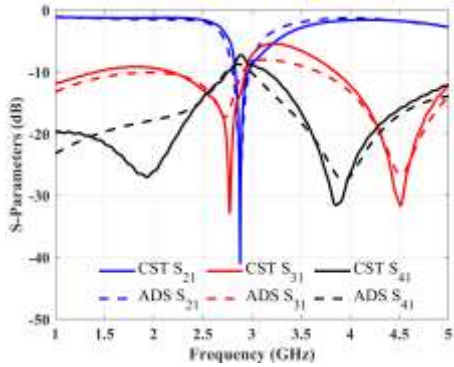

Figure 8. Comparison of the ADS optimization results within a ±40% variation range of the initial values (Table 1) versus the reference CST data.

The S-parameters obtained by expanding the model boundaries to the ±40% range (Figure 8) demonstrate a dramatic improvement in spectral trends compared to the previous ±20% optimization phase. According to the port-based visual and numerical trend analysis, the S_{21} parameter representing the primary transmission line which had shifted from the resonance center during the ±20% phase reached -25 dB levels over the -40 dB deep resonance notch of the reference CST data at 2.88 GHz. In the S_{31} port reflecting the coupling characteristic, the wide amplitude gap seen in the ±20% phase largely closed, and the waveforms began to overlap; however, the ADS curve followed a parallel deviation trend, staying approximately 2-3 dB above the reference across the entire 1-5 GHz band.

On the other hand, S_{41}, which exhibited the greatest distortion in the ±20% phase by missing the characteristic notches of CST and producing irrelevant peaks, finally began to mimic the general waveform in the ±40% phase. The most prominent deviation was observed in the low-frequency region, where the ADS curve was insufficient in capturing the depth of the first notch around 2.5 GHz. However, in the high-frequency band between 3.5 GHz and 5 GHz, the ADS curve successfully attached to and converged with the reference CST data. Consequently, while the general capture of spectral trends within the ±40% range proves that the equivalent circuit is correctly linked to the physical topology, parallel deviation in S_{31} and amplitude disconnections in the low frequencies of S_{41} are observed.

To determine the numerical effect of the ±40% scanning range on model sensitivity, the spectral data obtained from the final optimization phase were subjected to a detailed error analysis according to the established performance criteria, and the final findings are presented in Table 7.

Table 7. Error (MAE) and Deviation Analysis After ±40% Constrained Optimization

Parameter	MAE (dB)	Max. Deviation (dB)	Frequency (GHz)	Compliance Status
S_{21}	0.56	13.75	2.88	Sufficient Agreement
S_{31}	5.84	15.38	2.724	Non-compliant
S_{41}	2.32	9.02	1.936	Non-compliant
Global MAE	2.90	-	-	Non-compliant

The system is observed to have largely escaped parametric congestion with the expansion of the search space. The reduction of the overall MAE from 5.53 dB to 2.90 dB and the dramatic decrease in the S_{21} port error from 4.01 dB to 0.56 dB prove that the model demonstrates strong convergence and successfully breaks the targeted 1.0 dB 'Sufficient Agreement' barrier. The S_{41} parameter, representing isolation effects, also shows a major recovery compared to previous stages and decreased to 2.32 dB. However, while the algorithm achieves this near-perfect agreement in the primary transmission line, it has traded off the S_{31} parameter, leading to an increased deviation of 5.84 dB in this port. Although the S_{31} parameter has a high amplitude error of 5.84 dB, it follows the waveform and spectral trend of the reference CST data with much higher fidelity. This high error margin in S_{31} stems from a parallel amplitude offset rather than a structural mismatch.

The current equivalent circuit parameter values reached as a result of the optimization process conducted within the ±40% limits are detailed in Table 8. An examination of the parameter variation rates and constraint statuses for the ±40% optimization phase in Table 8 shows that the majority of the circuit elements converged to their optimum values within the search space without pushing the defined tolerance limits. In particular, the critical capacitive and inductive elements characterizing the coupling and resonance dynamics of the structure remained balanced within physically meaningful limits without showing excessive deviations, proving the electrical stability and analytical reliability of the model. Although boundary values were reached for two parameters (R_{f1}, L_f), the high spectral trend tracking achieved across the system and the sufficient agreement in the S_{21} parameter (0.56 dB MAE) confirm that the model has reached the targeted validity level. Consequently, since the majority of the updated parameters remain within the current range and show that the equivalent circuit topology has found its global optimum form without being forced to physical limits, the progressive optimization strategy conducted within the scope of this study was successfully concluded at the ±40% phase.

Table 8. ±40% Constrained Optimization Results and Boundary Value Analysis.

Parameter	***Initial Value***	***±10% Optimization Result***	***Variation (Δ%)***	***Boundary Status***
Lf1	3.07 nH	2.7358 nH	-10.89%	Inside
Cfg1	0.67 pF	0.4966 pF	-25.9%	Inside
Rf1	0.047 Ω	0.0282 Ω	-40%	At Limit
Gf1	0.111 mS	0.1454 mS	+31%	Inside
Lf	2.89 nH	1.7234 nH	-40%	At Limit
Cfg	0.30 pF	0.2798 pF	-6.73%	Inside
Rf	0.056 Ω	0.0598 Ω	+6.78%	Inside
Gf	0.066 mS	0.0692 mS	+4.84%	Inside
Ls	2.17 nH	1.4106 nH	-35%	Inside
Ls1	1.34 nH	1.4740 nH	+10.00%	Inside
Cg	0.46 pF	0.3880 pF	-15.65%	Inside
Cg1	0.25 pF	0.276 pF	+10%	Inside
m	0.95 nH	1.0450 nH	+10.00%	Inside
m1	0.33 nH	0.3953 nH	+19.78%	Inside
Cc	0.73 pF	0.4769 pF	+2.31%	Inside
Cc1	0.054 pF	0.0490 pF	-34.688%	Inside
Rs	0.067 m Ω	0.0705 Ω	+5.22%	Inside
Rs1	0.037 m Ω	0.0395 m Ω	+6.75%	Inside
Gc	0.160 mS	0.1655 mS	+3.43%	Inside
Gcl	0.091 mS	0.0899 mS	-1.20%	Inside
Lcsrr	1.50 nH	1.2002 nH	-19.98%	Inside
Ccsrr	2.04 pF	1.5409 pF	+34.00%	Inside
GCSRR	0.740 mS	0.7304 mS	-1.30%	Inside
CCSRRL	0.84 pF	0.9240 pF	+10.00%	Inside
GCSRRL	0.300 mS	0.3085 mS	+2.83%	Inside
Mcsrr	0.20 nH	0.1600 nH	-20.00%	Inside
Ccl	0.35 pF	0.2800 pF	-20.00%	Inside

RESULTS AND DISCUSSION

In this study, the complex electromagnetic behavior of a four-port directional coupler and CSRR-based microwave sensor structure from the literature was characterized using an original analytical equivalent circuit model developed in ADS. To achieve electrical balance while preserving physical realism, parameter tolerance limits were progressively expanded. This optimization process, constrained to a ±40% range, reduced the overall MAE to 2.90 dB and achieved a success in the S_{21} parameter of 0.56 dB, which is well below the targeted 1.0 dB ideal agreement limit.

Despite remaining within these defined constraints, the near-zero error in S_{21} proves that the model accurately represents the system dynamics. Although parallel amplitude offsets are observed in the S_{31} and S_{41} ports due to multi-port interactions, the spectral waveforms overlap with the reference data with high fidelity. The decision not to expand tolerances beyond the ±40% threshold to completely eliminate the error margin is based on the principle of avoiding the 'curve fitting' pitfall and maintaining physical accuracy.

Furthermore, the proposed progressive optimization strategy has shown that high-Q resonance characteristics can be expressed by an analytical equivalent circuit model without distorting the physical meaning of the circuit elements. This methodology provides a solid framework for the real-time analysis of similar multi-port microwave sensors where computational speed is critical. Future studies can focus on integrating adaptive algorithms into this circuit-based approach to further minimize the parallel offsets observed in the coupling ports. Consequently, this analytical model provides an extremely fast, reliable, and physically grounded strong alternative to time-consuming 3D full-wave simulations, especially during the iterative design processes of microwave sensor development.

REFERENCE

Agarwal, S., and Garg, M. C. (2024). Design of an accurate, planar, resonant microwave sensor for testing a wide range of liquid samples. *Electronics*, 13(22), 4510.

Baena, J. D., Bonache, J., Martin, F., Sillero, R. M., Falcone, F., Lopetegi, T., Laso, M. A. G., Garcia-Garcia, J., Gil, I., Portillo, M. F., and Sorolla, M. (2005). Equivalent-circuit models for split-ring resonators and complementary split-ring resonators coupled to planar transmission lines. *IEEE Transactions on Microwave Theory and Techniques*, 53(4), 1451–1461.

Bahl, I. J. (2003). *Lumped elements for RF and microwave circuits*. Artech House.

Bandler, J. W., Cheng, Q. S., Dakroury, S. A., Mohamed, A. S., Bakr, M. H., Madsen, K., and Sondergaard, J. (2004). Space mapping: The state of the art. *IEEE Transactions on Microwave Theory and Techniques*, 52(1), 337–361.

Cildir, A. (2025). Multifunctional reflective metasurface with wideband linear-to-circular and linear-to-linear polarization conversion. *Optical and Quantum Electronics*, 57(10), 548.

Cildir, A., Tahir, F. A., Jabbar, A., Zahid, A., Rehman, M. ur, Abbas, H., and Abbasi, Q. H. (2025). An efficient broadband metasurface design for smart health care and future communication applications. *Results in Optics*, 19, 100772.

Eroglu, A., and Lee, J. K. (2008). The complete design of microstrip directional couplers using the synthesis technique. *IEEE Transactions on Instrumentation and Measurement*, 57(12), 2756–2761.

Genç, İ., Gözel, M. A., and Kahriman, M. (2026). Microwave sensor design with directional coupler-based CSRR structure for the characterization of the dielectric properties of solid materials. *Measurement*, 259, 119548.

Gozel, M. A., Kahriman, M., and Kasar, O. (2018). Design of an efficiency-enhanced Greinacher rectifier operating in the GSM 1800 band by using rat-race coupler for RF energy harvesting applications. *International Journal of RF and Microwave Computer-Aided Engineering*, e21621.

Kasar, O., Kahriman, M., and Gozel, M. A. (2019). Application of ultra wideband RF energy harvesting by using multisection Wilkinson power combiner. *International Journal of RF and Microwave Computer-Aided Engineering*, 29(1), e21600.

Lei Zhu, and Wu, K. (1999). Unified equivalent-circuit model of planar discontinuities suitable for field theory-based CAD and optimization of M(H)MIC's. *IEEE Transactions on Microwave Theory and Techniques*, 47(9), 1589–1602.

Marcelli, R. (2024). Equivalent circuits for microwave metamaterial planar components. *Sensors*, 24(7), 2212.

Matthaei, G. L., Young, L., and Jones, E. M. T. (1980). *Microwave filters, impedance-matching networks, and coupling structures*. Artech House Books.

Mekki, S., Zegadi, R., Mosbah, S., Sayad, D., Elfergani, I., Bouknia, M. L., Rodriguez, J., Desai, A., Palandoken, M., and Zebiri, C. (2024). Equivalent circuit of a planar microwave liquid sensor based on metamaterial complementary split ring resonator. *Frequenz*, 78(1–2), 37–45.

Pozar, D. M. (2012). *Microwave engineering* (4th ed.). John Wiley and Sons.

Shi, H., Zhang, X., Huang, L., Wang, K., and Wang, Z. (2025). Dual-band planar microwave solid complex dielectric constant sensor system based on E-interdigital structure. *Sensors*, 25(18), 5789.

Swanson, D. G., and Hoefer, W. J. R. (2003). *Microwave circuit modeling using electromagnetic field simulation*. Artech House.

Wu, K., and Li, L. (2005). Numerical calibration and de-embedding techniques for CAD and equivalent circuit models of electromagnetic structures. *Mikrotalasna Revija*, 11(1), 7–19.

Zhou, Y., and Chen, Y. (2008). Lumped-element equivalent circuit models for distributed microwave directional couplers. *International Conference on Microwave and Millimeter Wave Technology*.

Real-Time Supervision and Fault Analysis of a Photovoltaic Plant via WatchPower Software

Amina Azizi [*]

Amina Benabda [2]

Amira Lakhdara [3]

[1,2,3] Dept. of electrical engineering, UBMA, Annaba, Algeria [*]amina.azizi@univ-annaba.dz

ABSTRACT

This paper investigates a real-world case study of a malfunctioning photovoltaic installation that remains in operation and is continuously supervised through the WatchPower monitoring platform. The real-time monitoring system provides continuous data acquisition and enables detailed performance evaluation of the PV installation. The information collected via WatchPower, together with on-site visual inspection findings, allowed the detection of operational anomalies and the assessment of their influence on the system's overall efficiency. Based on this analysis, a practical real-time fault monitoring and diagnosis methodology for photovoltaic systems was developed. The proposed approach was modeled and simulated in MATLAB/Simulink and subsequently integrated with the WatchPower monitoring environment to verify its reliability and effectiveness under actual operating conditions.

Keywords – Photovoltaic generator, Modeling, Diagnostic, WatchPower software, Real-time simulation

I. INTRODUCTION

Solar energy is a valuable renewable energy source. In fact, this inexhaustible source of energy could, in the future, become a reliable alternative to traditional energy sources in order to meet the growing energy demands of individuals and global industry. Indeed, small and medium-consumption applications in remote and rural areas benefit greatly from this type of energy. The faults that photovoltaic installations undergo are a major concern for researchers, as the presence of these faults exponentially reduces the kilowatts produced by the plants. Several solutions have been proposed in the literature, but they remain limited given the complexity of the problems[1].

during its design, installation, or operation. These faults reduce the performance of standalone photovoltaic systems, which in turn affects photovoltaic production. A practical approach for monitoring and fault detection in PV systems intended for online implementation is developed in this article. The monitoring and fault detection model presented here is built using MATLAB/Simulink and the WatchPower software. As with every industrial process, a photovoltaic system may be subject, during his operation, to various faults and abnormalities leading to a drop in its efficiency up to its unavailability. A precise diagnosis and fault detection and isolation make it possible to reduce the maintenance costs and above all increase the yield[2]. In this work, a focus has been made on the fault detection and isolation in the DC part of the PV system, it means of the PV array. In this work, we analyze the design and simulate the photovoltaic system to follow the maximum power of the photovoltaic generator.In this

work, we analyze the design and simulation of the photovoltaic system to follow the maximum power of the photovoltaic generator. The goal of this work is to propose, by conducting the less possible measurements to meet the economic constraints, an approach to detect and isolate the faults causing a drop in the array yield. To achieve this goal, the analysis of the I-V characteristic has been chosen. This analysis leads to the use of the watchpower software, to conduct the diagnosis of the PV plant. This procedure has been validated by on-site experiments, real-time simulations, and non-real-time simulations[3]. “Fig. 1” shows our project:

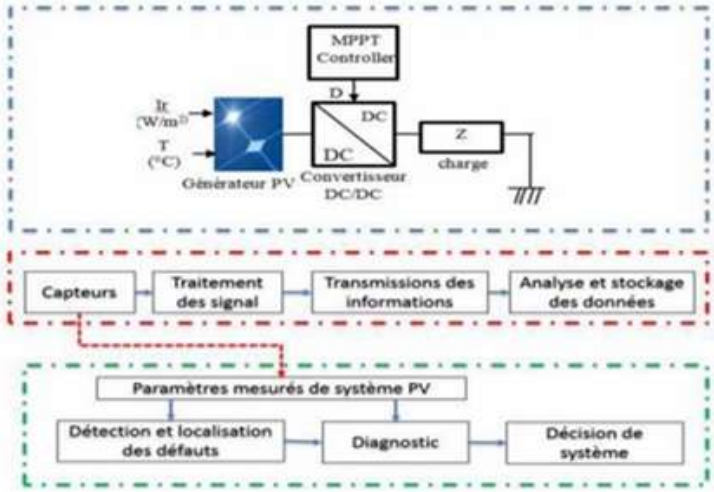

Fig.1. Configuration of the system.

II. MATERIALS AND METHOD

A. Solar panel

The solar panel mainly consists of 36 cells that combine in series and in parallel. These photovoltaic cells are made of silicon; we used two panels in parallel to increase the current so that we could supply the pump. The electrical characteristics of The main equation of the cell is given by[3]:

$$I_{pv} = I_{ph} - I_{sat}\left[\exp\left(\frac{e(V_{pv} + (Ipv * R_{Ser}))}{nKT}\right) - 1\right] - \frac{V_{pv} + (Ipv * R_{Ser})}{R_{shu}} \quad (1)$$

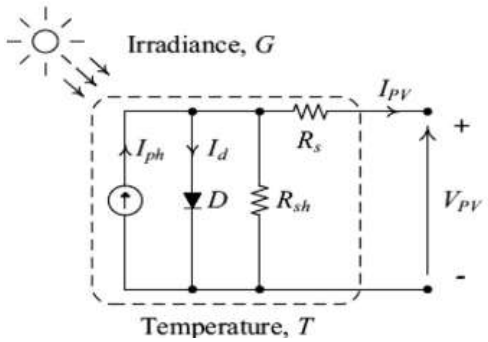

Fig.2. Electrical equivalent circuit of the photovoltaic cell

Solar panel characterization is done by connecting the solar panel in series with the ammeter followed by a rheostat and voltmeter connected across the rheostat. In our case we use a multi-meter. The resistance is varied and corresponding solar panel voltage and current are recorded, the I-V and P-V curves plotted for tow solar panels in series is shown in the below “fig 3”.

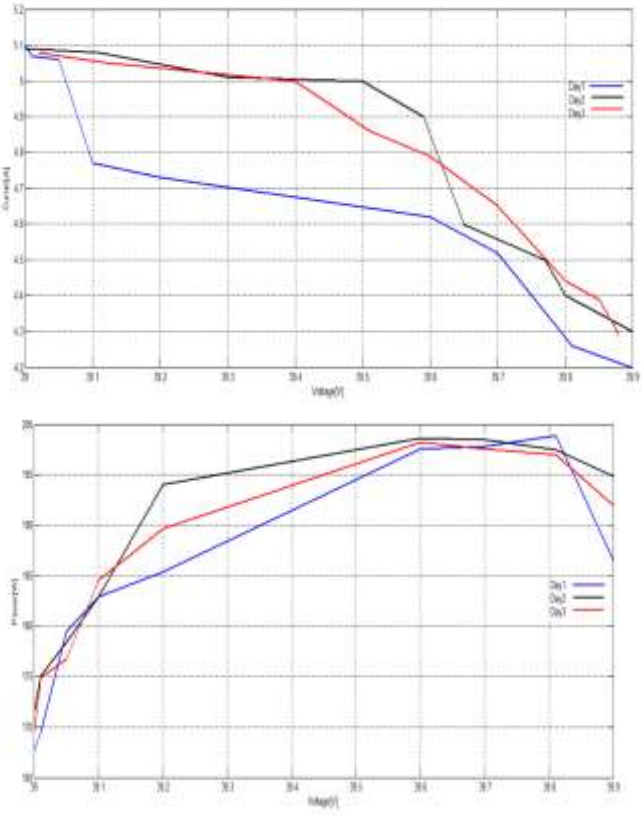
Fig. 3. I-V/P-V Characteristics of solar panel

B. Converter

.

To improve the performance of the solar panel, we used the RG-PT series charge controller, shown in Figure 4. This controller, equipped with an LCD display, incorporates a DC-DC converter with advanced technology that enables the maximum power point (MPPT) of the photovoltaic array to be tracked quickly and accurately, whatever the environmental conditions. This allows the maximum power from the solar panels to be exploited in real time, increasing the efficiency of the energy system. In addition, this controller is equipped with an RS-485 communication interface, meeting communication needs in a variety of environments. This is controlled by an MPPT tracking algorithm that we have developed, enabling in-depth analysis of the system's efficiency, stability and performance under a variety of solar conditions. The aim is to optimise the integration of photovoltaic panels and improve their operation in specific applications such as solar pumping. The relation between input and output voltages of the boost converter is given as[4]:

$$V_{out} = \frac{1}{1-D} V_{in} \qquad (2)$$

With D is the duty cycle which given as:

$$D = \frac{T_{on}}{T_s} \qquad (3)$$

With Ton is the on-state time of the IGBT and TS is the total switching time [5].

Fig.4 MPPT converter

The algorithm included in this converter is perturb and observe named P&O.In this method the controller adjusts the voltage by a small amount from the array and measures power; if the power Increases, further adjustments in that direction are tried until power no longer increases. This is called the perturb and observemethod, although this method can result in oscillations of power output. It is referred to as a hill climbing method, because it depends on the rise of the curve of power against voltage below the maximum power point, and the fall above that point. The flowchart in this method is shown in “fig.5” [6].

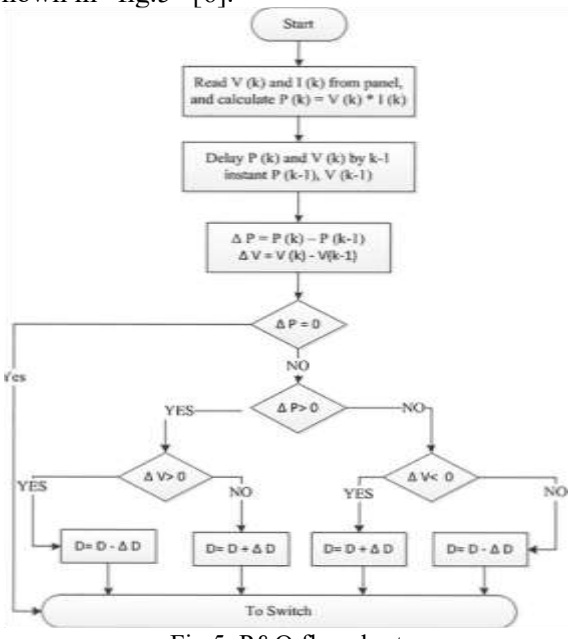

Fig.5. P&O flowchart

C. Inverter

The three-phase inverter with Pulse Width Modulation (PWM), is employed in this work. Among the available modulation techniques, Space Vector Pulse Width Modulation (SVPWM) has been adopted, as it is widely recognized as the most advanced approach for sinusoidal waveform synthesis, providing a higher output voltage with reduced total harmonic distortion [7].

The principle of vector modelling (SVPWM) consists of reconstructing the voltage vector ref from eight voltage vectors. Each of these vectors corresponds to a combination of the states of the switches in a three-phase voltage inverter. SVPWM is the method recently best suited to the control of inverter-powered AC motors, unlike other methods. It can detect additional fault conditions on the network, such as unbalanced or distorted situations,

and adapt the system accordingly, reducing losses and improving system efficiency [8].

Fig.6. Inverter

III. WORKING OF PROPOSED SYSTEM

In this experiment, WatchPower monitored the power output on a sunny day, May 24, 2024, with data recorded from 00:00 to 23:30 (a full day). Fig 7 shows our proposed system.

Fig.8 PV installation system

WatchPower is a monitoring software connected to the inverter that can supervise multiple devices simultaneously through a serial port. The main functions of the WatchPower monitoring software include data logging for connected devices, alarm messages, fault messages, and device configuration.To achieve this, a roadmap is established according to the following procedure[9,10]:

- Monitoring of the installation over a full sunny day using WatchPower
- A comparison between two experiments:
- A normal day without any faults in the photovoltaic installation
- A day with a shading fault.

Fig.8. Watch power

VI. Results and discussions

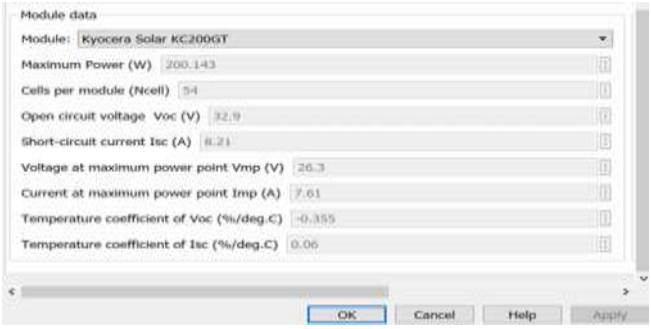

Fig.9. Module data

The block diagram of the PV system used is shown in Figure 9:

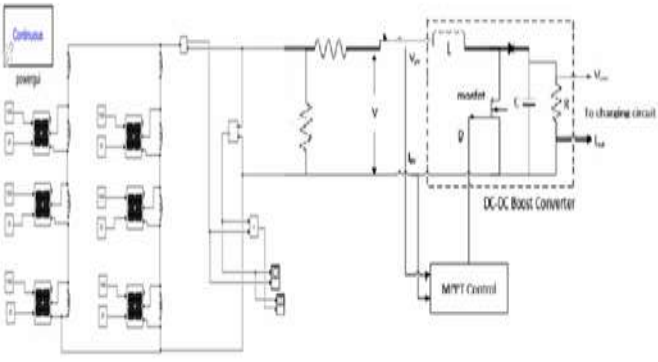

Fig.9. block diagram of the PV system used

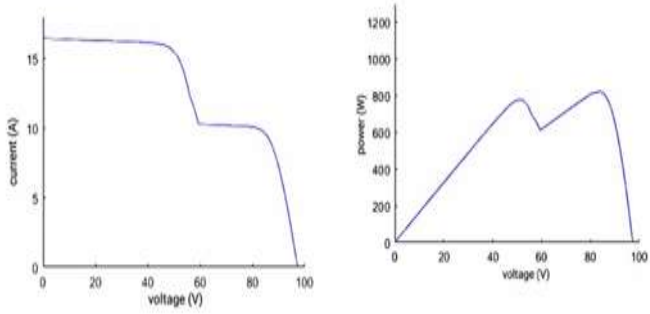

Fig.10. shading effect on two modules

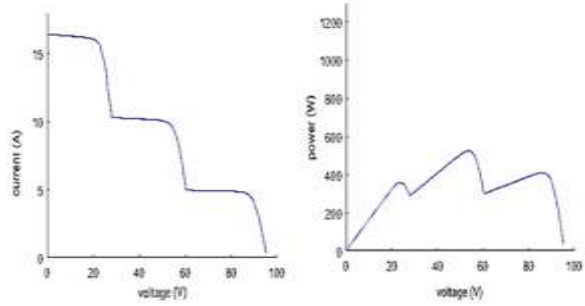

Fig.11. the shading effect on four modules

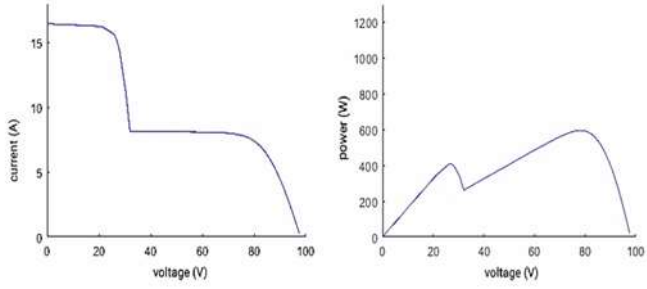

Fig.12 effect of a ground fault

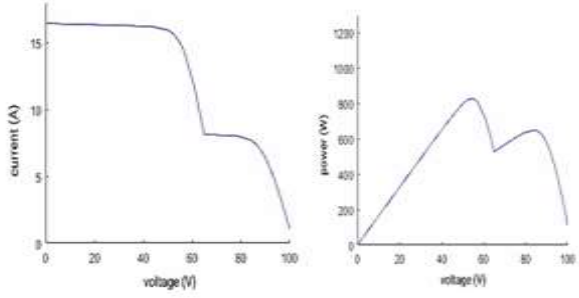

Fig.13. effect of a line-to-line fault

Watch power results:

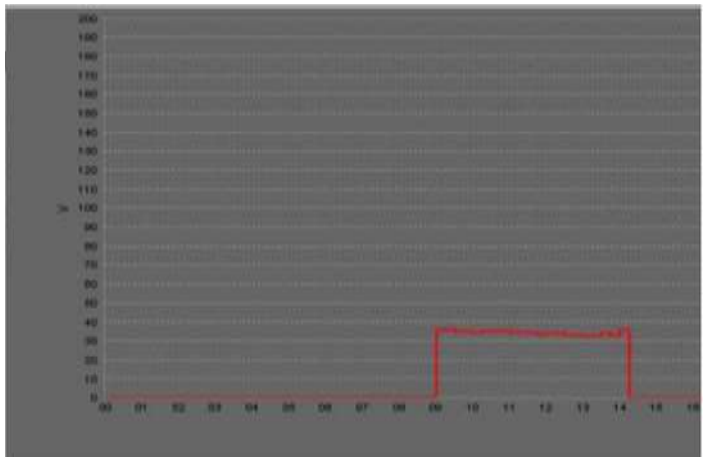

Fig.14 Input voltage of the PV installation

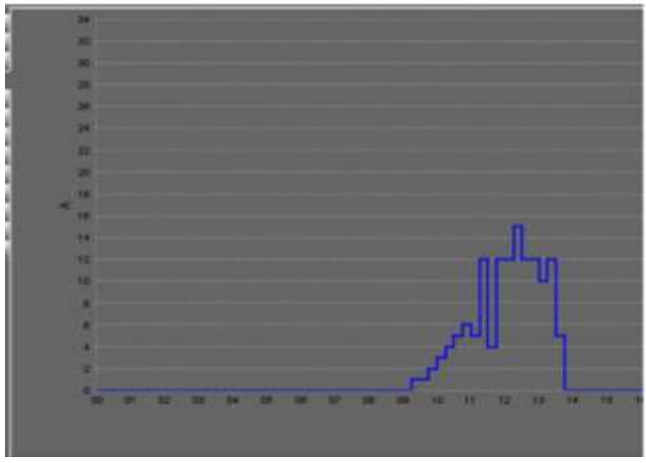

Fig.15 Input current of the PV installation

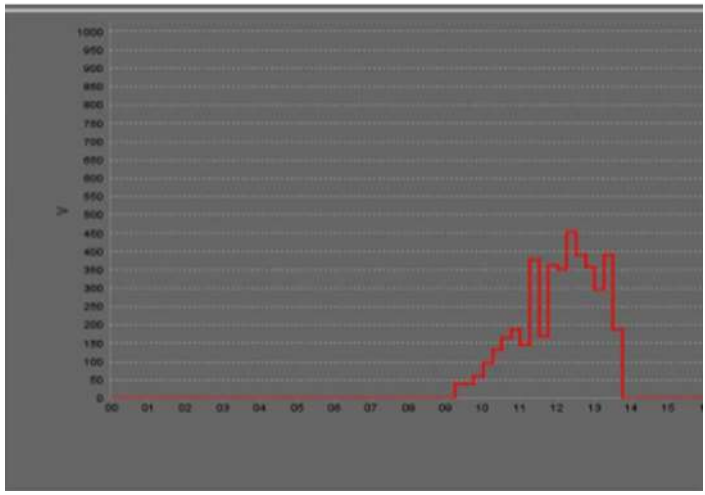

Fig.16. Input Power of the PV installation

Instability in electrical energy production is clearly observed throughout the operating period, mainly as a consequence of partial shading affecting the photovoltaic array. Shading reduces the amount of incident irradiance and therefore limits the ability of the panels to operate at their optimal power point, which explains the fluctuations recorded in voltage, current, and output power.

The maximum voltage of the system, approximately 35 V at 09:00 (Figure IV.35), corresponds to a period of relatively low irradiance, where the PV modules operate closer to open-circuit conditions. As the solar input increases, the current becomes the dominant parameter, reaching a peak of 15 A at 12:00 (Figure IV.36), consistent with the moment of highest solar exposure. This rise in current leads to a maximum power of 450 W at around 12:15, when both voltage and current reach favorable operating conditions.
The slight temporal shift between the maxima of current and power is characteristic of systems affected by shading and temperature variations, which modify the I–V characteristics of the modules and prevent perfectly synchronized peak production. Overall, these observations confirm that shading episodes have a significant impact on the system's energy stability and highlight the importance of real-time monitoring and fault detection to maintain reliable PV performance.

V. CONCUSION

This study examines a real damaged photovoltaic installation using a combined methodology that integrates on-site inspection with continuous real-time monitoring through the WatchPower platform. The correlation between field observations and operational data enabled the identification of multiple anomalies and the evaluation of their impact on the overall system performance.

The fault-diagnosis model developed in MATLAB/Simulink proved to be effective when implemented under actual operating conditions, demonstrating the advantage of combining analytical modeling with monitoring software for practical diagnostic applications. The findings emphasize the critical role of real-time supervision in ensuring the reliability, operational safety, and long-term efficiency of photovoltaic installations, particularly in the presence of aging effects or partially degraded components.

Furthermore, this work highlights the potential of monitoring platforms such as WatchPower as supportive tools for preventive maintenance and early fault detection. Future research could explore the integration of advanced diagnostic approaches, including machine learning and predictive algorithms, to enhance detection precision and enable proactive performance management strategies.

REFERENCES

[1] Ling-Ling, Guo-Qian Lin, Ming-Lang Tseng, Kimhua Tan, Ming K. Lim e, "A maximum power point tracking method for PV system with improved gravitational search algorithm"science direct, volume (65),2018.

[2] Seddik, H., et al, "Solar Energy Potential in Algeria and Future Perspectives". Proceedings of the Renewable Energy Symposium, pp. 31-38. ,2021.

[3] YanisPrunier, David Chuet, Sylvain Nicolay, GwenaëlleHamon, MaximeDarnon a b,"Optimization of photovoltaic panel tilt angle for short periods of time or multiple reorientations". Science direct,volume (20),2023.

[4] Abbes, H., Abid, H., et al,"Comparative Study of Five MPPT Control Algorithms for a PV System". International Conference on Renewable Energy, Sousse, Tunisia 2013.

[5] Azizi, A., &Logerie, P.-O,"Impact of Photovoltaic Module Aging on Grid-Connected System Performance". Solar Energy, 174, 445-454,2018.

[6] Khan, Z. U., Khan, A. D., Khan, K., Al Khatib, S. A. K., Khan, S., Khan, M. Q., & Ullah, A. (2024). A review of degradation and reliability analysis of a solar PV module. IEEE Ac cess, 12, 185036-185056.

[7] Yadav, Dinesh, and Amit Kumar Saraf. "Analysis of the visual degradation of PV modules installed in different climatic zones in India." Environment, Development and Sustainabil ity (2025): 1-23.

[8] Kaplani, E. (2015, December). PV cell and module degradation, detection and diagnostics. In Renewable Energy in the Service of Mankind Vol II: Selected Topics from the World Re newable Energy Congress WREC 2014 (pp. 393-402). Cham: Springer International Pub lishing

[9] Bouguerra, S., Agroui, K., Kaaya, I., Bouraiou, A., Yaiche, M. R., & Mansour, D. E. (2021). Modeling the effect of PV module orientation on the encapsulant browning degradation rate in Algeria region. IEEE Journal of Photovoltaics, 12(1), 274-284.

[10] Jadin, Mohd Shawal, et al. "A Device for Evaluating Photovoltaic (PV) Module Output Per formance and Degradation." Proceedings of the 6th International Conference on Electrical, Control and Computer Engineering:

InECCE2021, Kuantan, Pahang, Malaysia, 23rd Au gust. Singapore: Springer Singapore, 2022.

A Compact Denim-Based Flexible Wearable Antenna for 2.45 GHz ISM Band

Yağmur KÜÇÜKBOYACI [*]

Merih PALANDÖKEN [2]

[1]Department of Electrical and Electronics Engineering, İzmir Katip Çelebi University, Turkey
[2] Department of Electrical and Electronics Engineering, İzmir Katip Çelebi University, Turkey
[*](yagmurkbyc@gmail.com) [2](merih.palandoken@ikcu.edu.tr)

ABSTRACT

This study has presented a compact and flexible wearable antenna designed on a denim textile substrate for 2.45 GHz Industrial, Scientific, and Medical (ISM) band applications. The proposed antenna has featured a miniaturized footprint of 22 x 24 mm², which has been achieved through the strategic introduction of optimized slot geometries and a partial ground plane to extend the effective surface current path. Simulation results in free space have shown a stable resonance at 2.45 GHz with a reflection coefficient of -16.55 dB, confirming the accuracy of the design for the target frequency. Mechanical reliability has been confirmed through bending tests along both the x and y axes using various radii, where the antenna has maintained a reflection coefficient below the -10 dB threshold across the simulated cases. For the on-body analysis, a 4 mm separation distance has been maintained between the antenna and the phantom to represent a realistic air gap or clothing layers, resulting in a deeper resonance of -32.88 dB at 2.335 GHz over the tissue model. Additionally, a comprehensive Specific Absorption Rate (SAR) analysis has been performed, yielding a peak value of 0.59 W/kg for 100 mW input power, which has remained well below the FCC safety limit of 1.6 W/kg. Overall, the findings of this research have established that the proposed design has provided a robust, safe, and portable solution for modern Wireless Body Area Networks (WBAN) and advanced wearable healthcare monitoring systems.

Keywords – Wearable antenna, Wireless Body Area Network (WBAN), 2.45 GHz ISM band, Denim substrate, Specific Absorption Rate (SAR), Bending analysis

I. INTRODUCTION

Wireless Body Area Network (WBAN) technology has become a fundamental component in modern healthcare monitoring and real-time physiological sensing [1], [2]. Wearable devices operating within these networks have primarily utilized the 2.45 GHz Industrial, Scientific, and Medical (ISM) band due to its global standardization and high compatibility with Bluetooth-low-energy communication protocols [3], [4]. For such systems to be effective and commercially viable, the antennas have been required to be flexible, lightweight, and seamlessly integrable into daily clothing to ensure user comfort and mobility during long-term monitoring [5], [6].

The proximity of the human body has presented significant electromagnetic challenges, as high- permittivity and lossy tissues have caused resonant frequency detuning and a substantial reduction in radiation efficiency [7], [8]. Optimizing specific slot geometries on the radiating patch and employing partial ground planes have offered a compact and cost-effective solution to mitigate these effects while maintaining a low-profile structure [9], [10].

Denim fabric has been widely preferred as a substrate in wearable antenna designs due to its mechanical robustness, low cost, and low dielectric constant, which has supported enhanced impedance bandwidth and stable electromagnetic performance even under mechanical stresses [10], [11], [12].

This study has presented a compact microstrip patch antenna designed on a denim substrate for the 2.45 GHz ISM band. The proposed design has been rigorously analyzed using a realistic three-layer human tissue model consisting of skin, fat, and muscle to evaluate its performance in close proximity to the body. A comprehensive Specific Absorption Rate (SAR) analysis has been performed to ensure that the electromagnetic radiation levels remain within international safety limits for human health. Additionally, the mechanical reliability of the design has been verified through bending tests at different radii, simulating the typical movements of a wearer. The combination of optimized slot geometry and textile substrate has provided a robust radiation performance and frequency stability in both free space and complex on-body environments.

II. MATERIALS AND METHOD

The proposed wearable antenna has been designed on a flexible denim substrate (εr = 1.7, h = 1.0 mm, $\tan\delta$=0.02) compact physical area of 22 x 24 mm² to operate in the 2.45 GHz ISM band. To achieve a compact and robust configuration, the design has featured a microstrip patch radiator optimized with specific slot geometries and a partial ground plane. Numerical modeling and electromagnetic simulations have been conducted to characterize the antenna performance. To evaluate the design in a realistic environment, a three-layer human tissue model consisting of skin, fat, and muscle has been developed. The dielectric properties and thicknesses of each layer have been defined according to international standards to simulate the interaction between the antenna and the human body.

A. Antenna Design

Figure 1 has presented the final geometry of the proposed textile wearable antenna, where Fig. 1(a) has shown the top view of the radiating structure and Fig. 1(b) has shown the back view with the partial ground plane. The corresponding geometric dimensions have been given in Table 1. The antenna has been designed on a denim substrate using a compact and symmetric patch configuration with a total physical area of 22 x 24 mm². To achieve resonance at 2.45 GHz within this limited physical size, several slots and truncated sections have been introduced into the radiating patch in order to extend the effective current path. In addition, the partial ground plane on the back side has

improved impedance matching and has supported wider bandwidth performance. The final dimensions have been selected through parametric analysis of the S11response to obtain proper operation in the ISM band and to ensure a characteristic impedance of 50 Ω at the center frequency.

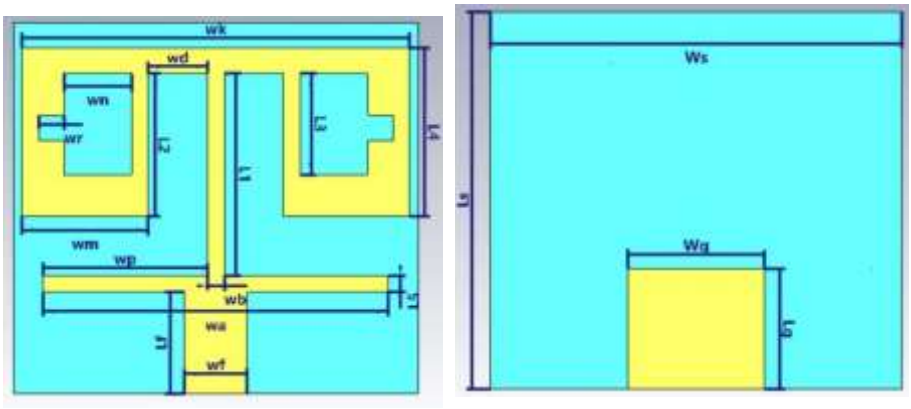

(a) (b)

Fig. 1 Detailed geometry of the proposed wearable antenna a) top view. b) back view.

Table 1. Geometric parameters and physical dimensions of the proposed antenna.

Parameter	Value (mm)	Parameter	Value (mm)
Ls	22	Wm	7.50
Ws	24	Wr	1.5
Lg	7	Wn	4
Wg	8	Wk	23
Lf	6	L1	12
Wf	3.70	L2	8.50
Wa	20.50	L3	6
Wb	1	L4	10
Wp	9.75	L5	1
Wd	3.5	h	1

III. RESULTS

The performance of the proposed denim-based antenna has been evaluated through numerical simulations under free-space conditions to determine its impedance matching and resonant behavior. The simulated reflection coefficient of the optimized design in free space has been presented in Fig. 2. As observed, the antenna has attained a deep resonance at 2.45 GHz with a minimum value of approximately

-16.55 dB. Since this result has been well below the standard -10 dB threshold, it has indicated efficient power transfer and satisfactory matching at the target ISM frequency. This response has confirmed that the slot-loaded patch configuration effectively has supported reliable operation for 2.45 GHz applications such as Bluetooth and Wi-Fi.

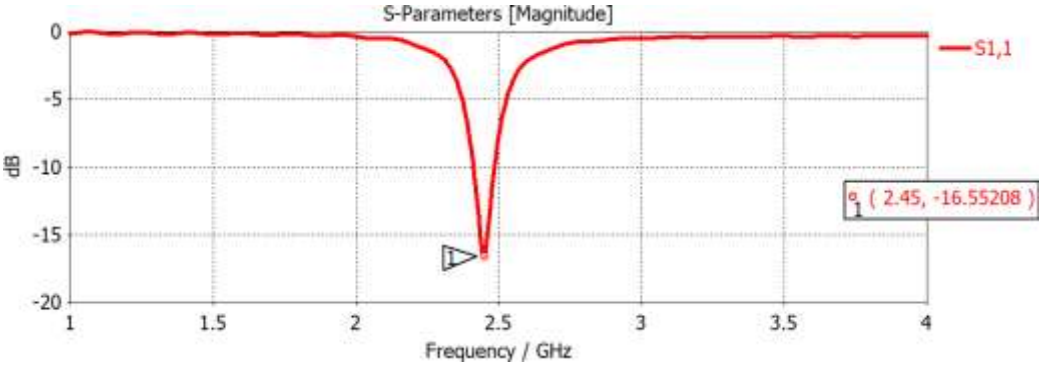

Fig. 2 Simulated reflection coefficient (S11) of the proposed wearable antenna in free space.

To achieve the target resonance at the 2.45 GHz ISM band, a parametric study has been conducted on the *wb* parameter. As has been illustrated in Fig. 3, varying *wb* from 0.5 mm to 2 mm has led to a significant shift in the resonant frequency. It has been observed that increasing the value of *wb* has caused an upward frequency shift. Based on these results, *wb* = 1 mm has been selected as the optimal dimension, as it has provided a distinct resonance at exactly 2.45 GHz with a reflection coefficient (S11) of-16.55 dB, ensuring excellent impedance matching for the intended application.

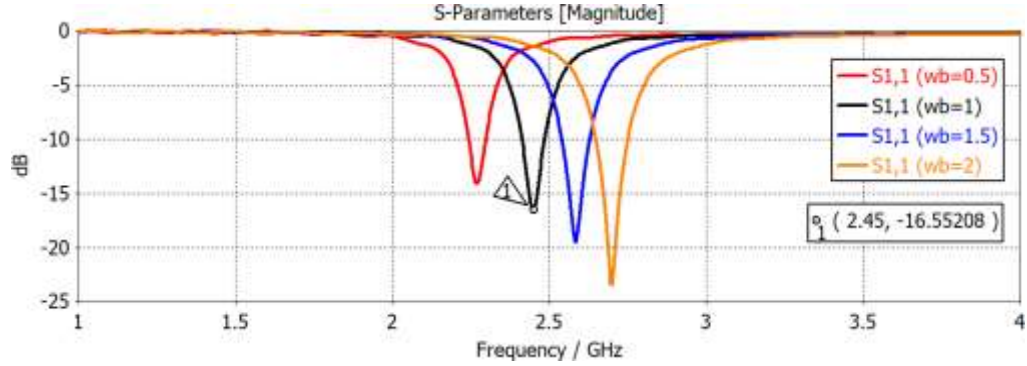

Fig. 3 Parametric study of the wb parameter on the simulated reflection coefficient.

The surface current distribution of the proposed antenna at 2.45 GHz has been illustrated in Fig. 4. It has been observed that the current has been primarily concentrated along the microstrip feed line and the edges of the radiating patch.

The strategic placement of slots and notches has effectively redirected the surface current, forcing it to follow a longer electrical path. This behavior has confirmed the miniaturization principle of the design, enabling the antenna to achieve resonance at the target ISM frequency within a compact physical footprint.

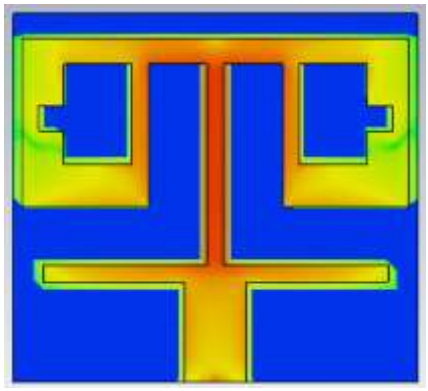

Fig. 4 Simulated surface current distribution of the proposed antenna at 2.45 GHz.

The radiation characteristics of the proposed antenna at 2.45 GHz in the ϕ = 90° plane have been presented in Fig. 5. Far-field analysis has revealed that the antenna has achieved a realized gain of 0.717 dBi and a 3 dB beamwidth of 88.9°. The wide radiation pattern has been advantageous for wearable systems, since it has supported stable communication performance under different body orientations. Despite the dielectric losses associated with the denim substrate, the antenna has demonstrated efficient radiation behavior, which has confirmed its suitability for the target wearable application.

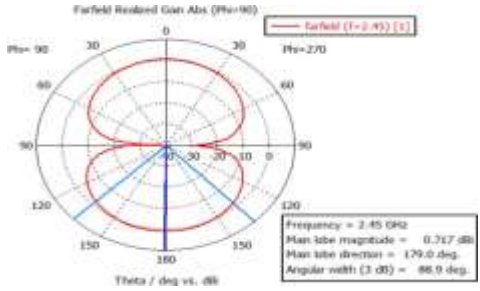

Fig. 5 Far-field radiation pattern at 2.45 GHz in the Phi = 90° plane.

Considering the flexible nature of the denim substrate, the antenna's performance under mechanical deformation has been evaluated. Bending

simulations have been conducted along both the x and y axes to emulate its behavior when worn on different parts of the human body. Various bending radii have been applied for each orientation to investigate the impact of physical bending on the resonance characteristics. The simulated S11 characteristics for various bending radii ranging from 10 mm to 60 mm along the x-axis and y-axis have been presented in Fig. 6a and Fig. 6b respectively. It has been observed that as the bending radius has decreased towards tighter curvatures, a slight shift in the resonance frequency has occurred. However, the antenna has maintained a reflection coefficient well below the -10 dB threshold across the 2.45 GHz band for all tested cases. This stability has demonstrated that the proposed denim- based antenna has been robust against physical deformations and has ensured reliable performance when integrated into clothing on various parts of the human body.

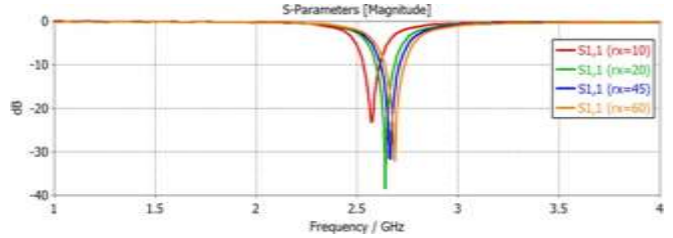

(a)

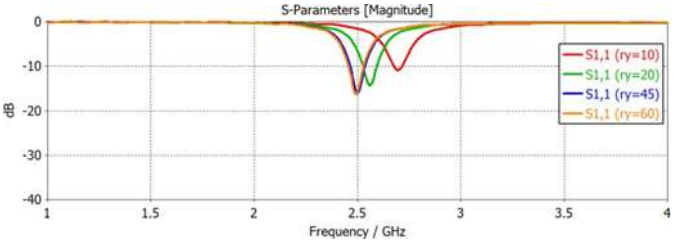

(b)

Fig. 6 Simulated S11 characteristics for various bending radii along the (a) x-axis (b) y-axis.

The performance of the proposed wearable antenna has been investigated using a multilayered human arm model to simulate realistic on-body conditions. The simulation setup has been presented in Fig. 7 from two different perspectives to provide a comprehensive understanding of the antenna-body interaction.

Specifically, the perspective view in Fig. 7a has demonstrated the spatial positioning and the overall footprint of the denim antenna as it has been integrated onto the arm phantom. This three-dimensional representation has highlighted the alignment and orientation of the radiating elements over the heterogeneous human tissue structure. Furthermore, Fig. 7b has provided the cross-sectional side view of the simulation environment, showing the vertical arrangement of the antenna relative to the tissue layers. In this configuration, a fixed separation distance of 4 mm has been maintained between the bottom of the antenna substrate and the top of the skin layer. This gap has been intentionally implemented to represent a realistic scenario involving an air gap or additional clothing layers, which has been crucial for mitigating the frequency detuning and impedance mismatch caused by the high permittivity of the human body.

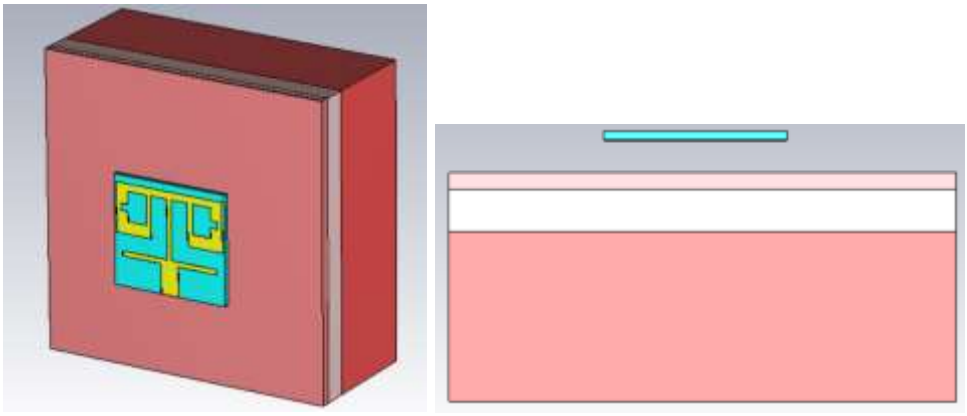

(a) (b)

Fig. 7 Simulation setup of the proposed wearable antenna on the three-layer human arm phantom: (a) perspective view, and
(b) side view.

The phantom has been composed of skin, fat, and muscle layers, each having been characterized by its specific electromagnetic properties. The detailed permittivity (εr), conductivity (σ), mass density (ρ), and thickness of these biological tissues at 2.45 GHz have been summarized in Table 2.

Table 2. Dielectric properties and thicknesses of the human arm tissue layers at 2.45 GHz.

Tissue Layer	Permittiviy (ϵr)	Conductivity (σ) (S/m)	Density (ρ) (kg/m³)	Thickness (mm)
Skin	37.95	1.49	1001	2
Fat	5.27	0.11	900	5
Muscle	52.67	1.77	1006	20

In practical wearable scenarios, direct contact between the radiating element and the human skin has been unrealistic due to the antenna's substrate, protective layers, or underlying clothing. Therefore, a parametric sweep has been conducted to evaluate the performance at various separation distances ranging from 1 mm to 4 mm over the tissue phantom to simulate these realistic conditions. As has been illustrated in Fig. 8, while a significant frequency shift has occurred at a very close proximity of 1 mm due to the high-permittivity loading of the tissues, the performance has stabilized as the gap has increased. This study has confirmed that a 4 mm separation distance, representing a typical air gap or a standard clothing layer, has effectively balanced the body loading effect and resonance stability.

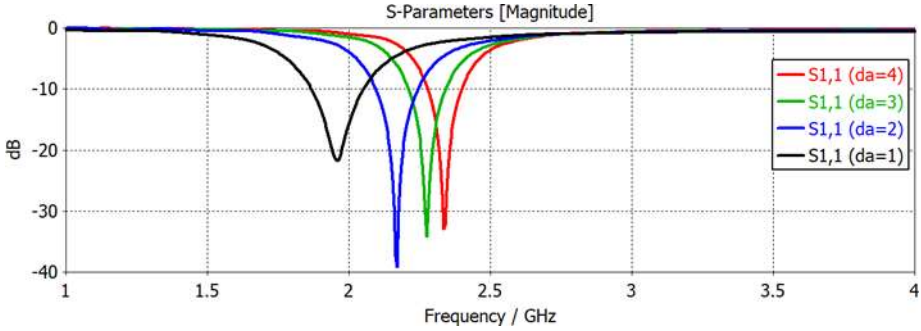

Fig. 8 Simulated reflection coefficient (S11) characteristics for various separation distances between the proposed antenna and the human tissue phantom.

Following the parametric study, a 4 mm distance has been selected as the optimized configuration for on-body analysis. The simulated reflection coefficient at this distance has been presented in Fig. 9. Over the tissue phantom, the antenna has exhibited a very deep resonance of -32.88 dB at 2.335 GHz. Despite the slight frequency detuning compared to the free-space resonance an expected outcome of the loading effect from the tissue phantom the antenna has provided excellent impedance matching. These results have demonstrated that the antenna has remained highly efficient and reliable when worn over clothing in a real-world environment.

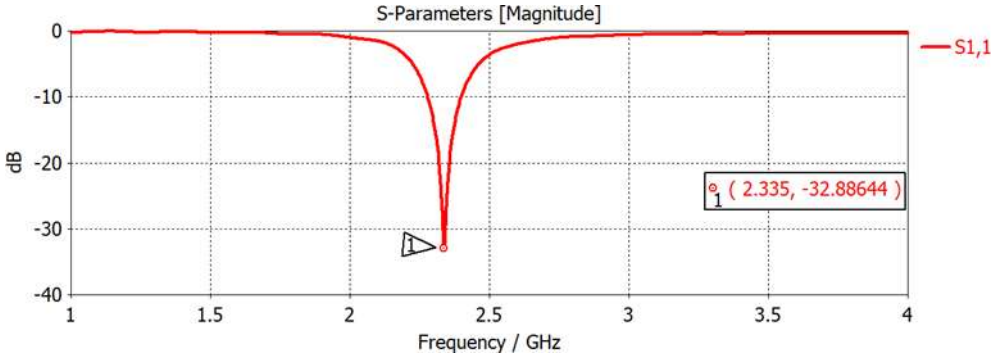

Fig. 9 Simulated reflection coefficient (S11) result of the optimized antenna placed over the human tissue phantom.

Specific Absorption Rate (SAR) analysis has been conducted to evaluate the electromagnetic safety of the proposed wearable antenna when operating near the human body. The simulated SAR distribution on the tissue phantom at 2.45 GHz has been illustrated in Fig. 10. For an input power of 100 mW, the peak SAR value averaged over 1 g of tissue has been found to be 0.59 W/kg. This result has been well within the safety limit defined by the Federal Communications Commissions (FCC), which is 1.6 W/kg for 1 g of tissue. The low SAR value has demonstrated that the denim-based antenna has minimized electromagnetic radiation exposure to the user, making it highly suitable for long-term wearable applications.

Fig. 10 Simulated SAR distribution of the proposed wearable antenna on the human tissue phantom at 2.45 GHz.

IV. DISCUSSION

The results obtained from the numerical simulations and on-body analyses have demonstrated that the proposed denim-based antenna has achieved the design objectives for 2.45 GHz WBAN applications. The compact physical footprint of 22×24 mm has distinguished this design from conventional patch antennas, which are typically larger at the target ISM frequency. This miniaturization has been attained through the introduction of specific slot geometries and truncated sections, which have redirected the surface current to follow a longer electrical path. This strategy has allowed the antenna to maintain its resonance within a limited physical space while using a flexible denim substrate.

The interaction between the antenna and the human body has provided technical insights into the design's robustness. A frequency shift from 2.45 GHz in free space to 2.335 GHz on the tissue phantom has been observed. This phenomenon has been attributed to the body loading effect, where the high permittivity of the skin and muscle layers increases the effective capacitance of the system. However, the 4 mm separation distance has effectively mitigated excessive detuning, ensuring that the antenna has remained operational near the target band. Furthermore, the reflection coefficient has reached -32.88 dB on the body, which has indicated that the tissue phantom has contributed to an improved impedance matching at that specific configuration.

Regarding mechanical reliability, the bending tests have confirmed that the denim substrate has maintained its electromagnetic integrity even at the tightest bending radius of 10 mm. This flexibility, combined with the 22×24 mm dimensions, has suggested that the antenna has been well-suited for integration into wearable accessories or curved body parts. Furthermore, the realized gain of 0.717 dBi and the broad 3 dB beamwidth of 88.9° have provided a stable radiation characteristic in the $\phi = 90°$ plane. This has been considered an advantage for wearable sensors, as it has supported consistent connectivity regardless of the wearer's orientation. Finally, the SAR value of 0.59 W/kg has remained well below the FCC limit of 1.6 W/kg. This performance has established that the proposed design has balanced compactness with user safety and radiation efficiency. Overall, the findings have confirmed that the combination of denim material and optimized slot geometry has resulted in a robust and safe solution for modern healthcare monitoring systems.

V. CONCLUSION

In this study, a compact denim-based wearable antenna with dimensions of 22 x 24 mm^2 has been presented for 2.45 GHz WBAN applications. The results have demonstrated that the antenna has achieved satisfactory

impedance matching, stable radiation performance, and reliable operation under both bending and on-body conditions. The optimized slot geometries have enabled effective miniaturization by extending the surface current path without increasing the overall footprint of the antenna. In addition, the design has maintained its performance under mechanical deformation and has exhibited a low SAR value of 0.59 W/kg, which has remained well below the FCC safety limit. These findings have confirmed that the proposed antenna represents a robust and safe solution for the evolving requirements of modern Wireless Body Area Network systems and smart textile platforms.

REFERENCES

[1] A. K. Arya et al., "Compact BLE Antenna with a Modified PIFA Configuration for Wearable EMG Monitor," IEEE Sensors Journal, vol. 23, no. 15, pp. 17648-17655, 2023.

[2] F. Wang et al., "Dual-Broadband Dual-Mode Wearable Antenna for On/Off-Body WBAN Communications," IEEE Antennas and Wireless Propagation Letters, vol. 24, no. 12, pp. 4565-4569, 2025.

[3] S. N. Mahmood et al., "ON-OFF Body Ultra-Wideband (UWB) Antenna for Wireless Body Area Networks (WBAN): A Review," IEEE Access, vol. 8, pp. 150844-150863, 2020.

[4] K. N. Paracha et al., "Wearable Antennas: A Review of Materials, Structures, and Innovative Features," IEEE Access, vol. 7, pp. 56694-56712, 2019.

[5] A. L. Sharon Giftsy et al., "Flexible and Wearable Antenna for Biomedical Application: Progress and Opportunity," IEEE Access, vol. 12, pp. 90016-90040, 2024.

[6] A. Al-Azza et al., "A review on textile antennas for wearable electronics," Modern Applied Science, vol. 12, no. 10, pp. 1-15, 2018.

[7] S. Segun and A. Telukdarie, "Revolutionizing Healthcare Delivery Through Wireless Wearable Antenna Frameworks," IEEE Access, vol. 11, pp. 80327-80347, 2023.

[8] R. Salvado et al., "Textile materials for the design of wearable antennas: A survey," Sensors, vol. 12, no. 11, pp. 15841- 15857, 2012.

[9] Z. Hamouda et al., "Flexible dual-band antenna for wearable applications," Microwave and Optical Technology Letters, vol. 60, no. 5, pp. 1220-1227, 2018.

[10] U. Ali et al., "Design, Analysis and Applications of Wearable Antennas: A Review," IEEE Access, vol. 11, pp. 14458- 14486, 2023.

[11] T. T. Le and T.-Y. Yun, "Wearable Dual-Band High-Gain Low-SAR Antenna for Off-Body Communication," IEEE Antennas and Wireless Propagation Letters, vol. 20, no. 7, pp. 1175-1179, 2021.

[12] X. Yin, S. J. Chen, and C. Fumeaux, "Wearable Dual-Band Dual-Polarization Button Antenna for WBAN Applications," IEEE Antennas and Wireless Propagation Letters, vol. 19, no. 12, pp. 2240-2244, 2020.

Evaluating User Preferences in Electric Vehicle Selection Using BWM and MARCOS Methods: A Case Study of Erzurum

Zişan ÖZÇELİK [1]

Müjde ARSLAN [1]

Ferhat YUNA [1*]

Mahmut Sami ŞAŞMAZTÜRK [2]

[1] Department of Industrial Engineering, Faculty of Engineering and Architecture, Erzurum Technical University, Erzurum, Türkiye
[2] Department of Management Information Systems, Faculty of Business and Management Sciences, Iskenderun Technical University, Hatay, Türkiye
[*](ferhat.yuna@erzurum.edu.tr)

ABSTRACT

With the rapid increase in the use of electric vehicles, the vehicle selection process for consumers has become a complex problem requiring the simultaneous evaluation of numerous variables. This study aims to determine the most suitable electric vehicle model in Erzurum province, taking into account user expectations and the challenging climatic conditions of the region. The research utilizes the Best-Worst Method (BWM) and MARCOS (Measurement of Alternatives and Ranking According to Compromise Solution) approaches from Multi-Criteria Decision Making (MCDM). First, evaluation criteria (price, range, charging time, battery performance, service network, etc.) were determined based on user expectations in Erzurum, and the weighting of these criteria was calculated using the BWM method. Then, leading electric vehicle alternatives in the market were ranked using the MARCOS method with these weightings. The data obtained from the applied model showed that certain criteria gained weight due to the effect of cold climate conditions on the battery. This study serves as an important guide for both consumers and industry stakeholders by numerically demonstrating the impact of regional dynamics on electric vehicle preference.

Keywords – Electric Vehicles, Multi-Criteria Decision Making (MCDM), BWM Method, MARCOS Method, Erzurum.

I. INTRODUCTION

The environmental impact of fossil fuels has accelerated the transition to electric vehicles (EVs) in the automotive sector. However, factors such as initial investment costs, charging infrastructure, and especially "range anxiety" make consumer choices difficult. These challenges are even more pronounced in regions like Erzurum, where winters are long and harsh. Extremely cold weather negatively affects the performance of lithium-ion batteries, reducing driving range significantly below standard factory specifications. Therefore, a consumer in Erzurum needs to focus much more on regional criteria such as cold-weather range performance and thermal management systems when purchasing an EV.

Vehicle selection, which requires the simultaneous evaluation of many conflicting criteria (high range, low cost, etc.), is a complex MCDM problem. Although there are studies on EV selection in the literature, research focusing on regional climate dynamics is quite limited. The aim of this study is to determine the most suitable model among the electric vehicle alternatives on the market, taking into account the challenging climatic conditions of Erzurum and local user expectations.

Accordingly, two robust MCDM methods were integrated into the study. The BWM, which allows for consistent calculation of criterion weights with fewer pairwise comparisons, was used; and the ranking of alternatives was

performed using the MARCOS method, which focuses on flexible and ideal/anti-ideal solutions. The aim of the study is to contribute to both the literature and the sector by numerically demonstrating the impact of challenging climatic conditions on EV preferences.

There are many studies in the literature that examine the preferences of EV users and market dynamics. In their studies, Yılmaz and Demir [1], Turan and Akın [2], Aydın and Şahin [3] and Güneş and Yıldız [4] examined the main factors affecting EV preferences in the Turkish market with the help of surveys and statistical analyses. In these studies, the decisive role of criteria such as price, range, battery capacity, charging time and service network in consumer decisions was emphasized.

In problems with numerous conflicting criteria, such as EV selection, the use of MCDM methods is frequently preferred in the literature. The integrated use of BWM and MARCOS methods, in particular, has come to the forefront in recent years. Kara and Özkan [5], Özdemir [6], Ersoy and Kaplan [7], Çetin [8], Öztürk and Karaca [9], Arslan and Yılmaz [10] and Polat and Demirtaş [11] evaluated EV models and ranked alternatives using BWM and MARCOS methods. These studies prove that the aforementioned methods are quite successful in reflecting consumer trends in mathematical models.

To the best of the author's knowledge, a review of the relevant literature revealed that while there are comprehensive studies addressing the EV market and user preferences in Türkiye using MCDM methods, no study was found that directly modeled the impact of regional climate differences (especially harsh winter conditions in places like Erzurum) on user priorities. This study distinguishes itself from previous studies by filling this gap in the literature and examining existing BWM-MARCOS approaches within the specific context of expectations in Erzurum.

II. Materials and Method

This study presents a numerical analysis based on MCDM methods to determine the most suitable electric vehicle model for the challenging climate and geographical conditions of Erzurum province. The negative impacts of regional dynamics such as high altitude, low temperatures, and long winters on the battery efficiency and range of electric vehicles were considered. The goal is to create a decision model that reflects real-world usage conditions, going beyond standard factory data.

This evaluation examines five different electric vehicles from the C-SUV and compact SUV segments available in the Turkish market, which offer advantages in the region's rugged terrain and heavy snowfall conditions. To ensure systematic analysis, alternative models were coded from A1 to A5 (EV-73X, EV-41Y, EV-92Z, EV-58W, EV-16Q) and integrated into the model. The study's dataset was created using a multi-source approach; manufacturer catalogs were used for technical specifications and range values, while safety data was supported by independent review reports, and subjective

criteria such as service accessibility and user experience were supported by expert opinions.

The comprehensive material structure created constitutes the fundamental analytical infrastructure of the research. Based on the data obtained, the BWM was used to determine the importance levels (weights) of the decision criteria, and the MARCOS method was used to ultimately rank the alternative tool models according to regional needs. Thanks to this integrated structure, both technical performance indicators and user-oriented evaluations were successfully combined in a single model.

To evaluate the suitability of electric vehicles for the challenging winter and geographical conditions of Erzurum province, nine key decision criteria were determined, encompassing technical performance, economic factors, and user experience, in line with regional requirements. In this context, range (C1) and battery capacity (C2), which are vital for continuous use in the face of the risk of battery performance degradation in cold weather conditions, and the heat pump option (C8), which minimizes range loss by providing energy efficiency in cabin heating, were included in the model within the context of regional dynamics. Motor power/performance (C3), which directly affects driving safety on the province's rugged and snowy road surfaces, and safety perception (C4), based on independent tests, represent the technical and safety capabilities of the vehicles. Price (C5), considered as the only cost-oriented (minimization) criterion in the analysis, constitutes the economic dimension of the decision-making process. In addition, service/dealer accessibility (C6), which is critical for uninterrupted use in challenging climatic conditions and after-sales satisfaction, charging network compatibility (C7), which indicates fast charging infrastructure capacity, and domestic/imported perception (C9), a qualitative factor reflecting brand trust through ease of maintenance, were used as other key criteria that completed the evaluation framework.

A. Best–Worst Method (BWM)

BWM is a Multi-Criteria Decision Making (MCD) method developed by Rezaei in 2015 that requires fewer comparisons than classical pairwise comparison methods [12]. The method is based on calculating the relative importance of other criteria based on the best and worst criteria determined by the decision-maker. The basic steps followed in applying the BWM method are as follows:

Step 1: Determining the Set of Decision Criteria

The decision-maker identifies n criteria that are effective in solving the problem:

$$C = \{c_1, c_2, \dots, c_n\} \quad (1)$$

Step 2: Selecting the Best and Worst Criteria

The decision-maker selects the "Best Criterion" (c_B), which has the highest impact on the problem, and the "Worst Criterion" (c_W), which has the lowest impact, from the defined set of criteria. No numerical scoring is done at this stage.

Step 3: Creating the Preference Vector (A_B) of the Best Criterion Compared to Other Criteria

The superiority of the best criterion (B) over all other criteria (j) is determined using a Saaty scale between 1 and 9. Here, a_{Bj} represents the preference of the best criterion over criterion j, and a_{BB} = 1. The resulting vector is as follows:

$$A_B = (a_{B1}, a_{B2,}, \dots, a_{B2}) \quad (2)$$

Step 4: Creating the Preference Vector (A_W) of Other Criteria Compared to the Worst Criterion

The superiority of all other criteria (j) over the worst criterion (W) is determined. Here, a_{jW} represents the preference of criterion j over the worst criterion, and a_{WW} = 1.

$$A_W = (a_{1W}, a_{2W}, \dots, a_{nW})^T \quad (3)$$

Step 5: Calculating Optimal Weights (w)*

The goal of the BWM method is to ensure that for each criterion j, the ratio $\frac{w_B}{w_j}$ is as close as possible to the value a_{Bj} and the ratio $\frac{w_j}{w_W}$ is as close as possible to the value a_{jW}. To this end, the following linear programming model is established, minimizing absolute differences:

Objective Function:

$$Min\ \xi L \quad (4)$$

Subject to:

$$| w_B - a_{Bj} * w_j | \leq \xi L \qquad \forall j \in \{1, \dots, n\} \quad (5)$$

$$| w_j - a_{jW} * w_W | \leq \xi L \qquad \forall j \in \{1, ..., n\} \quad (6)$$

$$\sum w_j = 1 \qquad \forall j \in \{1, ..., n\} \quad (7)$$

$$w_j \geq 0 \qquad \forall j \in \{1, ..., n\} \quad (8)$$

Solving this model yields the optimal criterion weights (w*) and the coefficient of consistency (ξ*).

Step 6: Calculating the Consistency Ratio

The Consistency Ratio (CR) is calculated to test the reliability of the obtained results. The closer the CR value is to 0, the more consistent the comparisons are.

$$CR = \xi^* / CI \qquad (9)$$

Here, CI is a constant coefficient that depends on the degree to which the best criterion is preferred over the worst criterion (a_{BW}).

B. MARCOS Method (Measurement of Alternatives and Ranking according to COmpromise Solution)

The MARCOS method used in comparing alternatives calculates the utility functions of alternatives according to ideal and anti-ideal reference points [13].

Step 1: Creating the Initial Decision Matrix
A matrix consisting of m alternatives and n criteria is created. The xij value shows the performance of the i-th alternative in the j-th criterion.

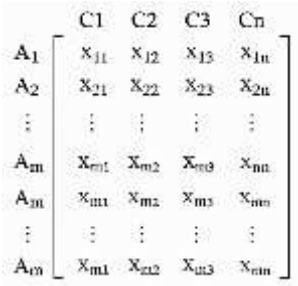

(10)

Step 2: Creating the Extended Decision Matrix
Ideal (AI) and Anti-Ideal (AAI) solution rows are added to the matrix.

$$AAI = min(x_{ij}) \quad \textit{(If benefit-oriented criteria)} \quad (11)$$

$$AAI = max(x_{ij}) \quad \textit{(If cost-oriented criteria)} \quad (12)$$

$$AI = max(x_{ij}) \quad \textit{(If benefit-oriented criteria)} \quad (13)$$

$$AI = min(x_{ij}) \quad \textit{(If cost-oriented criteria)} \quad (14)$$

Step 3: Normalization of the Decision Matrix (N)
Data in different units are normalized (n_{ij}):

$$n_{ij} = x_{ij}/x_{ai} \quad \text{(for benefit-oriented criteria)} \quad (15)$$

$$n_{ij} = x_{ai}/x_{ij} \quad \text{(for cost-oriented criteria)} \quad (16)$$

Step 4: Creating the Weighted Matrix (V)

The weights (w_j) found with BWM are multiplied by the normalized values:

$$v_{ij} = n_{ij} * w_j \quad (17)$$

Step 5: Calculating Benefit Levels

The total score (S_i) of each alternative is calculated:

$$S_i = \sum v_{ij} \quad \forall j \in \{1, \ldots, n\} \quad (18)$$

Next, the utility levels (K_i) of the alternatives are examined in relation to the Ideal and Anti-Ideal solutions:

$$K_i^- = S_i / S_{(AAI)} \quad (19)$$

$$K_i^+ = S_i / S_{(AI)} \quad (20)$$

Step 6: Determining the Utility Functions of the Alternatives

$$f(K_i^-) = K_i^+ / (K_i^+ + K_i^-) \quad (21)$$

$$f(K_i^+) = K_i^- / (K_i^+ + K_i^-) \quad (22)$$

Step 7: Calculating the Final Ranking Score $f(K_i)$

The score that determines the final ranking of the alternatives is calculated as follows:

$$f(K_i) = (K_i^+ + K_i^-) / (1 + (1 - f(K_i^+)) / f(K_i^+)) + (K_i^+ + K_i^-) / (1 + (1 - f(K_i^-)) / f(K_i^-)) \quad (23)$$

The alternative with the highest obtained $f(K_i)$ value is the one with the best performance.

III. RESULTS

A. Determining Criterion Weights with BWM

In the first stage of the research, the opinions of five different field experts were sought to determine the relative importance weights of the nine evaluation criteria. The decision-making expert group consisted of automotive industry professionals, academics working in the relevant field, and experienced electric vehicle users. The data obtained from the expert evaluations were transferred to MS Excel, and mathematical models were analyzed using the Excel Solver add-in. According to the BWM methodology, each decision-maker determined the most important (Best) and least important (Worst) criteria based on their own knowledge and experience; then, all other criteria were subjected to pairwise comparisons on a 1-9 importance scale against these two reference criteria. The established mathematical model was run independently for each expert, and optimal weight vectors with consistency ratios (CR) within acceptable limits were obtained for all decision-makers. To illustrate the application steps, the BWM analysis results and calculated consistency test findings for the first expert (Expert 1) are presented in the relevant image.

Figure 1. BWM results from Expert 1.

Figure 1 shows that the Input-Based Consistency Ratio (CR) for the relevant expert is 0.071. This value being below the acceptable threshold of 0.10 proves that the expert's evaluation is consistent and reliable. The data for the other four experts were analyzed similarly, and all were confirmed to be consistent (CR < 0.10). Table 1 shows the criterion weights for each of the five experts separately.

Table 1. Expert-Based Criterion Weights

Expert / Criteria	**C1**	**C2**	**C3**	**C4**	**C5**	**C6**	**C7**	**C8**	**C9**
Expert1	0,04884	0,07327	0,0628	0,04945	0,05495	0,07327	0,1099	0,4396	0,08792
Expert2	0,24347	0,14252	0,14252	0,08551	0,05344	0,02969	0,10689	0,05344	0,14252
Expert3	0,0678	0,0565	0,19915	0,04237	0,33898	0,0678	0,11299	0,08475	0,02966
Expert4	0,04165	0,06664	0,20825	0,06664	0,27073	0,02083	0,11107	0,0476	0,1666
Expert5	0,24347	0,14252	0,14252	0,08551	0,05344	0,02969	0,10689	0,05344	0,14252

B. Selection of Alternatives Using the MARCOS Method

The criterion weights determined by the BWM method were integrated using the geometric mean method to represent multiple expert opinions, and the final weight values to be used in the MARCOS analysis were obtained. Following the weighting phase, alternative vehicle models ((A1) EV-73X ,

(A2) EV-41Y , (A3) EV-92Z, (A4) EV-58W , (A5) EV-16Q) were evaluated using the MARCOS method.

Step 1: Creating the Initial Decision Matrix

First, an Initial Decision Matrix was created by collecting technical data (range, price, engine power, etc.) for the vehicles. Additionally, "Ideal" (AI) and "Anti-Ideal" (AAI) solution rows were added to this matrix as required by the MARCOS method.

Table 2: Extended Initial Decision Matrix

	Decision Variables								
	Max	**Max**	**Max**	**Max**	**Min**	**Max**	**Max**	**Max**	**Max**
Weights	0,088	0,089	0,105	0,042	0,132	0,109	0,103	0,064	0,269
Vehicle Model/Criteria	**C1**	**C2**	**C3**	**C4**	**C5**	**C6**	**C7**	**C8**	**C9**
Anti-Ideal Solution	**380**	**49**	**156**	**7**	**3.465.000**	**5**	**6**	**0**	**0**
(A1) EV-73X	600	77	514	9	3.465.000	5	10	1	0
(A2) EV-41Y	500	87	218	8	2.358.000	7	8	1	0
(A3) EV-92Z	523	89	218	8	2.371.000	9	9	0	1
(A4) EV-58W	605	81	204	6	2.100.000	8	7	1	0
(A5) EV-16Q	380	49	156	7	2.184.000	8	6	1	0
Ideal Solution	**605**	**89**	**514**	**9**	**2100000**	**9**	**10**	**1**	**1**

Step 2: Normalization Process

A normalization process was applied to make the data, which has different units (TL, km, kWh), comparable. The values of benefit-oriented criteria (Range, Battery, etc.) and cost-oriented criteria (Price) were converted to a range of 0-1 through normalization.

Table 3: Normalized Decision Matrix

	Decision Variables								
	Max	**Max**	**Max**	**Max**	**Min**	**Max**	**Max**	**Max**	**Max**
Weights	0,088	0,089	0,105	0,042	0,132	0,109	0,103	0,064	0,269
Vehicle Model/Criteria	**C1**	**C2**	**C3**	**C4**	**C5**	**C6**	**C7**	**C8**	**C9**
Anti-Ideal Solution	**380/605 = 0.63**	**0,55**	**0,30**	**0,67**	**1**	**0,56**	**0,60**	**0**	**0**
(A1) EV-73X	600/605 =0.99	0,87	1,00	1,00	0,61	0,56	1,00	1	0
(A2) EV-41Y	500/605 =0.82	0,98	0,42	0,89	0,89	0,78	0,80	1	0
(A3) EV-92Z	523/605 =0.64	1,00	0,42	0,89	0,89	1,00	0,90	0	1
(A4) EV-58W	605/605 =1,00	0,91	0,40	0,67	1,00	0,89	0,70	1	0
(A5) EV-16Q	380/605 =0.63	0,55	0,30	0,78	0,96	0,89	0,60	1	0
Ideal Solution	**1**	**1**	**1**	**1**	**0.61**	**1**	**1**	**1**	**1**

Step 3: Weighted Normalized Decision Matrix

Following the normalization process, the final criterion weights (w_j) obtained using the BWM method and combined with the geometric mean were multiplied by the normalized values ($v_{ij} = n_{ij}*w_j$). This process resulted in a weighted matrix that also

includes the importance levels of the criteria. As shown in Table 4, the row sum (S_i) of each alternative was calculated at this stage.

Table 4: Weighted Normalized Decision Matrix

	Decision Variables										
	Max	**Max**	**Max**	**Max**	**Min**	**Max**	**Max**	**Max**	**Max**	**S_{AAI}**	**S_i**
Weights	0,088	0,089	0,105	0,042	0,132	0,109	0,103	0,064	0,269		
Vehicle Model/Criteria	**C1**	**C2**	**C3**	**C4**	**C5**	**C6**	**C7**	**C8**	**C9**		
Anti-Ideal Solution	**0,055**	**0,049**	**0,105**	**0,0423**	**0,132**	**0,060**	**0,062**	**0**	**0**	**0,5053**	
(A1) EV-73X	0,087	0,077	0,105	0,0423	0,010544	0,060	0,103	0,064	0		0,5488
(A2) EV-41Y	0,072	0,087	0,044	0,0376	0,194	0,085	0,082	0,064	0		0,6656
(A3) EV-92Z	0,056	0,089	0,044	0,0376	0,193	0,109	0,092	0	0,269		0,8896
(A4) EV-58W	0,088	0,081	0,041	0,0282	0,217	0,097	0,072	0,064	0		0,6882
(A5) EV-16Q	0,055	0,049	0,032	0,0329	0,209	0,097	0,062	0,064	0	**S_i**	0,6009
Ideal Solution	**0,088**	**0,089**	**0,032**	**0,0282**	**0,217**	**0,109**	**0,103**	**0,064**	**0,269**	**0,9992**	

Step 4: Calculating Utility Levels and Functions

Using the total score (Si) of each alternative, utility levels (K_i^- and K_i^+) were calculated for both Ideal (S_i) and Anti-Ideal (S_{AAI}) solutions. These values indicate how close an alternative is to the ideal solution and how far it is from the worst-case scenario.

Table 5: Utility Levels of Alternatives

Vehicle Model/Criteria	S_{AAI}	S_i	K_i^-	K_i^+
Anti-Ideal Solution	0,5053			
(A1) EV-73X		0,6703	1,327	0,671
(A2) EV-41Y		0,6656	1,317	0,666
(A3) EV-92Z		0,8896	1,761	0,890
(A4) EV-58W		0,6882	1,362	0,688
(A5) EV-16Q	**S_i**	0,6009	1,189	0,601
Ideal Solution	0,9992			

Step 5: Final Ranking Results

In the final stage of the MARCOS method, the utility function f(K_i) was calculated for each alternative and ranked from largest to smallest. According to the calculation results, the vehicle with the highest f(K_i) value was determined to be the most suitable choice for Erzurum conditions.

Table 6: The Final Ranking of Electric Vehicles

Vehicle Model/Criteria	K_i^-	K_i^+	$f(K_i^-)$	$f(K_i^+)$	f(Ki)	Ranking
(A1) EV-73X	1,327	0,671	0,336	0,664	0,574	**3**
(A2) EV-41Y	1,317	0,666	0,336	0,664	0,569	**4**
(A3) EV-92Z	1,761	0,890	0,336	0,664	0,761	**1**
(A4) EV-58W	1,362	0,688	0,336	0,664	0,588	**2**
(A5) EV-16Q	1,189	0,601	0,336	0,664	0,514	**5**

The final utility scores of the alternatives obtained from numerical analyses performed using BWM and MARCOS methods to solve the electric vehicle selection problem in Erzurum province are shown in Table 6. When the analyses are examined, the A3 EV-92Z model ranked first with the highest calculated utility score (0.761).

IV. DISCUSSION

An examination of the findings clearly reveals the dramatic impact of regional dynamics on the decision-making process. The A3 (EV-92Z)'s first-place ranking is largely due to its high "Domestic/Imported Perception" score, competitive price/performance balance, and high accessibility to service/dealers in the region (C6). In a city like Erzurum, where range anxiety is high in winter conditions, after-sales support and integration with fast charging stations have outweighed standard technical advantages (e.g., pure engine power).

V. CONCLUSION

In this study, an MCDM model was developed for users in Erzurum province, evaluating the advantages of local production, service accessibility, and technical equipment features suitable for winter conditions. Using integrated BWM and MARCOS methods, electric vehicle alternatives in the C-SUV segment were ranked with a strong mathematical foundation. As a result of the analysis, the A3 (EV-92Z) was calculated as the most optimal choice for the region's conditions. In future studies, the scope of the model can be expanded by conducting comparative analyses between different climate zones.

ACKNOWLEDGMENT

We would like to express our gratitude to all the industry experts and electric vehicle users who contributed their valuable insights and time to the weighting of evaluation criteria and the selection of alternatives during the analysis phase of this research.

REFERENCES

[1] Yılmaz, A., & Demir, B. (2022). "Türkiye'de Elektrikli Araç Tercihlerini Etkileyen Faktörler." Uluslararası Ulaşım ve Lojistik Dergisi.
[2] Turan, S., & Akın, F. (2020). "Elektrikli Araçlarda Kullanıcı Tercih Analizi: Türkiye Örneği." Otomotiv Teknolojileri Dergisi.
[3] Aydın, R., & Şahin, P. (2021). "Türkiye'de Elektrikli Araç Pazar Analizi ve Kullanıcı Tercihleri." Enerji ve Ulaşım Dergisi.
[4] Güneş, H., & Yıldız, F. (2019). "Türkiye'de Elektrikli Araçların Pazar Analizi ve Kullanıcı Öncelikleri." Enerji Politikaları Dergisi.
[5] Kara, E., & Özkan, H. (2021). "Çok Kriterli Karar Verme Yöntemleri ile EV Model Sıralaması." Endüstri Mühendisliği ve Sistem Analizi Dergisi.
[6] Özdemir, M. (2019). "BWM ve MARCOS Yöntemlerinin Elektrikli Araç Değerlendirmesinde Kullanımı." Yöneylem Araştırması ve Karar Bilimi Dergisi.
[7] Ersoy, T., & Kaplan, M. (2020). "Elektrikli Araç Kullanıcı Tercihlerinin Çok Kriterli Karar Verme Yöntemleriyle Analizi." Otomotiv ve Teknoloji Dergisi.
[8] Çetin, B. (2021). "BWM ve MARCOS Yöntemleri ile Elektrikli Araç Değerlendirme." Sistem Analizi ve Endüstri Mühendisliği Dergisi.

[9] Öztürk, S., & Karaca, E. (2022). "Türkiye'de Elektrikli Araç Pazarında Kullanıcı Tercihleri ve Stratejik Analiz." Ulusal Ulaşım ve Enerji Dergisi.
[10] Arslan, D., & Yılmaz, H. (2020). "Çok Kriterli Karar Verme Yöntemleri ile Elektrikli Araç Model Değerlendirmesi." Otomotiv Endüstrisi Dergisi.
[11] Polat, K., & Demirtaş, R. (2019). "Elektrikli Araç Modellerinin Türkiye Pazarı İçin Analizi." Enerji ve Taşımacılık Araştırmaları Dergisi.
[12] Rezaei, J. (2015). Best-worst multi-criteria decision-making method. Omega, 53, 49-57.
[13] Stević, Ž., Pamučar, D., Puška, A., & Chatterjee, P. (2020). Sustainable supplier selection in healthcare industries using a new MCDM method: Measurement of alternatives and ranking according to Compromise solution (MARCOS). Computers & industrial engineering, 140, 106231.

Design and Machine Learning-Based Analysis of a High-Gain Reflector-Backed Dual-Band Antenna for Wi-Fi Applications

Mehmet Efe SÖNMEZ[*]

Merih PALANDÖKEN [2]

[1]Department of Electrical and Electronics Engineering,İzmir Katip Çelebi University, Turkey
[2]Department of Electrical and Electronics Engineering,İzmir Katip Çelebi University, Turkey
[*](mehmetefe576@gmail.com)
[2](merih.palandoken@ikcu.edu.tr)

ABSTRACT

This paper presents the design and performance analysis of a compact, dual-band microstrip antenna integrated with a metallic reflector for high-gain Wi-Fi applications targeting the 2.45 GHz and 5.2 GHz frequency bands. The radiating structure employs a modified cross-dipole configuration printed on an FR-4 substrate, where the integration of a metallic reflector at an optimal quarter-wavelength distance significantly enhances the broadside gain. The proposed antenna achieves peak realized gains of 5.8 dBi at 2.45 GHz and 3.26 dBi at 5.2 GHz, effectively demonstrating a 4.47 dB gain improvement compared to the reflector-less configuration. Beyond the hardware design, this study introduces a machine learning-based surrogate modeling approach to predict the antenna's reflection coefficient (S11), bypassing the need for computationally intensive full-wave 3D electromagnetic simulations. Three distinct algorithms—Random Forest (RF), Support Vector Regression (SVR), and Gradient Boosting Regressor (GBR)—were evaluated, with the Random Forest model achieving the highest prediction accuracy with an R^2 score of 0.8963. The results validate that the combination of reflector-backed high-gain antenna design and machine learning-driven performance prediction provides a robust and computationally efficient framework for the optimization of modern wireless communication systems.

Keywords – Dual-band antenna, cross-dipole, metallic reflector, high-gain antenna, machine learning, S-parameter prediction.

I. INTRODUCTION

Wireless communication systems have become an indispensable part of modern society, forming the backbone of the global digital economy. This technological revolution is fueled by the explosive proliferation of Internet of Things (IoT) devices, the insatiable demand for high-definition media streaming, and the continuous evolution of wireless standards such as Wi-Fi and 5G/6G networks [1]. This exponential growth necessitates the development of advanced hardware components capable of supporting higher data rates, wider bandwidths, and reliable connectivity across increasingly congested frequency spectrums [2]. Among these components, the antenna plays the most critical role, acting as the transducer between guided electromagnetic waves in the circuitry and unguided waves in free space. The performance of an antenna, therefore, directly dictates the efficiency, range, and quality of the entire wireless link.

For modern Wireless Local Area Network (WLAN) applications, operating seamlessly across the 2.4 GHz and 5 GHz frequency bands is a fundamental requirement. Consequently, dual-band antennas that can cater to both of these Wi-Fi standards in a single compact structure are highly sought after [3]. Moreover, to enhance signal penetration through obstacles, improve link budget, and extend coverage area, antennas with high directional gain are

particularly crucial for applications such as indoor access points, routers, and point-to-point communication links. While numerous microstrip antennas have been proposed for dual-band operation, achieving high gain without significantly increasing the antenna's physical footprint remains a persistent design challenge.

To address these challenges, crossed dipole antennas have emerged as a highly versatile candidate. As extensively detailed in the literature [4], the fundamental crossed dipole typically consists of two orthogonal half-wavelength ($\lambda/2$) radiating elements. While they inherently produce omnidirectional or isotropic patterns, integrating them with a metallic reflector at an optimal quarter-wavelength ($\lambda/4$) spacing effectively redirects the back-radiation, yielding a high-gain unidirectional profile. Furthermore, to meet modern multiband requirements within compact footprints, conventional straight dipole arms are frequently modified into multi-branched, meandered, or asymmetrically shaped configurations. These structural modifications manipulate the resonant electrical lengths, allowing a single radiating structure to support multiple frequency bands seamlessly [4].

Recent advancements in crossed-dipole designs have primarily focused on extending impedance bandwidth and maximizing directional gain. For instance, an ultra-wideband circularly polarized antenna backed by a modified cavity was demonstrated in [5]. By utilizing fan-shaped and triangular dipole arms, the authors achieved an impressive fractional impedance bandwidth of over 125% alongside a peak gain of 12.2 dBic. Beyond single-element enhancements, deploying crossed dipoles in multiple-input multiple-output (MIMO) systems introduces significant mutual coupling challenges. To address this, a 1×2 CP crossed-dipole MIMO array was investigated in [6], where a single metallic post was strategically inserted between the elements. This modification effectively shifted the self-decoupled band, enhancing port isolation by 13 dB and maintaining it above 20 dB across the entire operational bandwidth. In another study aiming for a low-profile and broadband CP performance, a uniplanar crossed-dipole antenna utilizing corner-cut fat dipoles and an integrated tapered balun was proposed in [7]. This compact design effectively suppressed leakage currents while achieving an impedance bandwidth of 113.3% and an axial ratio bandwidth of 98.1%. Targeting the requirements of modern Wi-Fi and 5G indoor base stations, a low-profile, wideband dual-polarized dipole antenna was proposed in [8]. By employing a Particle Swarm Optimization (PSO) algorithm for the balun design, the structure achieved an ultra-low profile of 0.14λ, while its 4-element array configuration delivered a peak gain of 14.2 dBi without the need for a complex feeding network. To achieve a low-profile dual-band operation with circular polarization, a crossed asymmetric dipole antenna backed by an artificial magnetic conductor (AMC) was proposed in [9]. By incorporating T-shaped slits into the AMC unit cells, the structure effectively tuned its dual

resonances, yielding broadband impedance and axial-ratio performance across both the 2.4 GHz and 5 GHz bands.

Furthermore, to achieve high-gain directional CP radiation, reflector-backed configurations have been extensively explored in the literature. For instance, a wideband CP cross-dipole antenna placed above a square reflector was presented in [10], where a center-fed structure with curved-delay lines enabled symmetric radiation patterns and a peak gain of 6.8 dBic, confirming the effectiveness of reflector integration for gain enhancement. Similarly, the integration of a Perfect Electric Conductor (PEC) reflector has been successfully employed to enhance boresight gain by combining forward-radiated and reflected electromagnetic waves. In [11], a compact super-wideband antenna utilizing a full-PEC reflector demonstrated a significant gain improvement of 3–6.5 dBi, underscoring the efficacy of reflector-backed structures in achieving high-gain directional radiation performance. In addition, multi-band performance and gain enhancement have been effectively addressed through advanced hybrid reflector surfaces. A recent study presented a triple-band antenna integrating both AMC and PEC characteristics to achieve low-profile unidirectional radiation in lower bands and enhanced gain in the upper band [12]. By successfully combining these surface properties, the design achieved peak gains of up to 9.6 dBi across multiple Wi-Fi and 5G operating bands, further confirming the potential of reflector-based structures for future multiband communication base stations.

Machine learning (ML) has recently gained significant attention in antenna engineering as a powerful tool for discovering optimized solutions within complex parameter spaces [13]. As highlighted in [13], ML techniques represent a paradigm shift in design methodology, offering a clear advantage over conventional trial-and-error simulation methods by providing rapid and accurate performance predictions. This study builds upon these foundational concepts, focusing on the integration of ML algorithms to overcome the computational bottlenecks typically associated with traditional full-wave antenna design processes. Beyond the foundational concepts, recent literature highlights the integration of Artificial Intelligence (AI) and deep learning algorithms with electromagnetic simulation tools, such as CST Microwave Studio and HFSS, to automate the design and optimization lifecycle [14]. These approaches, particularly surrogate-based optimization, have been proven effective in reducing the number of required full-wave simulations, thereby significantly enhancing computational efficiency and accelerating the overall design process [14]. Despite these advancements, conventional antenna design methodologies remain exhaustive and often fail to guarantee optimal outcomes, particularly given the growing topological complexity and stringent performance requirements of modern antennas [15]. Recent literature increasingly identifies that the efficiency and optimization capability of available methods are severely challenged by these complex design spaces. Consequently, there is a paradigm shift toward machine learning-based

optimization techniques, which are specifically designed to address these challenges by providing more efficient and robust design alternatives compared to traditional iterative approaches [15].

In this paper, a compact, reflector-backed dual-band microstrip antenna is presented to address these requirements. The radiating element is based on a modified cross-dipole configuration to achieve resonance at 2.45 GHz and 5.2 GHz. To enhance its performance, a metallic reflector is integrated into the design, significantly boosting its directional gain and front-to-back ratio.

Furthermore, the traditional antenna design process often relies on iterative, time-consuming, and computationally expensive full-wave 3D electromagnetic simulations. To overcome this computational bottleneck, this work also proposes and validates a novel approach by integrating machine learning (ML) algorithms as a rapid and accurate surrogate modeling technique [13], [14]. Three different algorithms—Random Forest (RF), Support Vector Regression (SVR), and Gradient Boosting Regressor (GBR)—are trained to predict the antenna's reflection coefficient (S11) based on its geometrical parameters, thereby demonstrating a reliable path towards accelerating the antenna optimization process.

MATERIALS AND METHOD

A. Antenna Design

The proposed antenna is designed to operate at dual Wi-Fi frequency bands, specifically targeting 2.45 GHz and 5.2 GHz. The physical layout and geometrical configuration of the antenna are illustrated in Figure 1. The antenna is printed on a low-cost FR-4 dielectric substrate with overall dimensions of 50 mm x 50 mm and a thickness of 1.6 mm.

To achieve dual-band resonance, a modified cross-dipole configuration is utilized. The radiating element consists of two distinct sets of arms, each responsible for a specific frequency band. The longer, arrow-shaped dipole arms are designed to resonate at the lower frequency band. The electrical length of these arrow-shaped arms is approximately equal to a quarter-wavelength ($\lambda_L/4$) at 2.45 GHz. Conversely, the inner sickle-shaped arms are tailored for the higher frequency band, with their lengths corresponding to a quarter-wavelength ($\lambda_H/4$) at 5.2 GHz. The antenna is excited centrally via a coaxial probe, which simultaneously feeds both the 2.45 GHz and 5.2 GHz radiating arms. All detailed parameterized dimensions of the radiating structure are listed in Table 1.

To enhance the directional gain and radiation performance of the antenna, a metallic reflector is integrated into the design. A solid aluminum plate with a thickness of 1 mm is positioned parallel to the FR-4 substrate. The reflector prevents back-radiation and redirects the electromagnetic waves in the forward direction. To ensure constructive interference and maximize the broadside gain, the separation distance between the radiating substrate and the

aluminum reflector is optimally set to a quarter-wavelength ($\lambda_L/4$) of the 2.45 GHz operating frequency.

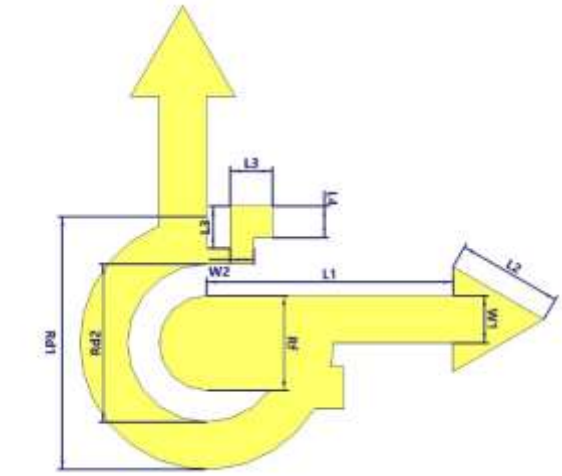

(a) (b)

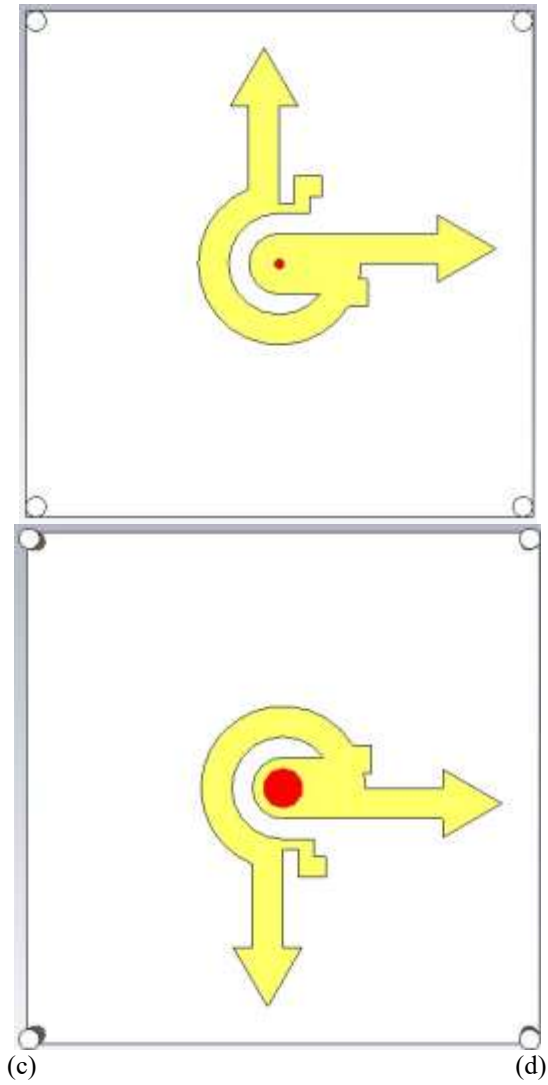

(c) (d)

Fig. 1 Proposed antenna (a) detailed geometry, (b) 3D view, (c) front view and (d) back view.

Table 1. Dimensions of the proposed antenna.

Parameter	Dimensions (mm)
Rf	6
Rd1	16
L1	15.58
L2	6.64
W1	3
W2	1.5
L3	2.67
L4	2
Rd2	10
HR	21

II. RESULTS

To evaluate the performance of the proposed dual-band Wi-Fi antenna, numerical simulations were carried out. The key performance parameters, including the reflection coefficient (S_{11}) and far-field radiation characteristics, were analyzed.

Figure 2 illustrates the simulated reflection coefficient (S_{11}) of the proposed antenna across the 2 GHz to 6 GHz frequency spectrum. The antenna exhibits a distinct dual-band resonance behavior. For the lower frequency band, the -10 dB impedance bandwidth ranges from 2.404 GHz to 2.676 GHz, covering the entire standard 2.4 GHz WLAN/Wi-Fi band perfectly. For the upper frequency band, the -10 dB bandwidth extends from 5.046 GHz to 5.294 GHz, which successfully covers the lower 5 GHz Wi-Fi spectrum. The deep resonance dips in both bands indicate excellent impedance matching between the 50 Ω coaxial feed and the antenna structure.

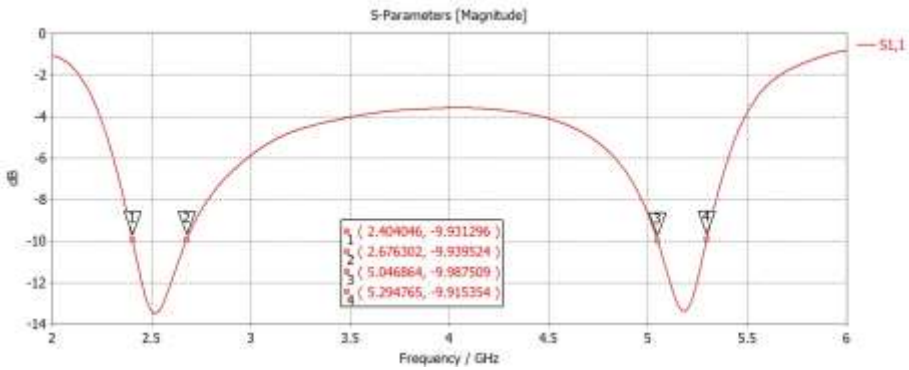

Fig. 2 S11 results.

The far-field radiation patterns and realized gain of the antenna at the center frequencies of the two operating bands are evaluated. Due to the integration of the aluminum reflector at the back of the FR-4 substrate, the antenna successfully produces directional broadside radiation patterns.

Figure 3 shows the 1D polar radiation pattern at 2.45 GHz. The antenna achieves a maximum realized gain of 5.8 dBi at $\theta = 0°$. The Half-Power Beamwidth, or angular width (3 dB), is observed to be 73.5 ° with a sufficiently low side lobe level of -3.4 dB. The optimum quarter-wavelength distance ($\lambda_L/4$) of the reflector at 2.45 GHz significantly contributes to this high broadside gain.

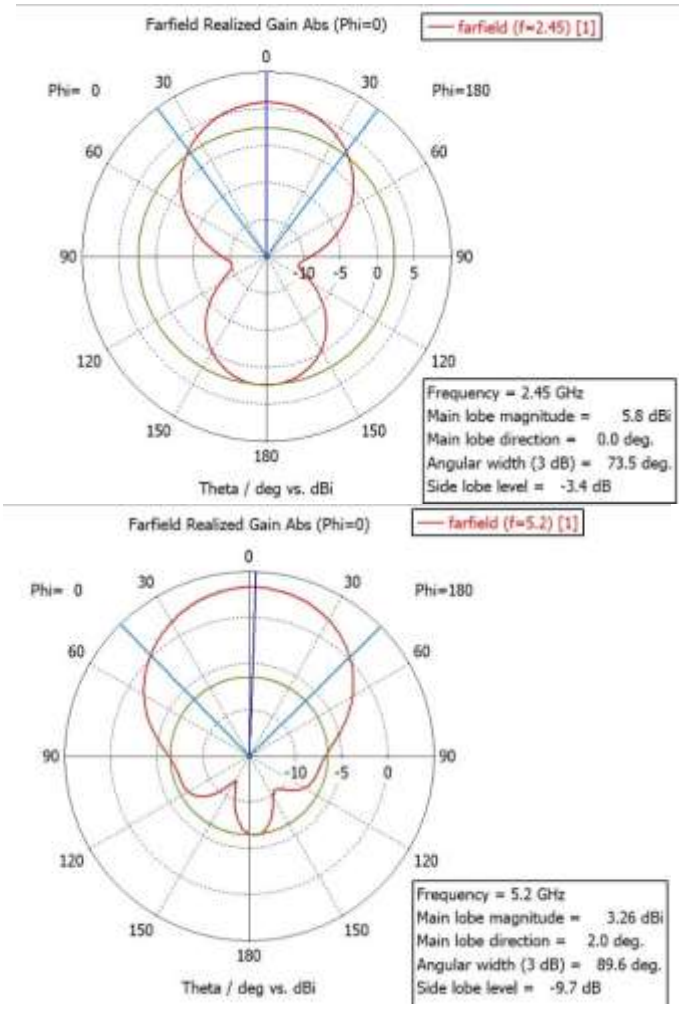

Fig. 3 2.45 GHz and 5.2 GHz radiation pattern of the proposed antenna.

Figure 3 depicts the radiation pattern at 5.2 GHz. At this higher band, the maximum realized gain is recorded as 3.26 dBi with an angular width of 89.6° and a very low side lobe level of -9.7 dB. The slight decrease in peak gain at 5.2 GHz compared to the 2.45 GHz band can be attributed to two main factors: firstly, the inherent dielectric losses of the FR-4 substrate, which increase at higher frequencies; and secondly, the reflector distance, which was optimized for the 2.45 GHz wavelength, behaves electrically larger at 5.2 GHz, thereby slightly altering the optimal constructive interference condition. Nevertheless, the gain and directional characteristics remain highly suitable for indoor Wi-Fi applications.

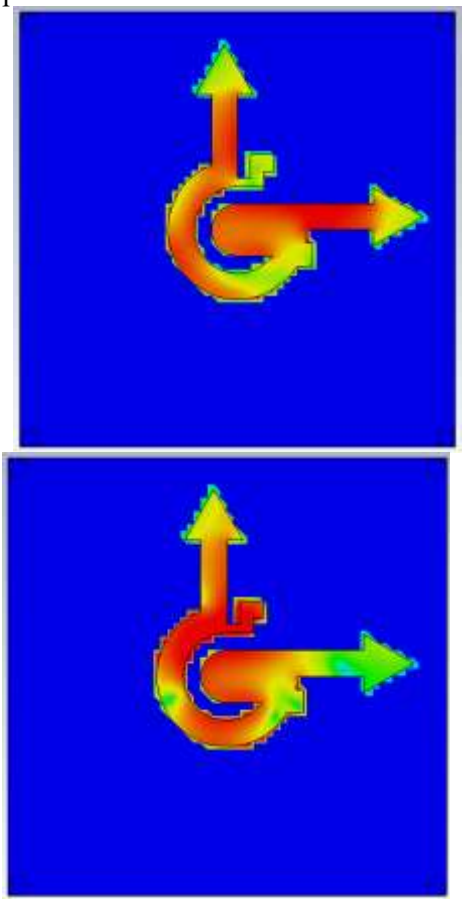

(a) (b)

Fig. 4 Simulated surface current distribution of the proposed antenna: (a) at 2.45 GHz and (b) at 5.2 GHz.

To gain a deeper physical insight into the frequency-selective resonance mechanism of the proposed dual-band antenna, the simulated surface current distributions at 2.45 GHz and 5.2 GHz are analyzed, as illustrated in Figure 4. The current density maps clearly reveal the frequency-dependent behavior of

the radiating structure. At 2.45 GHz (Figure 4a), the current is predominantly concentrated along the longer, arrow-shaped dipole arms, confirming their role as the primary radiators for the lower frequency band. Conversely, at 5.2 GHz (Figure 4b), the current intensity shifts toward the inner, sickle-shaped arms. This distinct shift in current distribution validates the dual-band design strategy, where the antenna structure effectively segregates the resonant paths for each frequency band. The intense current flow along these respective arms at their targeted frequencies confirms that the input energy is efficiently guided into the appropriate radiating segments, ensuring optimal impedance matching and radiation performance for both the 2.45 GHz and 5.2 GHz Wi-Fi standards.

III. DISCUSSION

To explicitly demonstrate the contribution of the metallic reflector to the antenna's radiation performance, a comparative gain analysis was conducted. Figure 4 presents the simulated gain over frequency for both the reflector-backed configuration (red curve, $a = 25$ mm) and the configuration without a functional reflector (green curve, $a = 1$ mm).

As observed in the graph, the integration of the reflector positioned at the optimized distance significantly enhances the antenna gain across the entire operating spectrum. At the lower target frequency of 2.45 GHz, the antenna gain increases drastically from a mere 1.61 dBi to 6.08 dBi, yielding an impressive improvement of approximately 4.47 dB. Similarly, at the upper frequency band of 5.2 GHz, the presence of the reflector boosts the gain from 0.44 dBi to 3.47 dBi. This substantial enhancement confirms that the reflector efficiently blocks back-radiation and constructively redirects the electromagnetic waves in the broadside direction, effectively validating the $\lambda_L/4$ spacing design principle discussed in the methodology.

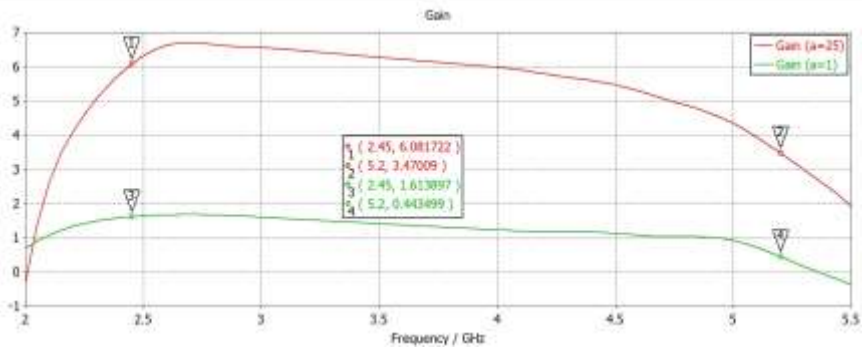

Fig. 4 Gain comparison of the proposed antenna with and without the reflector.

To overcome the high computational cost and time consumption associated with full-wave 3D electromagnetic simulations, three different Machine Learning (ML) algorithms were deployed to predict the reflection coefficient

(S_{11}) of the proposed antenna. The predictive models include Random Forest (RF), Support Vector Regression (SVR), and Gradient Boosting Regressor (GBR). The models were trained using the operating frequency and the lengths of the inner and outer dipole arms ($qw2$ and $qw5$) as input features. To rigorously evaluate the generalization capability of the algorithms, an interpolation test was conducted. Two completely unseen geometrical combinations (Scenario 1: $qw2 = 15.0, qw5 = 18.0$ and Scenario 2: $qw2 = 17.0, qw5 = 8.0$) were strictly isolated as the test set, while the remaining dataset was used for training.

Figure 5 illustrates the comparison between the actual S_{11} values obtained from CST simulations and the predicted values by the ML models for the two test scenarios. Visually, the tree-based ensemble algorithms (Random Forest and Gradient Boosting) demonstrate a superior ability to track the highly non-linear electromagnetic behavior of the antenna compared to SVR. Specifically, in Test Scenario 2, the actual antenna exhibits a deep resonance null of approximately -22 dB around 3.1 GHz. While the Random Forest algorithm captures this sharp resonance dip with remarkable precision, the SVR model severely underestimates the depth (flattening around -12 dB) due to its inherent margin-based smoothing (epsilon-tube) characteristics.

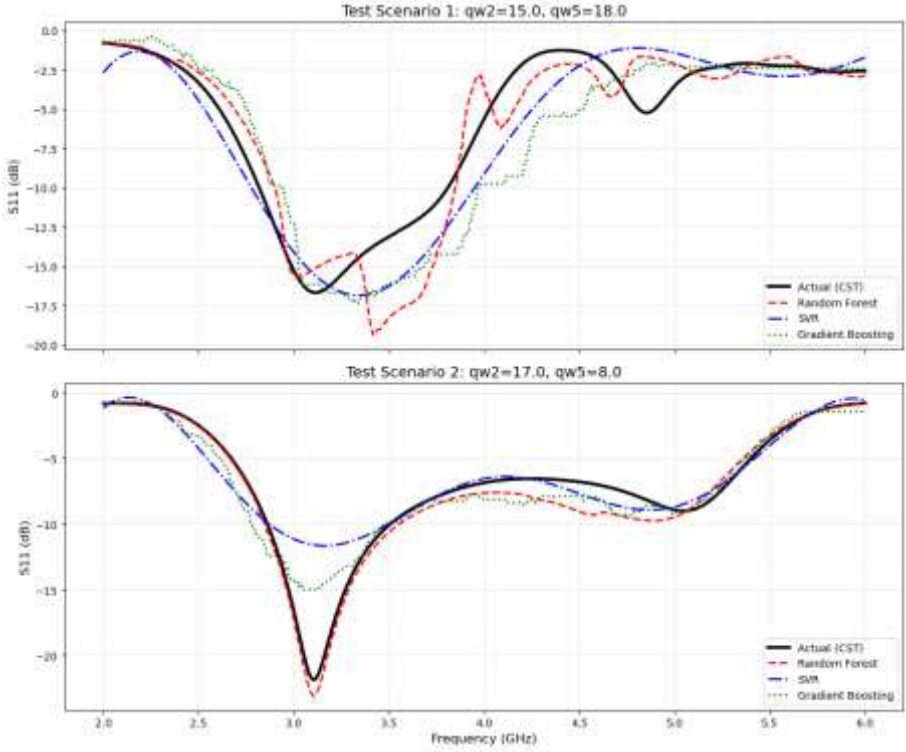

Fig. 5 Gain comparison of the proposed antenna with and without the reflector.

The quantitative performance of the implemented algorithms is summarized in Table 2. The performance metrics, including the Coefficient of Determination (R^2), Mean Absolute Error (MAE), and Root Mean Squared Error (RMSE), confirm the visual observations. Random Forest achieved the highest prediction accuracy, making it a highly reliable surrogate model for rapid antenna dimension optimization without requiring repetitive electromagnetic simulations.

Table 2. Performance metrics of the utilized machine learning algorithms.

Algorithm	R^2	MAE (dB)	RMSE (dB)
Random Forest	0.8963	1.0558	1.5733
SVR	0.8124	1.3506	2.1159
Gradient Boosting	0.7954	1.5160	2.2100

IV. CONCLUSION

In this work, a compact, reflector-backed dual-band antenna was designed, and its performance was successfully predicted using machine learning methodologies. The proposed antenna, based on a modified cross-dipole configuration on an FR-4 substrate, demonstrated excellent operational characteristics for modern Wi-Fi systems. Simulation results confirmed its dual-band capability with a -10 dB impedance bandwidth spanning from 2.404 GHz to 2.676 GHz for the lower band, and from 5.046 GHz to 5.294 GHz for the upper band, fully covering the targeted WLAN frequencies. The strategic integration of a metallic reflector at a quarter-wavelength distance was instrumental in achieving high directionality, resulting in a peak realized gain of 5.8 dBi at 2.45 GHz and 3.26 dBi at 5.2 GHz. The comparative analysis explicitly quantified the reflector's contribution, which boosted the gain by a substantial 4.47 dB at 2.45 GHz compared to the antenna without a reflector. Furthermore, this study validated the use of machine learning as a highly effective surrogate modeling technique for accelerating the antenna design process. A comparative analysis of three algorithms—Random Forest (RF), Support Vector Regression (SVR), and Gradient Boosting Regressor (GBR)—was conducted. The Random Forest model demonstrated superior performance in predicting the antenna's complex S-parameter behavior, achieving the highest Coefficient of Determination (R^2) of 0.8963, the lowest Mean Absolute Error (MAE) of 1.0558 dB, and the lowest Root Mean Squared Error (RMSE) of 1.5733 dB. The proposed high-gain antenna, combined with the successfully implemented RF prediction model, presents a robust and computationally efficient solution for the design and optimization of modern wireless communication antennas. Future work will involve the fabrication

and experimental measurement of the antenna prototype to verify these promising simulation and prediction results.

REFERENCES

[1] A. Al-Fuqaha, M. Guizani, M. Mohammadi, M. Aledhari, and M. Ayyash, "Internet of Things: A Survey on Enabling Technologies, Protocols, and Applications," *IEEE Communications Surveys & Tutorials*, vol. 17, no. 4, pp. 2347-2376, 2015.

[2] E. Khorov, I. Levitsky, and I. F. Akyildiz, "Current Status and Directions of IEEE 802.11be, the Future Wi-Fi 7," *IEEE Access*, vol. 8, pp. 88664-88688, 2020.

[3] J. Li, X. Jiang, and C. Zhang, "A Compact Dual-Band Printed Antenna for Wi-Fi/WLAN Applications," *IEEE Antennas and Wireless Propagation Letters*, vol. 21, no. 5, pp. 1023-1027, 2022.

[4] S. X. Ta, I. Park, and R. W. Ziolkowski, "Crossed Dipole Antennas: A review," *IEEE Antennas and Propagation Magazine*, vol. 57, no. 5, pp. 107-122, Oct. 2015.

[5] Fan, J., Lin, J., Cai, J., & Qin, F. (2022). Ultra-wideband circularly polarized cavity-backed crossed-dipole antenna. *Scientific reports*, *12*(1), 4569.

[6] Yang, W. J., Pan, Y. M., & Zheng, S. Y. (2022). Mutual coupling reduction in CP MIMO crossed-dipole antenna array. *IEEE Antennas and Wireless Propagation Letters*, *21*(12), 2442-2446.

[7] Wang, H., Park, Y. B., & Park, I. (2024). Design of a broadband circularly polarised uniplanar crossed-dipole antenna. *Scientific Reports*, *14*(1), 7821.

[8] Teng, X., Hou, Y., Guo, C., Wang, S., & Ma, K. (2024). Broadband low-profile multifunction dual-polarized dipole antenna and array for 5G and WiFi application. *IEEE Antennas and Wireless Propagation Letters*, *23*(6), 1849-1853.

[9] Ta, S. X., & Park, I. (2014). Dual-band low-profile crossed asymmetric dipole antenna on dual-band AMC surface. *IEEE Antennas and Wireless Propagation Letters*, *13*, 587-590.

[10] He, Y., He, W., & Wong, H. (2014). A wideband circularly polarized cross-dipole antenna. *IEEE Antennas and Wireless Propagation Letters*, *13*, 67-70.

[11] Belazzoug, M., Khodja, K., Ksouri, E., Rebbah, R., Messaoudene, I., Chaouche, Y. B., ... & Denidni, T. A. (2021, October). Design of a Compact SWB High Gain Antenna Using a Fully PEC Reflector. In *2021 IEEE Microwave Theory and Techniques in Wireless Communications (MTTW)* (pp. 253-257). IEEE.

[12] Hu, T., Pan, Z., Saitou, M., Liu, J., & Shimamoto, S. (2020). A Triple-Band Antenna Loaded with Reflector Surface for WLAN and 5G Applications. *J. Commun.*, *15*(10), 729-734.

[13] El Misilmani, H. M., & Naous, T. (2019, July). Machine learning in antenna design: An overview on machine learning concept and algorithms. In *2019 International Conference on High Performance Computing & Simulation (HPCS)* (pp. 600-607). IEEE.

[14] Sarker, N., Podder, P., Mondal, M. R. H., Shafin, S. S., & Kamruzzaman, J. (2023). Applications of machine learning and deep learning in antenna design, optimization, and selection: A review. *IEEE Access*, *11*, 103890-103915.
[15] Akinsolu, M. O., Mistry, K. K., Liu, B., Lazaridis, P. I., & Excell, P. (2020, March). Machine learning-assisted antenna design optimization: A review and the state-of-the-art. In *2020 14th European conference on antennas and propagation (EuCAP)* (pp. 1-5). IEEE.
[16] H. M. El Misilmani and T. Naous, "Machine Learning in Antenna Design: An Overview on Machine Learning Concept and Algorithms," in *International Conference on High Performance Computing & Simulation (HPCS)*, pp. 600-607, 2019.
[17] R. Sharma and P. Kumar, "Machine Learning Techniques for Antenna Design and Optimization: A Comprehensive Survey," *IEEE Access*, vol. 10, pp. 45678-45690, 2022.

Thermoelectric Generators for Automotive Waste Heat Recovery: Modelling, Power Conditioning and System Design

Volkan AKDOĞAN[1]

Yuying YAN[2]

1- Dr.; Iskenderun Technical University Engineering and National Sciences Faculty. volkan.akdogan@iste.edu.tr ORCID No: 0000-0003-2219-2317
2- Prof. Dr.; University of Nottingham Faculty of Engineering. yuying.yan@nottingham.ac.uk ORCID No: 0000-0001-8603-4372

ABSTRACT

With rising global energy demands and stringent environmental regulations, recovering the 30-40% of energy lost as exhaust heat in internal combustion engines is essential. This study aims to provide a comprehensive analysis of thermoelectric generators (TEGs) for automotive waste heat recovery, encompassing thermal modeling, power conditioning, and system design. The primary challenge is the dynamic, fluctuating nature of exhaust temperatures, which complicates efficient power extraction and exacerbates the inherently low conversion efficiency of TEGs. The novelty of this work lies in developing a two-dimensional transient heat transfer model featuring temperature-dependent material properties, providing a more accurate prediction of dynamic thermal behavior than traditional one-dimensional models. The methodology integrates this 2D numerical simulation with an H-bridge DC-DC converter and a Perturb and Observe (P&O) Maximum Power Point Tracking (MPPT) algorithm to dynamically optimize load resistance. The research frame utilizes a custom experimental TEG prototype equipped with controlled heat sources and liquid cooling, continuously acquiring voltage, current, and temperature data under simulated automotive conditions. The experimental data supported the trends predicted by the integrated model, suggesting that dynamic power conditioning is a practical approach to maintaining efficiency under variable thermal conditions. Ultimately, this study highlights that while integrated thermal and electrical management offers a practical pathway to optimize performance, further research into cost-effective materials and scalable manufacturing remains necessary for the widespread commercialization of these systems.

Keywords – Thermoelectric Generators, Waste Heat Recovery, Thermal Modeling, Power Conditioning, Maximum Power Point Tracking

INTRODUCTION

Rising global energy needs, dwindling fossil fuel reserves, and stringent environmental laws have greatly accelerated the exploration of energy efficiency and waste heat recovery technologies. In traditional internal combustion engines, a significant portion of the fuel's energy is lost as heat through exhaust gases and cooling systems. Research indicates that approximately 30-40% of the energy produced during combustion is lost via the exhaust system, presenting a considerable opportunity for energy recovery [1-3]. By capturing the heat that currently escapes and converting it into electricity, the engine can consume less fuel, emit fewer pollutants, and operate more efficiently.

Thermoelectric generators (TEGs) have gained recognition as an effective solution for capturing waste heat due to their solid-state design, reliability, and absence of moving mechanical components. These thermoelectric devices convert temperature differences directly into electrical energy through the Seebeck effect. A typical thermoelectric module is composed of pairs of p-type and n-type semiconductor pellets, which are electrically connected in series and thermally connected in parallel. The pellets are enclosed between two ceramic plates that secure the structure. A temperature gradient is established between the module's hot and cold surfaces, causing charge carriers to move from the warmer side to the cooler side. This movement generates an electrical potential difference across the device's terminals [4, 5].

Heat recovery systems, which utilize waste heat that would otherwise be lost, are particularly appealing due to their low energy conversion efficiency. Thermoelectric generators (TEGs) generally achieve about 5% efficiency in converting heat into electricity. As a result, TEGs have been extensively studied for a range of applications, including recovering heat from automotive exhaust, utilizing industrial waste heat, powering space systems, and integrating renewable energy sources [6-9]. In the automotive industry, several prototype systems have shown the potential to harness exhaust heat for generating electrical power. For instance, experimental TEG systems installed in vehicles have reported power outputs of several hundred watts under realistic driving conditions [10-12]. These systems can significantly decrease the electrical demand on the alternator, thereby enhancing fuel efficiency.

The effectiveness of thermoelectric systems is heavily influenced by the properties of the materials used, the design of the device, and how heat is managed. Materials that vary with temperature integrate electrical conductivity, thermal conductivity, and the Seebeck coefficient to assess their efficiency level, known as the figure of merit (ZT). Bismuth telluride (Bi2Te3) based materials are commonly employed in thermoelectric generators functioning at moderate temperatures because of their relatively high figure of merit and advantageous thermoelectric characteristics [13-15]. Nonetheless, the pursuit of advanced thermoelectric materials with enhanced efficiency continues to be a vibrant area of research.

Beyond material advancements, precise modeling and optimization of thermoelectric systems are crucial for enhancing power generation and system efficiency. Thermoelectric generators function under highly variable conditions, especially in automotive settings where exhaust temperatures and operational loads fluctuate continuously throughout driving cycles. Consequently, integrated thermal and electrical simulations are necessary to accurately forecast system performance and design the most effective configurations [16-19].

Efficient extraction of electrical power is another vital component of thermoelectric power generation systems. The electrical properties of thermoelectric generators fluctuate with changes in temperature and load conditions, necessitating the use of power conditioning circuits and maximum power point tracking (MPPT) techniques to achieve optimal energy conversion. By integrating DC-DC power converters with MPPT algorithms, thermoelectric generators can consistently operate at their maximum power point despite varying thermal conditions, thereby greatly enhancing the overall efficiency of the system [20-23].

This study offers a summary of thermoelectric power generation aimed at recovering waste heat in automotive applications. It covers the basic principles of converting thermoelectric energy, the properties of thermoelectric materials, thermal modeling techniques, and methods for power conditioning. Additionally, it introduces system-level aspects such as the design of thermoelectric generators, simulation techniques, and strategies for optimizing power, providing a thorough understanding of thermoelectric energy harvesting systems.

FUNDAMENTALS OF THERMOELECTRIC ENERGY CONVERSION

Thermoelectric Energy Conversion Principle

Thermoelectric energy conversion relies on the direct conversion of heat into electricity using solid-state semiconductor materials. This process takes place when there is a temperature gradient across conductive materials, resulting in the creation of an electrical potential difference. Thermoelectric generators (TEGs) exploit this effect to capture thermal energy and transform it into electrical power without the need for any moving mechanical components. Thanks to their solid-state design, thermoelectric systems provide benefits such as high reliability, minimal maintenance needs, and

compactness, making them ideal for a range of energy harvesting applications, including recovering waste heat from vehicles, industrial processes, and building energy systems [1, 3, 12].

Standard thermoelectric modules are composed of several p-type and n-type semiconductor components that are electrically linked in series and thermally aligned in parallel. When a temperature difference is established between the module's hot and cold sides, charge carriers in the semiconductor materials migrate from the hot side to the cold side. This movement of carriers generates an electric potential difference across the module's terminals. Once the module is connected to an external load, the resulting voltage propels an electrical current through the circuit, thereby generating useful electrical power [4, 6].

The process of converting thermoelectric energy is primarily influenced by three key phenomena: the Thomson effect, the Seebeck effect, and the Peltier effect. These phenomena explain the interaction between heat transfer and electrical conduction in thermoelectric materials, serving as the foundational principles for technologies related to thermoelectric power generation and cooling [8, 9].

Seebeck Effect

The Seebeck effect is the core principle behind the generation of electrical power in thermoelectric devices. This phenomenon was initially discovered by Thomas Johann Seebeck in 1821 when he noticed that a voltage was produced in a closed circuit made of two distinct conductors with junctions kept at varying temperatures. The voltage produced is directly related to the temperature difference between the hot and cold junctions [4, 24].

The open-circuit voltage generated by a thermoelectric material due to the Seebeck effect can be expressed as [25]

$$V = S(T_h - T_c) \tag{1}$$

where S represents the Seebeck coefficient of the material, while Th and Tc denote the temperatures of the hot and cold sides, respectively. The Seebeck coefficient indicates the magnitude of voltage generated per unit temperature difference and depends on the material properties of the thermoelectric elements. Semiconductor materials generally exhibit higher

Seebeck coefficients than metals, which makes them more suitable for thermoelectric power generation applications [13, 14].

In thermoelectric generators, the combination of p-type and n-type semiconductor materials is used to boost voltage output. The amount of electrical power produced is significantly influenced by the temperature gradient across the module and the electrical load conditions. Therefore, it is essential to maintain a substantial temperature difference between the two sides to optimize the performance of thermoelectric generators, particularly in waste heat recovery applications like automotive exhaust systems [6, 7].

Peltier Effect

The Peltier effect is the inverse of the thermoelectric phenomenon, describing the process of heat being absorbed or emitted at the junction of two distinct conductors when an electric current passes through the circuit. This effect, discovered by Jean Charles Athanase Peltier in 1834, serves as the foundational principle for thermoelectric cooling systems [26].

The rate of heat transfer associated with the Peltier effect can be expressed as [27]

$$\dot{Q} = \Pi I \tag{2}$$

where $\dot{Q}$ denotes the heat transfer rate, Π is the Peltier coefficient, and I represents the electrical current. Depending on the direction of current flow, heat can either be absorbed at one junction and released at the other or vice versa. Although the Peltier effect is mainly utilized in thermoelectric cooling devices, it also influences heat flow inside thermoelectric generators and contributes to the overall thermal balance of the system [8, 9].

Thomson Effect

The Thomson effect refers to the process of heat being absorbed or produced within a conductor when an electrical current flows through it and a temperature difference exists along the material. Discovered by William Thomson, also known as Lord Kelvin, this effect is recognized as the third essential thermoelectric phenomenon [28].

The heat generation associated with the Thomson effect can be expressed as [29]

$$\dot{Q} = \tau \mathrm{I} \frac{dT}{dx} \tag{3}$$

where τ is the Thomson coefficient, I is the electric current, and dT/dx represents the temperature gradient along the material. Compared to the Seebeck and Peltier effects, the Thomson effect generally has a smaller magnitude; however, it plays a role in the internal thermal behaviour of thermoelectric devices and should be considered in detailed thermoelectric modelling and analysis [4].

Thermoelectric Materials and Figure of Merit

The effectiveness of thermoelectric devices is heavily influenced by the thermoelectric characteristics of the materials incorporated into the modules. The dimensionless figure of merit (ZT) is a standard metric used to assess the efficiency potential of thermoelectric materials. This parameter is defined as [30]

$$ZT = \frac{S^2 \sigma T}{\kappa} \tag{4}$$

where S represents the Seebeck coefficient, σis the electrical conductivity, T is the absolute temperature, and κ is the thermal conductivity of the material. High ZT values are indicative of better thermoelectric performance, since they are caused by a combination of high electrical conductivity, low thermal conductivity, and high Seebeck coefficient [9, 14].

Among the thermoelectric materials available, bismuth telluride (Bi2Te3) and its alloys are commonly utilized in thermoelectric generators operating at moderate temperatures due to their relatively high efficiency and advantageous material characteristics. Several other materials, such as lead telluride (PbTe), silicon germanium (SiGe), and half Heusler compounds, are being explored for applications that demand enhanced thermal stability [13, 15]. Ongoing research in material science and nanostructuring techniques seeks to further enhance thermoelectric efficiency and broaden the practical application of thermoelectric generators in energy harvesting systems [9].

THERMOELECTRIC GENERATOR SYSTEM ARCHITECTURE

Structure of a Thermoelectric Generator

A thermoelectric generator (TEG) is a device that transforms heat energy directly into electrical energy through thermoelectric effects. Typically, a thermoelectric generator is composed of several thermoelectric modules that are both electrically and thermally connected to harness heat

from a temperature difference. Each thermoelectric module is flanked by two ceramic plates, which contain p-type and n-type semiconductor elements that are electrically linked in series and thermally linked in parallel.

The module's hot side is positioned against a heat source, like an automotive exhaust pipe, while the cold side is kept cooler through a cooling system. When there is a temperature difference between these surfaces, charge carriers in the semiconductor legs move due to thermal energy. An electrical potential difference arises across the module's terminals as electrons in the n-type material move toward the cooler side and holes in the p-type material move toward the warmer side.

In practical applications of thermoelectric generator systems, numerous thermoelectric couples are combined within a module to enhance the voltage output. These modules can be linked in either series or parallel arrangements, depending on the system's required voltage and current specifications. This modular design enables thermoelectric generators to be adapted for various power levels and uses.

Electrical Equivalent Model of a Thermoelectric Generator

In terms of electrical representation, a thermoelectric generator can be depicted by a simplified equivalent circuit that includes a voltage source and an internal resistance. The voltage source is associated with the thermoelectric voltage produced due to the temperature difference between the hot and cold sides, while the internal resistance signifies the electrical resistance of the thermoelectric components.

The open circuit voltage generated by the thermoelectric module can be expressed as [25]

$$V_{oc} = S(T_h - T_c) \tag{5}$$

where S is the effective Seebeck coefficient of the thermoelectric module, Th is the hot side temperature, and Tc is the cold side temperature. When the module is connected to an external electrical load, the output current depends on both the internal resistance of the thermoelectric module and the load resistance.

The electrical output power delivered to the load can be expressed as

$$P = I^2 R_L \tag{6}$$

where RL is the load resistance and I is the output current. A thermoelectric generator's internal resistance equals its load resistance when

maximum power is transferred. Therefore, impedance matching between the generator and the electrical load is essential for achieving maximum power extraction from the system.

Thermal Energy Flow in Thermoelectric Modules

The efficiency of a thermoelectric generator is heavily dependent on the flow of thermal energy through the thermoelectric module. Heat is absorbed by the module's hot side from the heat source, where a portion is transformed into electrical energy, while the rest is conducted to the cold side via thermal conduction and thermoelectric heat transport processes.

The total heat flow within a thermoelectric element consists of three primary components:

• Seebeck heat conversion, which produces electrical power

• Joule heating, caused by electrical resistance within the thermoelectric material

• Fourier heat conduction, which transfers heat from the hot side to the cold side

The thermal behavior of the thermoelectric module and its electrical power output are collectively determined by these mechanisms. As a result, effective thermal management is essential in the design of thermoelectric generators, especially in applications like automotive waste heat recovery, where temperature conditions fluctuate during operation.

Load Matching and Power Extraction

In real-world thermoelectric generator systems, the electrical output characteristics fluctuate with changes in temperature and load conditions. Because the internal resistance of the thermoelectric generator varies with temperature, it is necessary to continuously adjust the generator's operating point to ensure optimal power extraction.

As a result, thermoelectric energy harvesting systems often incorporate power conditioning circuits and control strategies. By using DC-DC converters along with maximum power point tracking (MPPT) algorithms, the electrical load on the thermoelectric generator can be dynamically modified. This ensures that the generator functions near its peak power point, even when temperature conditions fluctuate.

This architectural framework at the system level facilitates the efficient harnessing of energy from thermoelectric generators in variable settings like automotive exhaust systems, where the temperature of the heat source varies during engine operation. By integrating thermoelectric modules, thermal management systems, and power conditioning electronics, a comprehensive thermoelectric generator system can successfully transform waste heat into valuable electrical energy.

THERMAL MODELLING OF THERMOELECTRIC MODULES

Heat Transfer Mechanisms in Thermoelectric Modules

Thermal modeling is essential in designing and analyzing the performance of thermoelectric generators, as the electrical output of these devices is directly influenced by the temperature difference across their elements. Within a thermoelectric module, heat is transferred through various interconnected physical processes, including thermoelectric conversion, heat conduction, and resistive heating. To accurately predict the temperature distribution and electrical performance of the generator, precise modeling of these processes is crucial.

A thermoelectric module is generally composed of several p-type and n-type semiconductor legs situated between two ceramic layers. The module's hot side is exposed to a heat source, while the cold side is linked to a cooling system. Heat that enters the hot side travels through the thermoelectric components toward the cold side, where a portion of this thermal energy is transformed into electrical energy via the Seebeck effect. The rest of the heat is conveyed through the module due to thermal conduction and internal heat generation processes.

The overall heat flow in a thermoelectric component can be explained by three main factors: the movement of heat due to the Peltier effect, the transfer of heat through conduction as described by Fourier’s law, and the generation of heat from resistance, known as Joule heating, within the thermoelectric material.

One Dimensional Thermal Model

In many thermoelectric analyses, a simplified one dimensional thermal model is used to represent heat transfer along the length of the thermoelectric

legs. Under steady state conditions, heat conduction within a thermoelectric element can be expressed using Fourier's law [31]

$$Q = -kA\frac{dT}{dx} \tag{7}$$

where Q represents the heat transfer rate, k is the thermal conductivity of the thermoelectric material, A is the cross sectional area of the thermoelectric leg, and dT/dx is the temperature gradient along the element.

However, the thermal behaviour of thermoelectric modules is also affected by electrical current flowing through the device. The presence of electrical current results in Joule heating within the thermoelectric material, which can be expressed as

$$Q_J = I^2R \tag{8}$$

where I is the electrical current and R is the internal resistance of the thermoelectric element. These heat generation and conduction processes together determine the temperature distribution along the thermoelectric legs.

While one-dimensional models offer valuable insights into the behavior of thermoelectric devices, they might not accurately reflect the temperature fluctuations that occur in real-world systems where heat transfer conditions change both spatially and over time.

Two Dimensional Transient Heat Transfer Model

In real-world applications of thermoelectric generators, such as systems for recovering waste heat in vehicles, the thermal conditions of the heat source fluctuate continuously with changes in operating conditions. Consequently, transient thermal modeling is essential for accurately forecasting the dynamic performance of thermoelectric modules.

The thesis introduces a two-dimensional transient heat transfer model for a thermoelectric couple, utilizing a thermoelectric modeling approach. This model incorporates temperature-dependent material properties and varying ambient temperature conditions into the heat transfer equations to enhance the precision of the simulation outcomes.

The transient heat conduction within the thermoelectric element can be described using the heat diffusion equation [32]

$$\rho c_p \frac{\partial T}{\partial t} = k\left(\frac{\partial^2 T}{\partial x^2} + \frac{\partial^2 T}{\partial y^2}\right) + \dot{q} \tag{9}$$

where ρ is the density of the material, cp is the specific heat capacity, and k represents the thermal conductivity. This formulation allows the

temperature distribution within the thermoelectric element to be evaluated as a function of both spatial coordinates and time.

The transient heat diffusion equation is crucial for determining the temperature distribution within thermoelectric elements, enabling the prediction of the thermoelectric module's dynamic thermal behavior under different heat source conditions. Utilizing a two-dimensional model allows for a detailed analysis of temperature distribution in the thermoelectric legs, offering a more accurate depiction of thermal behavior compared to the simplified one-dimensional models frequently employed in previous research.

Simulation Methodology

A numerical simulation framework was established within a high-level numerical computing environment to examine the thermal and electrical characteristics of the thermoelectric generator system. This simulation model determines the temperature distribution and electrical output of individual thermoelectric components and subsequently applies the analysis to large-scale thermoelectric generator systems made up of multiple modules.

In the simulation model, each thermoelectric pellet is divided into multiple computational nodes to accurately capture temperature changes throughout the material. The model incorporates several parameters that vary with temperature, such as the Seebeck coefficient, thermal conductivity, and electrical resistivity. By integrating thermal and electrical equations, the simulation framework forecasts the electrical power output under various thermal operating conditions.

This modeling technique allows for an in-depth examination of thermoelectric generator performance when subjected to fluctuating heat source conditions, such as those found in automotive exhaust systems. The simulation outcomes can assess how temperature differences, material characteristics, and system design affect the electrical power output of the thermoelectric generator.

POWER CONDITIONING AND MAXIMUM POWER POINT TRACKING

Need for Power Conditioning in Thermoelectric Generators

The performance of thermoelectric generators (TEGs) in terms of electrical output is heavily influenced by the temperature differential across

the thermoelectric modules. In real-world applications of waste heat recovery, such as in automotive systems, the temperature of exhaust gases is in constant flux due to varying engine operating conditions. Consequently, the voltage and current produced by the thermoelectric modules change dynamically during their operation.

Thermoelectric generators are known for generating relatively low voltage levels while supplying a higher current. This electrical characteristic often results in inefficient direct connections between thermoelectric modules and electrical loads in most applications. Consequently, power conditioning circuits are necessary to adjust the electrical output of thermoelectric generators, ensuring effective energy transfer to the load or energy storage system.

As depicted in Fig. 1, power conditioning systems typically incorporate DC-DC power converters that adjust the voltage level of the thermoelectric generator to meet the demands of the load. These converters also facilitate the regulation of the generator's operating point to optimize the amount of electrical power extracted. In systems designed for thermoelectric energy harvesting, power conditioning circuits are essential for enhancing overall conversion efficiency and ensuring stable performance under fluctuating thermal conditions [12, 18].

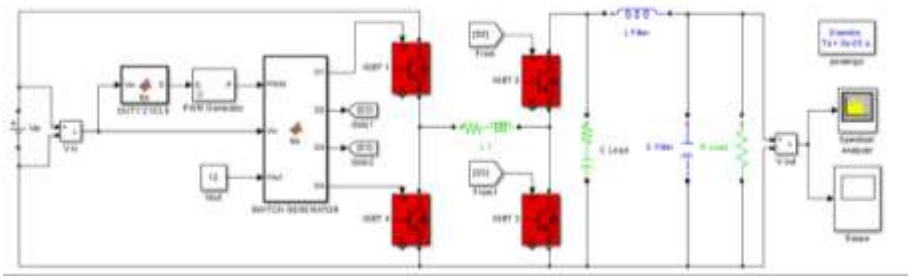

Figure 1: Thermoelectric power generation system including TEG modules, DC–DC converter, and load.

DC–DC Converter Topologies for Thermoelectric Systems

Various DC-DC converter designs can be employed in thermoelectric energy harvesting systems, depending on the specific voltage regulation needs and system setup. Commonly utilized converters include buck converters, boost converters, buck-boost converters, and more sophisticated

configurations like SEPIC converters. These converters adjust the output voltage of the thermoelectric generator to deliver the required voltage level to the electrical load or storage system.

In thermoelectric systems, where the voltage produced is often lower than what is needed, boost converters are commonly used to elevate the voltage level. On the other hand, when the thermoelectric voltage surpasses the necessary load voltage, buck converters might be utilized.

This study explores a thermoelectric generator system that employs a DC-DC converter design based on an H-bridge to manage the output voltage and enhance power transfer efficiency. The H-bridge converter offers versatile power flow control and can function in both buck and boost modes, determined by the duty cycle of the switching signals. By modifying the switching duty cycle, the converter can adeptly adjust the equivalent load resistance perceived by the thermoelectric generator [33].

Need for Power Conditioning in Thermoelectric Generators

MPPT techniques are crucial for ensuring that generators function at their peak power point under different operating conditions when energy harvesting systems are used. These algorithms dynamically modify the duty cycle of the DC-DC converter to align the equivalent load resistance perceived by the thermoelectric generator with its internal resistance.

Various MPPT methods have been proposed for energy harvesting systems, including the fractional open circuit voltage technique, the incremental conductance method, the Perturb and Observe (P&O) strategy, and several metaheuristic optimization approaches [20, 22]. Among these, the Perturb and Observe method is particularly popular due to its straightforwardness and ease of implementation.

The Perturb and Observe algorithm, as depicted in Fig. 2, operates on the fundamental concept of slightly altering the generator's operating voltage or current and monitoring the resulting change in output power. If the power output increases after this adjustment, the control system continues to adjust the operating point in the same direction. Conversely, if the power decreases, the direction of the perturbation is reversed. By repeatedly executing this process, the algorithm gradually approaches the maximum power point.

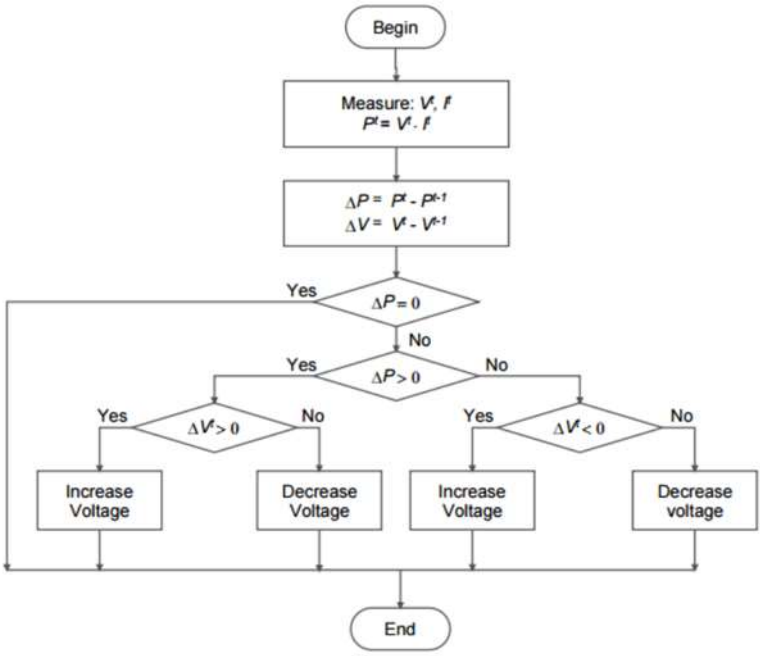

Figure 2: Flowchart of the Perturb and Observe MPPT algorithm [34].

MPPT Implementation in Thermoelectric Systems

In thermoelectric generator systems, the MPPT controller is generally incorporated into the control circuitry of the DC-DC converter. This controller keeps track of the voltage and current generated by the thermoelectric modules and determines the generator's real-time output power. Using this data, the controller modifies the duty cycle of the converter's switching signals to ensure operation remains close to the maximum power point.

In automotive waste heat recovery systems, employing MPPT control greatly enhances energy harvesting efficiency due to the constant fluctuation in temperature across the thermoelectric modules during engine operation. By continuously adjusting the electrical load conditions, the MPPT control system ensures that the thermoelectric generator functions at its peak efficiency across a broad spectrum of thermal conditions.

EXPERIMENTAL THERMOELECTRIC GENERATOR SYSTEM

Thermoelectric Generator Prototype Design

To assess the real-world performance of thermoelectric generators, several prototype models were created and subjected to testing. The

experimental setup was crafted to examine the electrical output, thermal dynamics, and overall efficiency of thermoelectric modules when exposed to varying heat source conditions, as depicted in Fig. 3.

The experimental thermoelectric generator system is composed of thermoelectric modules positioned between a heat exchanger on the hot side and a cooling unit on the cold side. The hot side is exposed to a controlled heat source that simulates the thermal conditions of car exhaust gases, while the cold side is maintained at a lower temperature using a liquid cooling system. This setup creates a consistent temperature difference across the thermoelectric modules, facilitating the generation of electrical power via the Seebeck effect.

The prototype system developed incorporates multiple thermoelectric modules, which are configured in both series and parallel arrangements based on the desired electrical output characteristics. This modular design of the thermoelectric generator allows for flexible scaling of the system and supports the assessment of various module configurations during experimental trials.

.

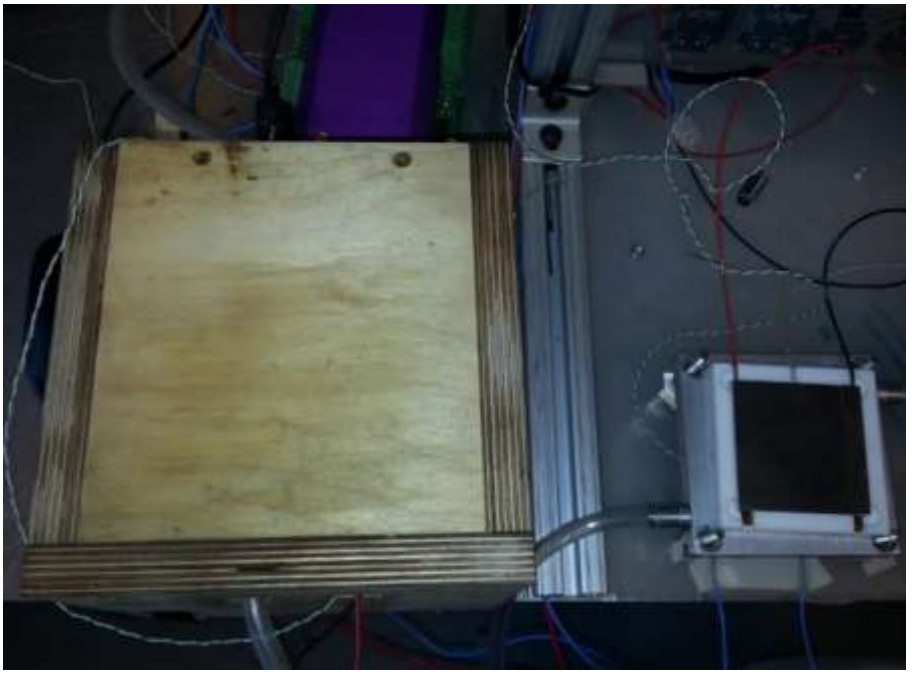

Figure 3: Experimental thermoelectric generator prototype and thermoelectric module arrangement.

Thermoelectric Generator Prototype Design

Precise tracking of thermal and electrical parameters is crucial for assessing the efficiency of thermoelectric generator systems. To achieve this, a data acquisition system was created to record temperature, voltage, and current readings during experimental operations.

To track the temperature difference across the thermoelectric modules, sensors were placed on both the hot and cold surfaces. Additionally, the system's electrical power output was assessed using voltage and current sensors connected to the electrical output terminals of the thermoelectric generator.

The data gathered were sent to a data acquisition unit and logged using a computer-based monitoring system. The measurement setup shown in Fig. 4 facilitated real-time monitoring of the thermoelectric generator's performance and allowed for an in-depth examination of the correlation between temperature differences and electrical power output.

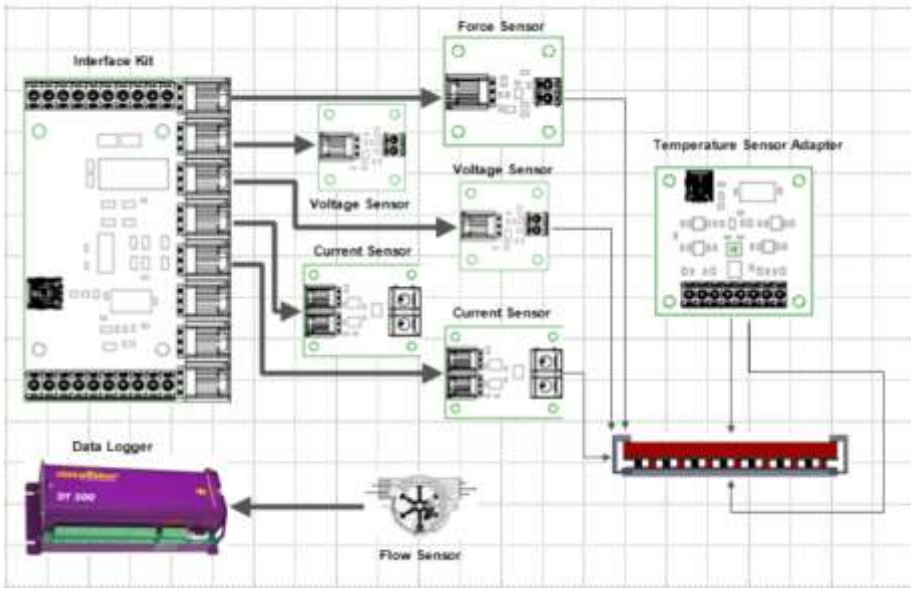

Figure 4: Data acquisition system used for monitoring thermoelectric generator performance.

Experimental Test Setup

The experimental setup was designed to replicate the working conditions of thermoelectric generators in automotive waste heat recovery

systems. This test apparatus comprises a heat source, thermoelectric generator modules, a cooling mechanism, and measurement tools. The heat source delivers a regulated thermal input to the hot side of the thermoelectric modules, while the cooling mechanism ensures the cold side remains at a stable temperature.

In the course of experimental testing, the temperature disparity between the hot and cold sides of the thermoelectric modules is progressively increased, and the resulting electrical output voltage and current are documented. Various electrical load conditions are employed to examine the output power characteristics of the thermoelectric generator.

The experimental arrangement depicted in Fig. 5 facilitates the examination of several crucial factors influencing the performance of thermoelectric generators, such as the temperature gradient, electrical load resistance, and cooling efficiency. These assessments offer valuable insights into the practical behavior of thermoelectric energy harvesting systems.

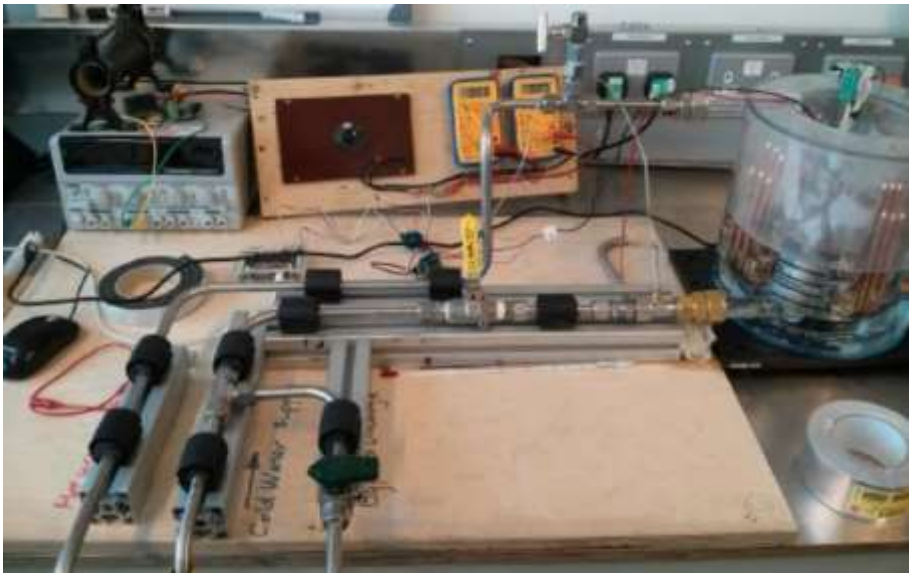

Figure 5: Experimental test rig for thermoelectric generator performance evaluation.

Experimental Results and System Performance

Experimental data reveal that the electrical power output of the thermoelectric generator rises as the temperature difference across the thermoelectric modules increases. When the temperature on the hot side is

elevated while the cold side is kept stable by the cooling system, a greater temperature gradient is formed across the modules, leading to an increase in output voltage and current.

The experimental findings also demonstrate that the highest electrical power is achieved when the load resistance is appropriately aligned with the internal resistance of the thermoelectric generator. When the load is optimally configured, the thermoelectric generator reaches its peak power output for a specific temperature difference.

Moreover, the findings indicate that effective thermal management is crucial for enhancing system performance. Properly cooling the cold side is essential for maintaining a significant temperature difference across the thermoelectric modules, which in turn boosts the system's overall electrical power generation capacity.

The experimental studies confirm the theoretical modeling and simulation methods outlined earlier, demonstrating the practicality of using thermoelectric generators for recovering waste heat. The findings also emphasize the significance of designing integrated systems, which include thermal management, electrical power conditioning, and load optimization, to achieve effective thermoelectric energy conversion.

CHALLENGES AND FUTURE DIRECTIONS

Although thermoelectric generators (TEGs) hold great promise for capturing waste heat and harnessing energy, their widespread use is hindered by various technical and practical obstacles. These obstacles mainly involve the performance of materials, integration into systems, management of heat, and cost-effectiveness. Overcoming these barriers is crucial to enhance the efficiency and practicality of thermoelectric energy conversion systems.

One of the main obstacles in thermoelectric power generation is the relatively low efficiency of current thermoelectric materials. The thermoelectric figure of merit (ZT), which is determined by the material's electrical and thermal conductivity along with the Seebeck coefficient, plays a crucial role in the effectiveness of thermoelectric devices. While materials like bismuth telluride (Bi2Te3) have shown good performance at moderate temperatures, their efficiency is still insufficient for many practical energy harvesting uses. As a result, research is continuously being conducted to create

advanced thermoelectric materials with higher (ZT) values by employing nanostructuring techniques, band structure engineering, and innovative material compositions [9, 14, 15].

A significant challenge in thermoelectric systems involves managing heat and designing heat exchangers. The electrical power output of thermoelectric generators is directly linked to the temperature difference between the hot and cold sides of the thermoelectric modules. In many applications, such as recovering heat from automotive exhaust, it can be challenging to maintain a stable and sufficiently large temperature gradient due to varying operating conditions. Therefore, effective heat exchangers and cooling systems are essential to enhance heat transfer and sustain optimal temperature differences across the thermoelectric modules [6, 7].

Integrating systems is a crucial aspect that influences the effective deployment of thermoelectric generators. In both automotive and industrial applications, it is essential to incorporate thermoelectric modules into the current mechanical and thermal frameworks without notably increasing the complexity or cost of the system. Furthermore, thermoelectric generators necessitate power conditioning electronics, such as DC-DC converters and maximum power point tracking (MPPT) controllers, to efficiently harness electrical energy from fluctuating thermal sources. The design of dependable and efficient power electronics for thermoelectric systems continues to be a focus of ongoing research [12, 18, 22].

Financial factors also pose a significant obstacle to the broad adoption of thermoelectric technologies. The presence of rare or costly elements in many high-performance thermoelectric materials drives up the production expenses of thermoelectric modules. Moreover, extensive thermoelectric systems necessitate numerous modules and sophisticated thermal management components, further escalating the overall system cost. Consequently, future research should prioritize the development of cost-efficient thermoelectric materials and scalable manufacturing methods to facilitate the large-scale implementation of thermoelectric energy harvesting systems.

Looking ahead, there are several promising avenues for research that could further boost the effectiveness and usability of thermoelectric generators. Progress in nanostructured thermoelectric materials and hybrid systems holds the promise of greatly enhancing thermoelectric efficiency.

Moreover, combining thermoelectric generators with other renewable energy technologies, like photovoltaic systems and hybrid energy harvesting frameworks, could open up new possibilities for increasing overall energy conversion efficiency.

One promising avenue is the creation of sophisticated control algorithms and smart power management strategies for thermoelectric systems functioning in fluctuating thermal environments. Optimization methods based on machine learning and adaptive techniques for tracking the maximum power point could enhance the efficiency of thermoelectric generators in scenarios with highly variable heat sources.

In conclusion, while thermoelectric generators encounter various technical obstacles, continuous progress in materials science, thermal engineering, and power electronics is broadening their range of potential uses. As technology advances further, thermoelectric energy conversion is anticipated to become increasingly significant in future energy harvesting and waste heat recovery systems.

CONCLUSIONS

Thermoelectric generators (TEGs) utilize solid-state energy conversion processes to potentially convert waste heat into electrical power. This study has delivered an extensive summary of systems for harvesting thermoelectric energy, emphasizing TEGs specifically designed for recovering waste heat. Initially, the basic principles of thermoelectric energy conversion, such as the Seebeck, Peltier, and Thomson effects, were introduced to lay the groundwork for understanding thermoelectric power generation.

The discussion focused on the structural features and electrical equivalent modeling of thermoelectric generators to elucidate the connection between temperature differences, internal resistance, and the generation of electrical power. Furthermore, thermal modeling techniques for thermoelectric modules were explored, emphasizing the critical role of precise heat transfer analysis in forecasting device performance. The modeling framework presented illustrated the interconnection of thermal and electrical phenomena in thermoelectric systems and demonstrated how simulation tools can be employed to evaluate generator behavior under varying thermal conditions.

Power conditioning and maximum power point tracking (MPPT) methods were highlighted as crucial elements in effective thermoelectric energy harvesting systems. Due to the fact that the electrical properties of thermoelectric generators change with temperature and load variations, DC-DC power converters paired with MPPT algorithms facilitate the efficient capture of electrical energy from fluctuating heat sources. These control techniques greatly enhance the overall efficiency and reliability of thermoelectric generator systems.

Additionally, experimental studies were conducted to support the theoretical models and illustrate the practical viability of thermoelectric generators. The experimental setup for the thermoelectric generator, which included the test rig configuration and data collection system, enabled a comprehensive examination of the correlation between temperature variation and electrical power generation. The findings verified that the electrical efficiency of thermoelectric generators is highly reliant on efficient thermal management and appropriate electrical load alignment.

Although there are current challenges with conversion efficiency and the cost of materials, thermoelectric generators remain a focal point of research due to their dependability, scalability, and capability to capture energy from heat sources that would otherwise go unused. Future improvements in thermoelectric materials, advancements in heat exchanger designs, and smart power conditioning methods are anticipated to further boost the performance of thermoelectric systems.

Thermoelectric generators present a practical option for capturing waste heat and harnessing energy in automotive, industrial, and renewable energy sectors. Ongoing advancements in materials science, thermal engineering, and power electronics are crucial for enhancing the efficiency and cost-effectiveness of thermoelectric technologies in future energy systems.

REFERENCE

[1]. Hendricks, T., & Choate, W. T. (2006). Engineering scoping study of thermoelectric generator systems for industrial waste heat recovery. Pacific Northwest National Laboratory (PNNL), Richland, WA (United States).

[2]. Jabbar, M. Y., Ahmed, S. Y., & Khafaji, S. O. W. (2024). A scoping review of the thermoelectric generator systems designs (heat exchangers and coolers) with locations of application to recover energy from internal combustion engines. Journal of Applied and Computational Mechanics, 10(3), 547-583.

[3]. Win, S. L. Y., Chiang, Y. C., Huang, T. L., & Lai, C. M. (2024). Thermoelectric generator applications in buildings: a review. Sustainability, 16(17), 7585.
[4]. Bergman, T. L. (2011). Fundamentals of heat and mass transfer. John Wiley & Sons.
[5]. Karwa, R. (2020). Heat and mass transfer. Springer Nature.
[6]. Rodriguez, R., Preindl, M., Cotton, J. S., & Emadi, A. (2019). Review and trends of thermoelectric generator heat recovery in automotive applications. IEEE Transactions on Vehicular Technology, 68(6), 5366-5378.
[7]. Asaduzzaman, M., Ali, M. H., Pratik, N. A., & Lubaba, N. (2023). Exhaust heat harvesting of automotive engine using thermoelectric generation technology. Energy Conversion and Management: X, 19, 100398.
[8]. Zlatic, V., & Hewson, A. (Eds.). (2009). Properties and applications of thermoelectric materials: the search for new materials for thermoelectric devices. Springer Science & Business Media.
[9]. Zebarjadi, M., Esfarjani, K., Dresselhaus, M. S., Ren, Z. F., & Chen, G. (2012). Perspectives on thermoelectrics: from fundamentals to device applications. Energy & Environmental Science, 5(1), 5147-5162.
[10]. Crane, D. T., & LaGrandeur, J. W. (2010). Progress report on BSST-Led US department of energy automotive waste heat recovery program. Journal of electronic materials, 39(9), 2142-2148.
[11]. Risseh, A. E., Nee, H. P., Erlandsson, O., Brinkfeldt, K., Contet, A., Gaiser, G., ... & Dellrud, J. (2017). Design of a thermoelectric generator for waste heat recovery application on a drivable heavy duty vehicle. SAE International Journal of Commercial Vehicles, 10(2017-01-9178), 26-44.
[12]. Zoui, M. A., Bentouba, S., Stocholm, J. G., & Bourouis, M. (2020). A review on thermoelectric generators: Progress and applications. Energies, 13(14), 3606.
[13]. Witting, I. T., Chasapis, T. C., Ricci, F., Peters, M., Heinz, N. A., Hautier, G., & Snyder, G. J. (2019). The thermoelectric properties of bismuth telluride. Advanced Electronic Materials, 5(6), 1800904.
[14]. Zhang, X., & Zhao, L. D. (2015). Thermoelectric materials: Energy conversion between heat and electricity. Journal of Materiomics, 1(2), 92-105.
[15]. Hong, M., Chen, Z. G., & Zou, J. (2018). Fundamental and progress of Bi2Te3-based thermoelectric materials. Chinese Physics B, 27(4), 048403.
[16]. Kim, S. (2013). Analysis and modeling of effective temperature differences and electrical parameters of thermoelectric generators. Applied energy, 102, 1458-1463.
[17]. Kumar, S., Heister, S. D., Xu, X., Salvador, J. R., & Meisner, G. P. (2013). Thermoelectric generators for automotive waste heat recovery systems part I: Numerical modeling and baseline model analysis. Journal of electronic materials, 42(4), 665-674.
[18]. Lan, S., Yang, Z., Chen, R., & Stobart, R. (2018). A dynamic model for thermoelectric generator applied to vehicle waste heat recovery. Applied energy, 210, 327-338.
[19]. Luo, D., Yan, Y., Chen, W. H., & Cao, B. (2024). Exploring the dynamic characteristics of thermoelectric generator under fluctuations of exhaust heat. International Journal of Heat and Mass Transfer, 222, 125151.
[20]. De Brito, M. A. G., Galotto, L., Sampaio, L. P., e Melo, G. D. A., & Canesin, C. A. (2012). Evaluation of the main MPPT techniques for photovoltaic applications. IEEE transactions on industrial electronics, 60(3), 1156-1167.

[21]. Eltawil, M. A., & Zhao, Z. (2010). Grid-connected photovoltaic power systems: Technical and potential problems—A review. Renewable and sustainable energy reviews, 14(1), 112-129.
[22]. Chen, Y., Xie, C., Li, Y., Zhu, W., Xu, L., & Gooi, H. B. (2023). An improved metaheuristic-based MPPT for centralized thermoelectric generation systems under dynamic temperature conditions. Energy, 277, 127485.
[23]. Kanagaraj, N. (2021). Photovoltaic and thermoelectric generator combined hybrid energy system with an enhanced maximum power point tracking technique for higher energy conversion efficiency. Sustainability, 13(6), 3144.
[24]. Qasim, M. A., Velkin, V. I., & Hassan, A. K. (2022). Seebeck generators and their performance in generating electricity.
[25]. Vargas, J. C. C., Rodríguez, M. J. L. D., García, P. A. P., & Figueroa, M. M. A PELTIER CELLS RESEARCH-(FIRST PART).
[26]. Lee, H. (2016). Thermoelectric Generators. poglavlje u knjizi: Thermoelectrics: Design and Materials, Wiley, Western Michigan University, 8-22.
[27]. DiSalvo, F. J. (1999). Thermoelectric cooling and power generation. science, 285(5428), 703-706.
[28]. Maduabuchi, C., Lamba, R., Ozoegwu, C., Njoku, H. O., Eke, M., Gurevich, Y. G., & Ejiogu, E. C. (2022). Thomson effect and nonlinear performance of thermoelectric generator. Heat and Mass Transfer, 58(6), 967-980.
[29]. Alam, H., & Ramakrishna, S. (2013). A review on the enhancement of figure of merit from bulk to nano-thermoelectric materials. Nano energy, 2(2), 190-212.
[30]. Han, J., Sun, Q., Li, W., & Song, Y. (2017). Microstructure and thermoelectric properties of La0. 1Dy0. 1SrxTiO3 ceramics. Ceramics International, 43(7), 5557-5563.
[31]. Wang, B. L. (2017). A finite element computational scheme for transient and nonlinear coupling thermoelectric fields and the associated thermal stresses in thermoelectric materials. Applied Thermal Engineering, 110, 136-143.
[32]. Thomas, B. G., Samarasekera, I. V., & Brimacombe, J. K. (1984). Comparison of numerical modeling techniques for complex, two-dimensional, transient heat-conduction problems. Metallurgical Transactions B, 15(2), 307-318.
[33]. Mi, C., Bai, H., Wang, C., & Gargies, S. (2008). Operation, design and control of dual H-bridge-based isolated bidirectional DC–DC converter. IET Power Electronics, 1(4), 507-517.
[34]. Lian, K. L., Jhang, J. H., & Tian, I. S. (2014). A maximum power point tracking method based on perturb-and-observe combined with particle swarm optimization. IEEE journal of photovoltaics, 4(2), 626-633.